UNIVERSIDAD DE CHILE
FACULTAD DE CIENCIAS FÍSICAS Y MATEMÁTICAS
DEPARTAMENTO DE ASTRONOMÍA

SUPER MASSIVE BLACK HOLES AND THE CENTRAL REGION IN ACTIVE GALACTIC NUCLEI

TESIS PARA OPTAR AL GRADO DE DOCTOR EN CIENCIAS, MENCIÓN ASTRONOMÍA

JULIÁN ESTEBAN MEJÍA RESTREPO

PROFESOR GUÍA:
PAULINA MARÍA LIRA TEILLERY

MIEMBROS DE LA COMISIÓN:
KONRAD TRISTRAM
LEONARDO JAIME BRONFMAN AGUILÓ
LUIS EDUARDO CAMPUSANO BROWN
MANUEL ALEJANDRO ARAVENA AGUIRRE
VALENTINO GASTÓN GONZÁLEZ

SANTIAGO DE CHILE
AGOSTO 2017

RESUMEN DE LA TESIS PARA OPTAR AL GRADO DE DOCTOR EN CIENCIAS, MENCIÓN ASTRONOMÍA

AGUJEROS NEGROS SUPERMASIVOS Y LA REGIÓN CENTRAL EN NÚCLEOS ACTIVOS DE GALAXIAS

En este trabajo presento un estudio de la región central de galaxias activas orientado a mejorar las estimaciones de masas de agujeros negros supermasivos distantes y a dilucidar las propiedades del gas en sus cercanías. En el primer capítulo intruduzco brevemente los conceptos básicos y presento los descubrimientos más relevantes así como las grandes problemáticas asociadas al objeto de estudio de esta tesis.

A continuación, en el segundo capítulo presento un estudio orientado a mejorar las calibraciones actuales para medición de masas de agujeros negros supermasivos distantes usando líneas de emisión características de la región de líneas anchas tales como Hα, Hβ y Mg II λ2798 (de bajo nivel de ionización) y C IV λ1549 (de alto nivel de ionización). La novedad de este trabajo radica en el uso de observaciones espectrales simultáneas de las líneas de emisión a recalibrar lo que evita posibles efectos de variabilidad en la emisión de los cuásares estudiados. Lo anterior es posible gracias a las observaciones de 39 cuásares a redshift $\sim$ 1.55 mediante el uso del espectrógrafo X-Shooter del telescopio VLT cuya gran cobertura espectral permite el mapeo simultáneo de las líneas de emisión antes mencionadas. Además de presentar nuevas calibraciones, los resultados indican que las líneas de baja ionización proveen estimaciones de masa más confiables que las basadas en C IV λ1549.

En el tercer capítulo, estudio la posibilidad de mejorar las estimaciones de masa usando C IV λ1549 mediante algunos métodos propuestos en la literatura además del método propuesto en el segundo capítulo de esta tesis. Todos estos métodos se basan en correlaciones encontradas usando muestras pequeñas de menos de 100 objetos. Para cuantificar la solidez estadística de éstos aquí se usa la base de datos de cuásares del Sloan Digital Sky Survey de la cual se extrajo una muestra de cerca de 30000 objetos. Los resultado encontrados sugieren que todos los métodos actualmente sugeridos tienen un efecto muy limitado en el mejoramiento de las estimaciones de masas usando C IV λ1549.

Finalmente, en el cuarto capítulo estudio el efecto de la distribución del gas de la región de líneas anchas en la estimación de masas. Lo anterior es posible gracias a la comparación entre masas obtenidas por el método ya descrito y masas estimadas mediante el ajuste del modelo estándar del disco de acreción al espectro de emisión de este. Los resultados sugieren una fuerte dependencia del cociente de ambas estimaciones de masa con el ancho observado de las líneas de emisión.

SUMMARY OF THESIS FOR THE DEGREE OF DOCTOR OF PHYLOSOPHY IN ASTRONOMY

SUPER MASSIVE BLACK HOLES AND THE CENTRAL REGION IN ACTIVE GALACTIC NUCLEI

Here I present an in-depth study of the central region of active galactic nuclei oriented to improve current mass estimation methods of distant super massive black holes and to infer the physical properties of the gas in their vicinity. In the first chapter I briefly introduce the basic concepts and present the most relevant discoveries and problematics associated to the central topic of this thesis.

Then, in the second chapter, I present new calibrations of the so called single epoch black hole mass estimation method. This method uses emission lines from the broad line region such as the Hα, Hβ and Mg II λ2798 low ionization lines, and the C IV λ1549 high ionization line. The novelty of this work is the usage of simultaneous observations of these emission lines that prevents from possible variability effects. The latter was possible thanks to the observations of 39 quasars a $z \sim 1.55$ using the X-Shooter spectrograph of the VLT telescope whose wide spectral coverage allows simultaneous mapping of the aforementioned emission lines. In addition to presenting new calibrations, the results of this study indicate that low ionization lines provide more accurate mass estimations than C IV λ1549 as it was suggested by previous studies.

In the third chapter, I examine the possibility of improving current C IV λ1549-based mass estimates of super-massive black holes by testing the performance of some methods proposed in the literature, including a method proposed in this thesis. All these methods are based on correlations found using small samples of less than 100 objects. In order to quantify the statistical robustness of these methods, in this work I use the Sloan Digital Sky Survey quasar database out of which I extracted a sample of nearly 30000 objects. The results suggest that the methods studied here have a very limited effect on the improvement of C IV λ1549-based mass estimations.

Finally, in the fourth chapter, I study the effect of gas distribution of the broad line region on mass estimations. This is possible thanks to the comparison between masses obtained from the single epoch method and those obtained from the fitting the accretion disc spectral energy distribution to standard accretion disk models. The results indicate a strong dependence of the ratio between both mass estimates with the observed width of the broad emission lines.

Acknowledgements

En primer lugar agradezco a mi profesora y asesora Paulina Lira por las discusiones científicas de gran valor para este trabajo así como por su apoyo, guía y oportunidades dadas a lo largo de mi doctorado. Hago de igual manera un reconocimiento especial al excelente e intachable trato humano recibido de su parte. Agradezco también enomermente a mis co-asesores Benny Trakhtenbrot y Hagai Netzer cuyo aporte fue indispensable para llevar a cabo este trabajo. De igual manera, agradezco a mi comité de tesis por sus comentarios y críticas constructivas que ayudaron en la cristalización de este proyecto. Extiendo también mis agradecimientos a los profesores del departamento que aportaron directa o indirectamente a mi formación así como a todos los funcionarios que le dan vida a Calán.

Agradezco además a todos mis compañeros de posgrado en especial a Alessandro, Felipe, Paula y Thomas con los cuales tuve más cercanía durante estos años. Por supuesto, ofrezco un agradecimiento singular a mi amigos Ángel y Sebastián quienes empezaron conmigo esta aventura doctoral y han sido un gran apoyo en diversos momentos durante mi estadía en este hermoso país. De igual manera hago un reconocimiento a mis más grandes amigos: Carolina, Catalina, Catherine, Cornelio, Daniel, David Felipe, José David, Laura, Mauricio, Malory y Xiomara quienes de una u otra manera estuvieron presentes durante todo este proceso.

Estas últimas líneas quiero regarlárselas a las personas más importantes en mi vida a quienes adoro y admiro profundamente: a mi gran amor, Elizabeth, a mis padres, Margarita y Reinel, a mi hermana, Erika y a mis más cercanos familiares. A Eli le agradezco inmensamente su compañía, apoyo incondicional y amor profundo que han hecho de esta zigzagueante travesía un camino mucho más amable de recorrer. A mis padres les agradezco el apoyo sin reparos, el amor único e ilimitado que sólo ellos pueden ofrecerme y por haber hecho de la educación una prioridad en nuestra crianza. A mi hermana le agradezco por su gran ejemplo como científica, su cariño, sus palabras de aliento y por haberme regalado la inmensa felicidad de ser tío de nuestro consentido y adorado Tomás. ¡Gracias familia!.

El trabajo de esta tesis fue financiado por "CONICYT-PCHA/doctorado Nacional para extranjeros/2013-63130316".

Table of Contents

Chapter 1

Introduction

1.1 Active Galactic Nuclei

It is widely accepted that the majority of galaxies host a super-massive black hole (SMBH) at their centres. The study of local-quiescent galaxies has exhibit a strong correlation between their SMBH mass ($M_{\rm BH}$) and their bulge stellar dispersion ($\sigma_\star$ i.e., the $M_{\rm BH} - \sigma_\star$; Ferrarese & Merritt, 2000). This connection suggests co-evolution of the assembly of the host galaxy and the growth of the SMBH. During their growing phases, SMBHs experience several episodes of active accretion of material. We call "Active galaxies" or "active galactic nuclei" (AGN) those galaxies whose SMBHs are undergoing one of these accretion episodes.

UV and optical AGN radiation corresponds to the emission from an accretion disc (AD) funnelling matter onto a SMBH that converts a large amount of gravitational energy into radiation (Shakura & Sunyaev, 1973). The high density material ($n_{\rm H} \gtrsim 10^9 cm^{-3}$) close to the AD is photo-ionized by the strong AD radiation field and present large peculiar velocities of thousands of kilometres per second associated to Keplerian motion around the SMBH. As a result of electron recombination this material leaves an imprint of very broad emission lines in the observed spectra. This material is usually referred to as the broad line region (BLR). This region extends up to the dust sublimation radius which is the distance at which dust no longer evaporates and survives the AD radiation field. Starting at this radius, an obscuring structure of dust and gas is found which is usually referred to as the dusty torus. In spite of this common name, its geometry, dynamics and associated covering factor is still largely unknown (e.g. Stalevski et al., 2016). Furthermore, it is still unclear whether the torus properties depend on the luminosity, redshift, or the evolutionary state of host galaxies.

Further away from the SMBH, the dynamics are dominated by the host galaxy rather than by the SMBH. As a consequence, the typical velocities associated to that gas are only a few hundred of kilometres per second. The gas facing the AD is also photo-

ionized by the AD radiation field. As a product of recombination, narrow emission lines are formed and determine the commonly called narrow line region (NLR).

AGN activity can also be characterized by the collimated ejection of material at relativistic speeds, which is observed in about 10% of objects. Better studied at radio wavelengths, these structures are known as radio-jets. In Figure 1.1.1 I show an schematic representation of an active galaxy with a central SMBH of $10^8 M_\odot$ showing the typical physical scales associated to each of its components.

There are three key parameters of AGN activity. First, the SMBH mass ($M_{\rm BH}$). Second, the mass accretion rate ($\dot{M}$) that is often described by the ratio of the bolometric luminosity (L) to the Eddington luminosity ($L/L_{\rm Edd}$). Finally, the SMBH angular momentum (J) that is usually represented by the dimensionless spin parameter $a_* = J/(GM^2/c)$ and which settles the innermost limit of the accretion disc. According to its definition, a_* can take all values between -1 and 1 where both limiting values are measured with respect to the AD direction of rotation and are respectively associated to maximally counter-rotating and co-rotating SMBHs. These three properties, $M_{\rm BH}$, $\dot{M}$ and a_* jointly determine the AGN bolometric luminosity.

The role of the black hole spin is crucial in AGN activity. Particularly, a_* determines the innermost stable circular orbit (ISCO) which sets the internal boundary of the AD. Because of this boundary, a_* also regulates (1) the maximum temperature of the AD emission, (2) the shape of the bluest region of the AD spectral energy distribution (SED) and (3) the efficiency (η) of radiative energy extraction in terms of the total amount of in-falling mass (i.e. $\eta \equiv L/\left(\dot{M}c^2\right)$). The difference of the energy output between maximally counter-rotating and co-rotating SMBHs is dramatic with associated efficiencies of $\eta = 0.038$ and $\eta = 0.32$, respectively. In most studies a value of $\eta = 0.1$ is adopted as a canonical AD efficiency.

Different observational features distinguish AGN from inactive galaxies. In particular, for galaxies to be classified as AGN, they should meet *at least* one of the following properties:

- Contain a compact central region that emits electromagnetic radiation far beyond the luminosity than would be expected from a stellar system of similar size.
- Show clear evidence of non-stellar continuum emission at their center.
- Show strong broad an/or narrow emission lines whose line ratios cannot be explained by stellar radiation fields.
- Show variability of their continuum and line emission.
- Show intense ($\gtrsim 10^{42}{\rm erg\,s^{-1}}$) hard X-ray emission ($\gtrsim$ 10 KeV).
- Show strong and/or collimated radio emission.

1.2 AGN Diversity

Despite the common physical origin, clear differences are observed in the spectral properties of AGN that conveyed into different sub-classifications. Among all of them, Khachikian & Weedman (1974) proposed two sub-classes to differentiate the properties of their optical and UV spectra: Type-1 (broad-line) and Type-2 (narrow-line) AGN. On the one hand, Type-1 AGN are characterized by their strong broad emission lines produced in the BLR and intense non-stellar continuum emission from the accretion disc. On top of the broad lines, type-1 AGN exhibit narrower emission lines from ionized material in the NLR. On the other hand, type-2 AGN are characterized by only displaying the narrow emission line component. However, Antonucci & Miller (1985) observed broad emission lines on the spectrum of the polarized light of NGC1068 that was previously classified as Type-2 AGN. Such polarized light can be interpreted as coming from the nucleus and being scattered into the light of sight of the observer. This observation suggested an unification model where the AD and the BLR are surrounded by a dusty toroidal-like structure, the torus (Antonucci, 1993; Urry & Padovani, 1995). Under this model, type-1 and type-2 AGN are physically equivalent but are being observed at different line-of-sight inclinations. Specifically, type-2 AGN are objects objects in which our line-of-sight intercepts the torus, which absorbs most of the light coming from the AD and the BLR (an schematic representation of the unification model can be observed in Figure 1.1.1). Even though this model has been successful at explaining the diversity of AGN population, it is still under debate whether the differences between type-1 and type-2 AGN are only caused by an inclination effect, or they can be also associated to, for instance, different evolutionary phases of galaxy evolution (e.g. Satyapal et al., 2014; Del Moro et al., 2016; Ricci et al., 2017).

1.3 Black Hole Masses

The formerly mentioned $M_{\rm BH} - \sigma_\star$ relation suggests that AGN do not only modify their local environment but also their host-galaxy (or vice-versa). As a matter of fact, there is accumulated evidence that AGN activity induces outflows that extend up to kiloparsec scales (e.g. Arav et al., 2013; Borguet et al., 2013). As a result, it is expected that AGN activity plays a key role in galactic-scale feedback and the regulation of star formation processes as the host galaxy evolves. This is supported by the observed coincidence of the peak at $z \sim 2$ of star-formation rate and the AGN density of the universe (Wall et al., 2005). Likewise, the $M_{\rm BH} - \sigma_\star$ relation also indicates that $M_{\rm BH}$ is probably the most relevant parameter connecting SMBH with galaxy evolution. As a consequence, precise and accurate $M_{\rm BH}$ measurements are key for a proper examination of the co-evolution of host galaxies and SMBHs.

In type-1 AGN, a common approach to estimate $M_{\rm BH}$ relies on the assumption that the BLR is in virial equilibrium. In this case, the linewidth ($\Delta W_{\rm obs}$) of a given emission

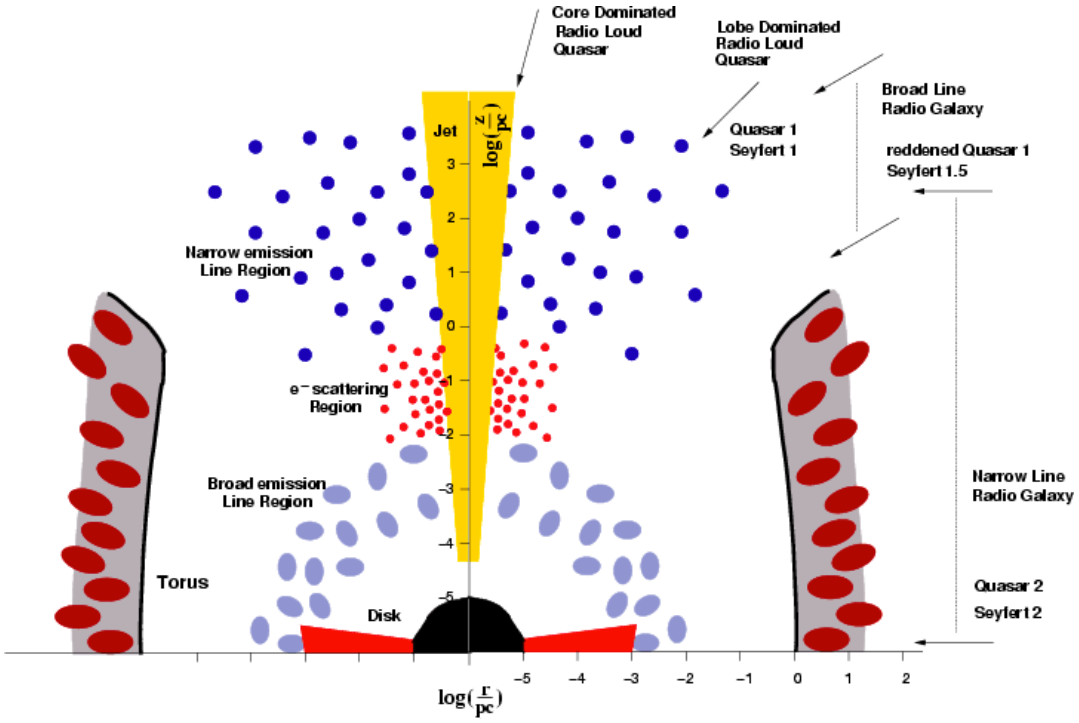

Figure 1.1.1: Graphical representation of an AGN with a central SMBH of $10^8 M_\odot$. Credits: C. Zier & P. L. Biermann. A&A 396, 91-108 (2002)

line can be used as a proxy for the Keplerian velocity ($V_{\rm BLR}$) of the BLR line-emitting region around the SMBH. Under these assumptions $M_{\rm BH}$ can be expressed as:

$$M_{\rm BH} = G^{-1} R_{\rm BLR} V_{\rm BLR}^2 = f\ G^{-1} R_{\rm BLR}\ \Delta W_{\rm obs}^2 \tag{1.1.1}$$

where G is the gravitational constant, $R_{\rm BLR}$ is the distance from the BLR to the SMBH and f is the virial factor that accounts for the difference between $V_{\rm BLR}$ and $\Delta W_{\rm obs}$ which depends on the gas distribution and kinematics of the BLR. Since even in the closest galaxies the BLR cannot be resolved with current capabilities, $R_{\rm BLR}$ cannot be measured from direct imaging. Fortunately, $R_{\rm BLR}$ can be estimated using a direct technique named reverberation mapping (RM, e.g., Blandford & McKee 1982; Peterson 1993). This method traces the light-time delay (τ) between accretion disc continuum flux variations and the subsequent response of the BLR broad emission-line flux. Given that the AD is right next to the SMBH, $R_{\rm BLR}$ is simply approximated to $c\tau$, where c is speed of light. As a first order approximation, f is assumed to be constant in all systems and is determined by requiring RM-based masses to agree, on average, with dynamically masses determined from the $M_{\rm BH}$-$\sigma_\star$ relation in local inactive galaxies (Onken et al., 2004; Graham, 2015; Woo et al., 2015).

Even though RM is a successful technique, it is not useful for $M_{\rm BH}$ determination in large samples. In fact, RM technique has only measured $M_{\rm BH}$ in 63 low-z ($z < 0.1$) type-1 AGN (Kaspi et al., 2000, 2005; Bentz et al., 2009, 2013) and only a handful of high-

luminosity, high-redshift sources (e.g. Kaspi et al., 2007, ; Lira et al. 2017, submitted). The main reason for this is the necessity of long term systematic monitoring of objects (of the order of months and even years) to adequately determine $R_{\rm BLR}$. Furthermore, the typical time scale of line response to continuum variation increases with AGN luminosity and, because of cosmological time dilution, it also increases with redshift. Fortunately, RM campaigns have revealed an underlying direct relationship between the radius of the BLR, $R_{\rm BLR}$, and the median AGN accretion disc continuum, thus allowing the estimation of $R_{\rm BLR}$ from a simple continuum flux measurement. This correlation is best calibrated for the Hβ emission line and the median AGN accretion disc continuum emission at 5100Å (Kaspi et al., 2000, 2005; Bentz et al., 2009, 2013). The use of this relationship and the cross-calibrations to other broad emission lines (e.g., Hα, Mg II λ2798 and C IV λ1549) has provided the community with a much less expensive procedure that allow $M_{\rm BH}$ estimations in large data samples of type-I AGN using a single optical spectrum for each object and covering a large redshift range ($0 \lesssim z \lesssim 7$). This indirect technique for $M_{\rm BH}$ determination is called the single epoch (SE) virial method and is widely used to estimate $M_{\rm BH}$ in type-1 AGN (e.g. McLure & Jarvis, 2002; Greene & Ho, 2005; Vestergaard & Peterson, 2006; Vestergaard & Osmer, 2009; Wang et al., 2009; Trakhtenbrot et al., 2011; Xiao et al., 2011; Shen & Liu, 2012; Trakhtenbrot & Netzer, 2012; Park et al., 2013; Mejía-Restrepo et al., 2016).

Regardless of the advantageous possibility to determine $M_{\rm BH}$ in large samples, SE estimations are subject several difficulties. Particularly, one crucial difficulty is the unreliable measurements provided by SE calibrations of the C IV λ1549 high ionization line that is used for estimations at $z \gtrsim 2.0$ in optical surveys. The latter is most probably caused by non-virial motion of the C IV λ1549 emitting material which is revealed by its largely blueshifted emission with respect to the host galaxy reference frame (up to 5000km s^{-1}, see e.g. Richards et al., 2011). As a consequence, high redshift $M_{\rm BH}$ estimations are highly uncertain, imposing serious complications for the appropriate study of the assembly of the $M_{\rm BH}$-$\sigma_\star$ relation.

On top of the problematics with SE C IV λ1549 based estimations, assuming a constant f is presumably one of the major sources of uncertainties in SE estimations because the gas distribution and dynamics of the BLR might change from object to object. There have been some attempts to unveil possible dependencies of f on the BLR and SMBH observed properties. All these works compare SE mass estimations with masses obtained using the median trend of the $M_{\rm BH}$-$\sigma_\star$ scaling relation or associated correlations (e.g. Collin et al., 2006; Decarli et al., 2008b; Shen & Ho, 2014). Some of these works have suggested an anti-correlation between f and the observed full width at half maximum (FWHM$_{\rm obs}$) of the broad emission lines. This result has been understood as an effect of line of sight inclination due to a planar distribution of the BLR gas. All these works, however, apply the same prescription to all systems, assuming that all objects are well represented by the median trend of the scaling relation used to alternatively derive $M_{\rm BH}$, and do not take into account the large intrinsic scatter in such relations.

Recently, Capellupo et al. (2015, 2016) improved an alternative method to estimate $M_{\rm BH}$ based on Bayesian SED fitting of the accretion disc. The accretion disc was modelled using the standard Shakura & Sunyaev (1973) geometrically thin optically thick model with general relativistic and disc atmosphere corrections (Slone & Netzer, 2012). Each model is defined by its black hole mass, accretion ratio, spin and the intrinsic reddening in the host galaxy. Using this model we successfully reproduced the SED emission in 37 out of 39 objects at $z = 1.55$ observed with the X-Shooter spectrograph of the VLT telescope. The advantage of this sample is that, at such redshift, the wide spectral coverage provide by X-Shooter maps a large region of the accretion disk SED that allows a proper modelling of the AD. The relevance of this alternative $M_{\rm BH}$ estimation method is that it only uses information coming from the AD. Hence, these masses are independent of the BLR gas distribution and dynamics. As a consequence, comparing the AD-based with the SE-based black hole masses opens the possibilities to infer the underlying BLR distribution and to uncover possible biases in SE-based estimations.

1.4 This Thesis

The topic of study of this thesis are *distant* type-1 AGN which are also called quasars. Particularly, I present a thorough study of the central region of quasars aiming to improve current mass estimation methods of *distant* super massive black holes and to examine the properties of their BLRs. For this purpose, I divide this document in three central topics: (1) determination of new calibrations for SE black hole mass estimation, (2) investigation of the possibility to improve single epoch C IV-based mass estimations and (3) exploration of the effect of the BLR gas distribution on the mass determination of distant supermassive black holes. Below, I provide a short description of the chapters of this thesis.

Chapter 2 is mainly devoted to improve current calibrations of the SE $M_{\rm BH}$ estimation method that uses emission lines from the broad line region such as the Hα, Hβ and Mg II λ2798 low ionization lines, and the C IV λ1549 high ionization line. To this end we used the sample of 39 quasars at $z \sim 1.55$ observed by X-Shooter that is described in Capellupo et al. (2015, 2016). The wide spectral coverage provided by X-Shooter allows simultaneous mapping of the aforementioned emission lines and prevents possible variability effects on our calibrations. In addition to new $M_{\rm BH}$ calibrations, I evaluate the effect of continuum placement on the $M_{\rm BH}$ determination and propose a new method oriented to improved C IV λ1549-based mass estimations. The results of this study are presented in Mejía-Restrepo et al. (2016)

In Chapter 3, I use the Sloan Digital Sky Survey quasar database (SDSSQ) to test the performance of some methods available in the literature, including the one proposed in Chapter 2, that are intended to improve C IV λ1549-based mass estimates. All the proposed methods are based on correlations found using small samples of less

than 100 objects. In comparison, from the SDSSQ data we extracted a sub-sample of nearly 30000 objects. This allows us to perform robust statistical analyses to check the significance and independence from other correlations and conclude on the actual applicability of these methods.

Chapter 4 studies the effect of the unknown BLR gas distribution on the determination of $M_{\rm BH}$ and concludes on the probable BLR distribution causing such effect. This analysis is possible thanks to the comparison between SE-based and AD-based $M_{\rm BH}$ estimations that were obtained using the X-Shooter samples previously described. The results of this work are presented in Mejia-Restrepo et al. (2017, submitted to Nature-Astronomy).

Finally, in chapter 5 I present the summary and most relevant conclusions of this thesis.

Chapter 2

Single epoch super massive black hole masses estimations: recalibration and analysis

The material presented in this chapter is based on the work published in Mejía-Restrepo et al. (2016)

2.1 Introduction

The mass ($M_{\rm BH}$) of Super Massive Black Holes (SMBHs), along with the SMBH spin (a_*) and accretion rate ($\dot{M}$), are the fundamental parameters that drive the physical, geometric and kinematic properties of the SMBH environment (e.g. Kaspi et al., 2005; Slone & Netzer, 2012; Capellupo et al., 2015). $M_{\rm BH}$ is also known to be correlated with several properties of the host galaxy, suggesting a so-called "co-evolutionary" scenario for the SMBH and stellar component of the host (e.g. Ferrarese & Merritt, 2000; Häring & Rix, 2004; Gültekin et al., 2009; Xiao et al., 2011). Therefore, accurate and precise determinations of $M_{\rm BH}$, across cosmic epochs, are crucial for our understanding of SMBH physics and evolution.

For un-obscured, type-I actively growing SMBHs (active galactic nuclei - AGN), $M_{\rm BH}$ can be estimated from single epoch spectra of several broad emission lines. The method, which was used for many large samples of AGN across cosmic epochs (e.g., Croom et al., 2004; McLure & Dunlop, 2004; Onken et al., 2004; Fine et al., 2006; Shen et al., 2008; Rafiee & Hall, 2011; Trakhtenbrot & Netzer, 2012), is based on a combination of two basic ingredients (Vestergaard, 2002; Peterson et al., 2004). First, reverberation mapping (RM) experiments provide an empirical relation between the BLR size and the AGN continuum luminosity ($R_{\rm BLR} = K'(\lambda L_\lambda)^\alpha$, with $\alpha \sim 0.5 - 0.7$; see Kaspi et al. 2000, 2005; Bentz et al. 2009, 2013, and references therein). Second,

the gas in the broad line region (BLR) is assumed to be virialized (as suggested by several empirical studies, e.g., Peterson & Wandel, 1999; Onken et al., 2004) . After taking the line width of the BLR lines as a natural estimation of the virial velocity of the gas in the BLR ($V_{\rm BLR}$), one may obtain the mass from the virial relation:

$$M_{\rm BH} = fG^{-1}R_{\rm BLR}V_{\rm BLR}^2 = K(\lambda L_\lambda)^\alpha {\rm FWHM}^2 \quad (2.2.1)$$

where $K = K'G^{-1}f$ and f is a general geometrical function which correct for the unknown structure and inclination to the line of sight. f can be determined experimentally by requiring RM-$M_{\rm BH}$ estimations to be consistent, on average, with those predicted from the $M_{\rm BH}$-bulge stellar velocity dispersion ($M_{\rm BH}$-σ_*) relation of local galaxies where $M_{\rm BH}$ have been dynamically estimated (e.g. Onken et al., 2004; Woo et al., 2010; Graham et al., 2011; Graham, 2015; Woo et al., 2015). In this chaper, we assume $f = 1$, which is appropriate for the FWHM $M_{\rm BH}$ (Hβ) estimates (Woo et al., 2015). However, in addition to the still large uncertainty in this value (50%), f can also be different for different lines and could even depend on luminosity and/or line properties (e.g. equivalent widths, line offsets FWHM Shen, 2013). We come back to this issue in chapter 4.

Among the RM-based $R_{\rm BLR} - L$ relations, the most reliable one is the $R_{\rm BLR}$ (Hβ) – L_{5100} relation, which is the only one based on a large number of sources, with $L_{5100} \lesssim 10^{46}\,{\rm erg\,s^{-1}}$. Thus, the $M_{\rm BH}$ determination based on other lines and luminosities at other wavelengths needs to be re-calibrated to match $M_{\rm BH}$ measurements based on Hβ and L_{5100}. Particularly, C IV λ1549, hereafter C IV, (e.g. Vestergaard & Peterson, 2006; Park et al., 2013), Mg II λ2798, hereafter Mg II, (e.g. McLure & Jarvis, 2002; Vestergaard & Osmer, 2009; Wang et al., 2009; Trakhtenbrot et al., 2011; Shen & Liu, 2012; Trakhtenbrot & Netzer, 2012) and Hα (e.g. Greene & Ho, 2005; Xiao et al., 2011; Shen & Liu, 2012) have been re-calibrated accordingly, and are widely used lines to determine $M_{\rm BH}$ at high redshifts.

Earlier $M_{\rm BH}$ recalibrations based on Mg II and Hα have showed good agreement and low scatter with Hβ-based $M_{\rm BH}$ calibration (Greene & Ho, 2005; Xiao et al., 2011; Trakhtenbrot & Netzer, 2012). However, $M_{\rm BH}$ recalibrations using the C IV line are more problematic, compared with those based on lower-ionization lines. First, the correlation between the widths of C IV and the other lines was shown to be weak, or indeed insignificant, and to present a large scatter, in many AGN samples (e.g., Baskin & Laor, 2005; Netzer et al., 2007; Shang et al., 2007; Shen et al., 2008; Fine et al., 2010; Ho et al., 2012; Shen & Liu, 2012; Tilton & Shull, 2013). Moreover, about 40% of the objects have FWHM (C IV) $\lesssim$ FWHM (Hβ), in contrast to the expectations from RM experiments and the virial assumption, that suggest FWHM (C IV) $\simeq 2 \times$ FWHM (Hβ) (see detailed discussion in TN12, and additional samples in Ho et al. (2012); Shen & Liu (2012); Tilton & Shull (2013)). Second, significant blueshifts of the *entire* C IV profile (i.e., not necessarily a specific sub-component of the line), reaching several 1000s ${\rm km\,s^{-1}}$, are ubiquitously measured in the vast majority of AGN (Richards et al., 2002; Baskin & Laor, 2005; Shang et al., 2007; Richards et al., 2011; Trakhtenbrot & Netzer, 2012). Some of these findings were explained either by a disc outflow wind (e.g.

Gaskell, 1982; Sulentic et al., 2007; Richards et al., 2011) or, alternatively, by scattering off an in-falling medium in the innermost C IV-emitting regions, which would produce the C IV blueshifts (e.g. Kallman & Krolik, 1986; Goosmann & Gaskell, 2007; Gaskell, 2009; Gaskell & Goosmann, 2013). Finally, the detailed re-analysis of the RM data for C IV performed by Denney (2012) found that the (narrowest) core of the broad C IV line does not reverberate in response to continuum variability. This implies that the *outermost* C IV emitting regions may not be virialized, either. All this leads to the conclusion that the simplified models and prescriptions discussed above may be incorrect, or at least incomplete, for some lines.

The $M_{\rm BH}$ determination is also subjected to several uncertainties, related to the limitations of spectral analysis, and/or the need to make several assumptions regarding the universality of some AGN properties. The former includes the blending of neighbouring emission and/or absorption features; incorrect determination of the continuum emission (Shang et al., 2007, hereafter S07); poor statistics due to non-homogeneous or small nature of the sample under study (e.g. Ho et al., 2012); poor data quality (e.g., Denney et al., 2013; Tilton & Shull, 2013); and measurements obtained from non-simultaneous data (see e.g. Shen & Liu, 2012; Marziani et al., 2013a). The latter, somewhat more fundamental uncertainties, include non virial gas motion; the orientation of the (generally non-spherical) BLR with respect to the line-of-sight (Runnoe et al., 2014; Shen & Ho, 2014; Brotherton et al., 2015b); and the extrapolation of the $R_{\rm BLR} - L$ relations to luminosities which are well beyond the range probed by RM experiments.

There have been many efforts to improve single-epoch $M_{\rm BH}$ determinations, addressing some of the aforementioned limitations (e.g. Greene & Ho, 2005; Vestergaard & Peterson, 2006; Fine et al., 2008; Wang et al., 2009; Fine et al., 2010; Xiao et al., 2011; Shen & Liu, 2012; Trakhtenbrot & Netzer, 2012; Marziani et al., 2013a; Park et al., 2013; Runnoe et al., 2013; Brotherton et al., 2015a; Zuo et al., 2015). Trakhtenbrot & Netzer (2012, hereafter TN12) combined Sloan digital sky survey archival data (SDSS; Abazajian et al., 2009) with smaller surveys and samples to improve earlier Mg II-based $M_{\rm BH}$ prescriptions (e.g., McLure & Jarvis, 2002; McLure & Dunlop, 2004; Wang et al., 2009), by assuming virialization of the Mg II emitting clouds. As mentioned above, the TN12 study emphasized the fact that a large fraction of AGN show FWHM (C IV) $<$ FWHM (Hβ). Marziani et al. (2013a) (hereafter M13) also used SDSS data to perform an Eigenvector 1 analysis (Boroson & Green, 1992), and to separate the population into "population A" (FWHM (Hβ) $< 4000\,{\rm km\,s^{-1}}$) and "population B" (FWHM (Hβ) $> 4000\,{\rm km\,s^{-1}}$) sources. They suggested that Hβ- and Mg II-based $M_{\rm BH}$ estimates in population B sources could be systematically overestimated due to a red-shifted, extremely broad emission component. The study ofShen & Liu (2012) combined SDSS optical observations of high-z objects ($1.5 \lesssim z \lesssim 2.2$) with follow up FIRE-IR observations, which allowed them to compare and recalibrate the C IV, Mg II, Hβ and Hα $M_{\rm BH}$ relations as well as contrast them with previous calibrations. While they found that FWHM(Mg II) correlates well with the Balmer lines, the FWHM(C IV) does not show such correlations and is not a reliable viral mass es-

timator. The Shen & Liu (2012) results are however subjected to low quality SDSS data, non homogeneous sample selection and non simultaneous observations. Ho et al. (2012) obtained simultaneous UV, optical and infrared X-Shooter spectra for 7 objects at $1.3 \lesssim z \lesssim 1.6$, resulting in similar conclusions regarding the usability of Mg II-based $M_{\rm BH}$ estimates, and the limitations associated with C IV.

The studies of (Denney et al., 2013, hereafter D13) and Tilton & Shull (2013) claimed that in spectra of limited S/N and/or spectral resolution, FWHM(C IV) measurements are underestimating the "real" line widths, in objects with strong intrinsic absorption features that cannot be deblended from the emission lines. This would partially explains the TN12 finding that about 40% of the objects shows C IV profiles narrower that Hβ profiles. However, objects with no evidence of absorption features, and yet "intrinsic" line widths with FWHM(C IV)<FWHM(Hβ) are known to exist (e.g., Corbin & Boroson, 1996). After correcting for intrinsic C IV absorption, D13 claimed that although FWHM(C IV) still does not correlate well with FWHM(Hβ), σ(C IV) shows a strong correlation with σ(Hβ) and can safely be used for C IV based $M_{\rm BH}$ determinations. Based on these results, (Park et al., 2013) obtained high quality data in 39 out of 45 objects of the RM experiments campaign and improved the Vestergaard & Peterson (2006) C IV-based $M_{\rm BH}$ estimator based on the σ(C IV). Both D13 and (Park et al., 2013) used non homogeneous and multi-epoch samples that could affect their results. In addition, $\sigma_{\rm line}$ measurements are highly dependent on the continuum determination method (see discussion in (Peterson et al., 2004)).

Recently, Runnoe et al. (2013) (hereafter R13) and Brotherton et al. (2015a) used a sample of 85 low-redshift ($0.03 < z < 1.4$) and low-luminosity ($43.37 < \log L_{5100} < 46.45$) AGN with quasi-simultaneous UV and optical spectra to propose a method to rehabilitate C IV for $M_{\rm BH}$ determination, based on a correlation that they found between the Si IV+O IV]$-$C IV line peak intensity ratio and the H$\beta-$C IV FWHM ratio. This allowed these authors to predict FWHM(Hβ) from measurements of the Si IV+O IV] emission. These studies suggested that this correlation may be driven by the so-called Eigenvector 1.

In this work, we use X-shooter high-quality observations that combines simultaneous UV, optical and infrared spectroscopy of a unique sample of AGN at z$\sim$1.55, selected by both their $M_{\rm BH}$ and Eddington ratio, $L/L_{\rm Edd}$ as described in Capellupo et al. (2015) (hereafter paper I). Selecting objects at this redshift allows simultaneous observations of Hα, Hβ, Mg II and C IV which is optimal for comparing the various mass determination methods. In Paper I, we showed that the accretion-disc continuum of most of the objects (25 out of 30) can be successfully modelled by a geometrically thin, optically thick Shakura-Sunyaev accretion discs (Shakura & Sunyaev, 1973, hereafter SS73) . The models were taken from Slone & Netzer (2012) who include several improvements upon the SS73 model, such as GR effects and a detailed treatment of the Comptonization in the disc atmosphere. Paper I shows that most earlier attempts to fit accretion disc (AD) spectra to AGNs failed because of the limited wavelength coverage and/or non-simultaneous observations. The continuation of this work, that includes 9 more

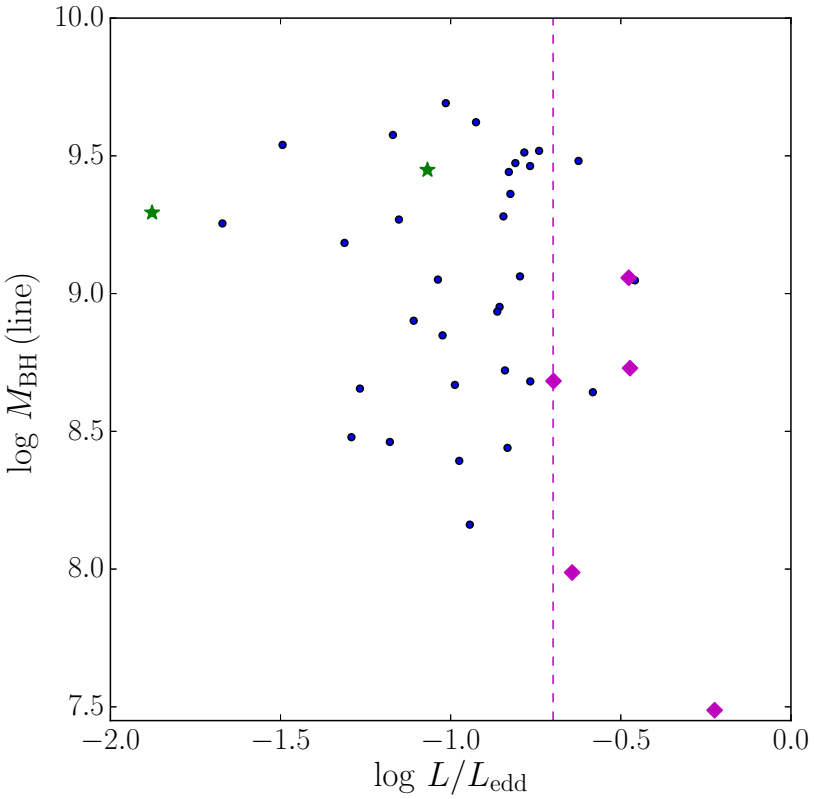

Figure 2.2.1: $M_{\rm BH}$ vs $L/L_{\rm Edd}$ using the values we obtained in this chapter. Green stars and magenta diamonds represent the broad absorption line quasars (BALQSO) and the broad-Mg II respectively (as defined in §2.4.3.4) . The magenta dashed vertical line represents $L/L_{\rm Edd}$=0.2.

sources and a more comprehensive analysis, is described in Capellupo et al. (2016, in prep.), hereafter Paper III) which is published in this volume.

The purpose of the present chapter is to evaluate BH mass measurements based on different emission lines, as derived from our unique sample of X-shooter spectra. We also aim to provide to the community $M_{\rm BH}$ correction factors that do not depend on the exact shape of the underlying continuum. The chapter is structured as follows. In section 2.2 we describe the sample. In section 2.3 we first introduce the *local* and *global* thin disc continuum approaches and describe the fitting procedures we follow to model the continuum, emission lines, iron pseudo continuum and Balmer continuum. In section 2.4 we present and discuss the main results and in section 3.4 we list the main conclusions of our work. Throughout this chapter we assume a flat ΛCDM cosmology with the following values for the cosmological parameters: $\Omega_\Lambda = 0.7$, $\Omega_{\rm M} = 0.3$ and $H_0 = 70\,{\rm km\,s^{-1}\,Mpc^{-1}}$.

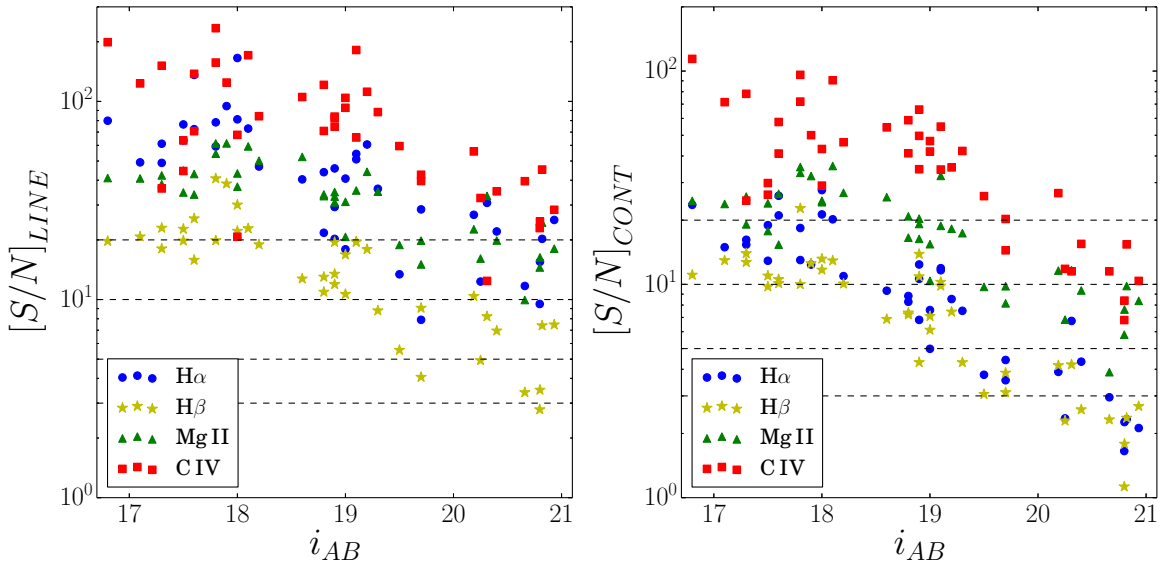

Figure 2.2.2: Signal to noise ratios (S/N) measured at the peaks of each of the main broad emission lines (left), and over the corresponding nearby continuum bands (right), plotted against optical brightness, $i_{\rm AB}$. The black dashed lines represent, from bottom top, S/N equal to 3, 5, 10 and 20.

2.2 Sample, Data and Analysis

The analysis presented in this chapter is based on a sample of luminous, type-I AGN in a narrow redshift range around $z \simeq 1.55$, for which we have obtained high signal to noise (S/N) single epoch spectroscopic observations using the X-Shooter instrument on the Very Large Telescope. The 39 sources span a range in brightness of $i_{\rm AB} \sim 16.8 - 20.9$. The sample selection, data acquisition and reduction for the 30 brightest sources were described in detail in paper I, and information about 9 other sources, obtained in ESO program 092.B-0613, is provided in Paper III. Here we only briefly highlight a few essential aspects.

The sample has been selected from the seventh data release of the SDSS (Abazajian et al., 2009) to homogeneously map the parameter space of $M_{\rm BH}$ and $L/L_{\rm Edd}$. For the purposes of target selection, these quantities were initially obtained by spectral fitting of the Mg II broad emission line in the SDSS spectra as part of the large compilation described in TN12. In Figure. 2.2.1 we show $M_{\rm BH}$ vs $L/L_{\rm Edd}$ using updated values calculated in this chapter based on the Hα broad emission line and following the procedure that we describe in section 2.4.4.

At the chosen redshift range of the sample, X-Shooter covers the rest-frame wavelength from about 1200Å to 9200Å. This broad spectral coverage has allowed us, after correction for Galactic extinction, to successfully model and constrain the observed Spectral Energy distributions (SEDs). As shown in Papers I and III, we obtain sat-

isfactory thin AD model fits to 37 sources, 6 of which require an intrinsic reddening correction for a satisfactory fit. The wide wavelength coverage, together with the homogeneous selection of the sample in the $M_{\rm BH} - L/L_{\rm Edd}$ plane, enables us to test the performance of the single epoch black hole mass estimators for the Hα, Hβ, Mg II and C IV lines and estimate the systemic bias induced when the physical SED is unknown.

In Figure 2.2.2 we show the the signal to noise ratios (S/N) for our X-Shooter spectra, measured at the peaks of each of the main emission lines under study, as well as at the corresponding continuum bands, as a function of $i_{\rm AB}$. We note that, even in the spectral region which overlaps with the available SDSS spectra, the X-Shooter data provide a significant improvement in terms of S/N and spectral resolution (see an example in Fig. A.A.1, described in appendix §A.1). All the sources have fairly high S/N ($\gtrsim 20$) at the peaks of the Mg II and C IV lines and the adjacent continuum bands. However, this is not the case for Hα and Hβ. The continuum bands adjacent to Hα are much noisier. Most of the objects have $S/N < 20$, and for those with $i_{\rm AB} > 18.5$, the ratio is below 10. Nevertheless, we are able to obtain reliable Hα line measurement because most objects have fairly high S/N at their Hα line peak (34 out of 39 object have $S/N \gtrsim 20$ and all of them have $S/N \gtrsim 8$). Moreover, the relevant continuum bands around Hα have low levels of contamination from iron or other, unresolved spectral features. Consequently, even a moderate continuum S/N (i.e., $\gtrsim$3) is enough to have reliable Hα fits. There are however 4 objects where $S/N < 3$ and their line measurements, especially their FWHM(Hα) are somewhat uncertain.

Unfortunately, the Hβ line measurements are more problematic. In addition to the fact that Hβ is the weakest of the lines of interest, we can also see from Fig. 2.2.2 that the relevant continuum band in 21 out of 39 objects have $S/N \lesssim 10$, and 14 of them are actually below $S/N \sim 5$. Near infrared (NIR) telluric absorption is another issue that could also crucially affect Hβ line measurements. The spectral regions with known low atmospheric transmission in the NIR, between Å and between 13000Å to 15000Å typically translate to rest-frame bands at 4200-4500Å and 5300-5800Å at the redshift of the sample. These bands are known to show strong iron emission which are suppressed by such telluric absorption (see the example spectrum in Fig. 2.2.3 around 4400 and 5500Å). The combined effect of the telluric absorption and the limited S/N achieved for the fainter sources severely affects the correct modeling of their iron emission around Hβ. This, in turn, significantly increases the measurement uncertainties related to Hβ, ultimately making Hβ measurements of faint objects less reliable.

Fortunately, the Hα line shows very similar profiles to Hβ (e.g. Greene & Ho, 2005) which is in accordance with the expected radial ionization stratification of the BLR (Kaspi et al., 2000). Based on these results, we can probe several aspects related to the Hβ line using the more reliable Hα measurements.

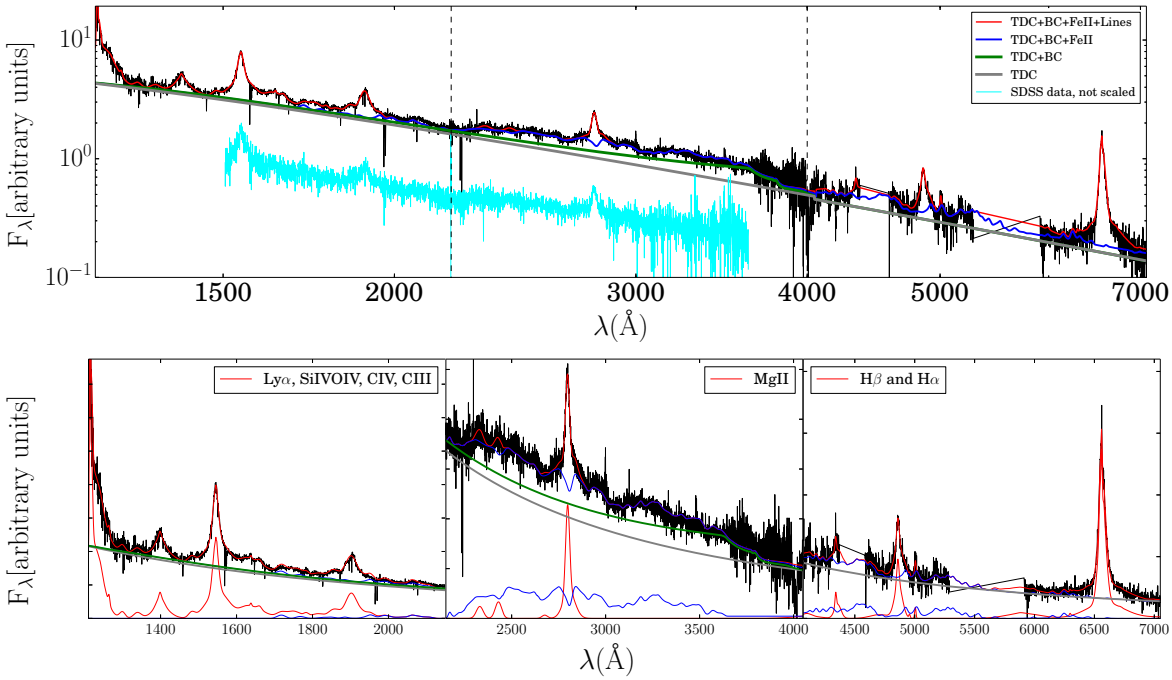

Figure 2.2.3: The rest-frame X-Shooter spectrum (top) and main emission line complexes (bottom), over the three X-Shooter bands (UV:left, Optical:middle, Infrared:right), for the source J0143-0056 and the corresponding line fitting using the ***global* thin disc continuum approach**. The observed spectrum is shown in black. The best-fitting continuum is shown in gray. The blue lines represent the additional best-fit iron emission. The red lines represent the additional best-fit models for the emission lines. For the sake of comparison we show the SDSS of the source in cyan.

2.3 Spectral Decomposition

In this section we describe the analysis procedures we used to model the X-Shooter spectra and to obtain continuum and line emission measurements. We discuss separately the analysis of emission corresponding to the continuum, the blended iron features, and the emission line components. All the spectral modelling is done by employing the Levenberg-Marquardt algorithm for χ^2 minimization, using the `python` based spectroscopic analysis package `pyspeckit` (Ginsburg & Mirocha, 2011). The fitting is preformed in the rest frame, after shifting the spectra using the improved SDSS redshifts provided by Hewett & Wild (2010). We chose to use these redshifts, instead of using the O III] λ5007 line observed within the X-Shooter data, because of the limited quality of the relevant data and modelling of the Hβ-O III] λ5007 spectral region (see §2.2) and the weak or absent O III] λ5007 emission in many of our sources.

2.3.1 Continuum Emission

We adopt here two different approaches to account for the continuum emission of the AGN,which we refer to as the *local* and *global* (thin disc) continuum approaches. The *local* continuum attempts to account for the usual approximation of the continuum emission by a single power law when the observed spectrum is limited to a narrow wavelength range. The *global* thin disc continuum, on the other hand, corresponds to the more physically-motivated AD model, that was obtained through a Bayesian analysis taking advantage of our wide spectral wavelength coverage (see paper I). A comparison of the measurements obtained with both approaches will allow us to quantify the possible bias imposed by ignoring the real SED shape, when wide-enough wavelength coverage is not available.

2.3.1.1 Local continuum approach and Biases

The *local* continuum approach consists of separately fitting the continuum emission surrounding each of the lines of interest. For every source in the sample, each of these continua is approximated by a single power law, which connects neighbouring spectral windows known to have little line contamination. Our specific choice of such line-free continuum bands rely on several similar works (S07,TN12), and are listed in Table 2.1.

The most important bias in the *local* approach is that it commonly uses non real continuum windows that are affected by either (1) weak line emission flux such as the continuum window at 1700Å that is used for C IV line fitting, (2) iron continuum emission that affects continuum windows around 2600Å and 3000Å, as well as those around 4650Å and 5100Å that are respectively used for Mg II and Hβ line fitting and finally, (3) the Balmer continuum (BC) emission, at $\lambda < 3647$ Å, which can significantly

Table 2.1: *Spectral pseudo-continuum windows used for our line fitting procedure under the local continuum approach.* [1]*For each object, we manually adjusted the continuum bands, using the listed wavelength ranges as a reference.*

Line Complex	Continuum windows[1]	
Si IV+O IV]	1340-1360Å	1420-1460Å
C IV	1420-1460Å	1680-1720Å
C III]	1680-1720Å	1960-2020Å
Mg II	2650-2670Å	3030-3070Å
Hβ	4670-4730Å	5080-5120Å
Hα	6150-6250Å	6950-7150Å

affect Mg II measurements, and to a lesser extent even C IV measurements. All these biases are in the direction of an overestimation of the continuum emission when the *local* approach is used which will translate into FWHM and line flux underestimation.

An additional bias comes from the shape of the SED, particularly at the turn over of most spectra at around 1000-1500Å (exact wavelengths depend on BM mass, spin and accretion rate, see Papers I and III). The simple power-law approximation to the SED does not remain valid over this range and may lead to measurement biases of the line profile properties of C IV and Si IV+O IV] λ1400 (hereafter Si IV+O IV]). In this chapter we use our AD SED fittings to quantify these biases.

2.3.1.2 Thin disc continuum approach

The *global* AD approach is based on the best fits from the thin-accretion-disc continuum models obtained for each of the sources in Papers I and III (see also Appendix C.1). For the analysis in this chapter we do not consider the two objects with no satisfactory fits to the thin disc continuum model.

As explained in paper I and III, the SEDs of the AD models used in this work are determined by $M_{\rm BH}$, the accretion rate ($\dot{M}$), the spin (a_*) and the inclination of the disc with respect to the line-of-sight (θ). We adopted a Bayesian procedure to fit the thin AD model spectra to the observed X-shooter SEDs. $M_{\rm BH}$ and $\dot{M}$ were taken as priors with Gaussian distributions centred on the observed values, obtained from Hα and L_{6200} measurements (following the procedures described in this chapter), and with standard deviations of 0.3 and 0.2 dex, respectively (see Appendixes C.2 and C.3 for further details).

Within the *global* continuum approach we also consider the BC emission that peaks near the Balmer edge (3647Å) and gradually decreases towards shorter wavelengths. The Balmer continuum model we used is based on calculations of the photo-ionization code ION (Netzer, 2006) with an H-atom containing 40 levels, solar abundances, hydrogen density of 10^{10}cm^{-3}, column density of 10^{23}cm^{-2} and ionization parameter of $10^{-1.5}$. The exact shape is insensitive to the exact value of these parameters and the

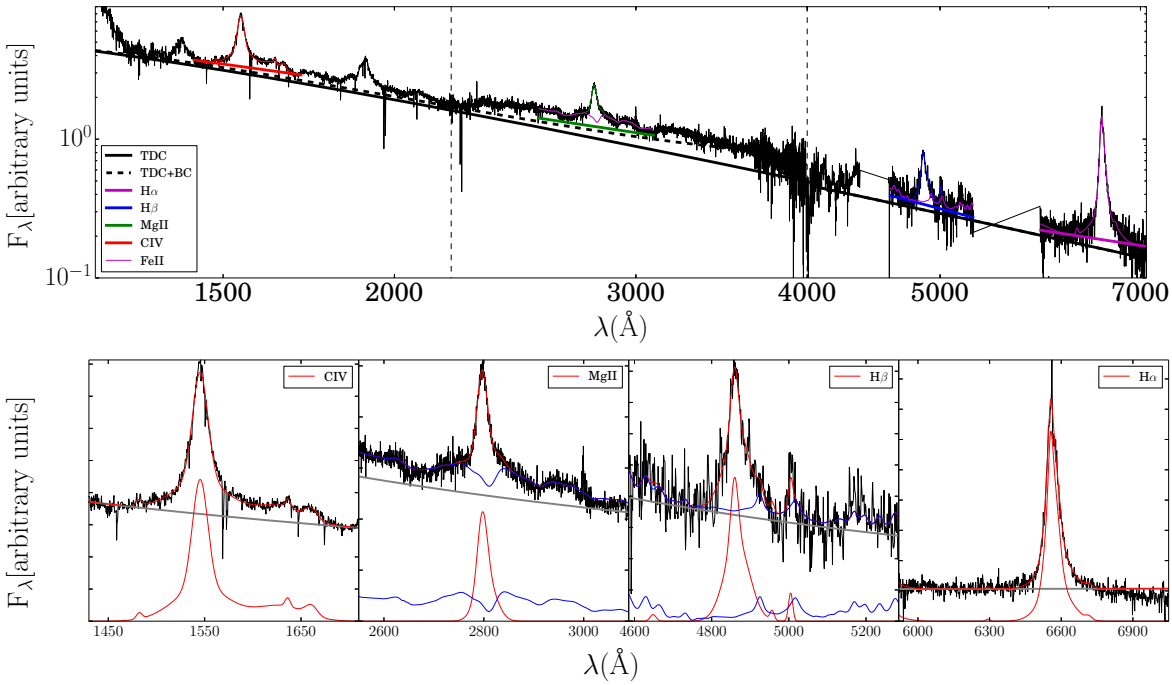

Figure 2.2.4: An example spectrum and spectral decomposition of one of the sources in our sample, J0143-0056 using the *local* approach. The top panel presents the rest-frame X-Shooter spectrum and the overall decomposition. The solid black solid line corresponds to the "thin disc" continuum, while the dashed black line illustrates the addition of the Balmer continuum. We highlight the spectral regions surrounding the most prominent broad emission lines (from left to right: C IV in red, Mg II in green, Hβ in blue, and Hα in magenta). The bottom panels show in detail the highlighted regions of the top panel as well as the individual *local* continuum determinations. Continuum fitting is in gray. Continuum plus iron emission fitting is in blue. Continuum plus, iron plus line fitting in red. Observed spectrum is in black.

normalization is done by direct fits to the observations.

An additional contribution to the continuum emission is due to starlight, mostly at wavelengths longer than about 6000Å. For our AGN sample such a contribution is marginal in 32 out of 39 objects and does not severely affect the continuum level and shape of the AGN SED as discussed in paper I and III (<3% at 6200Å). For the 7 fainter objects we used the method described in paper III which assumes a template from an 11 Gyr old stellar population to model the host galaxy emission. The scale factor of the template is determined from the ratio of the measured EW (Hα) and the median value of the EW (Hα) distribution of the 29 brightest objects, as discussed in paper III. The host galaxy contribution is subtracted before the thin disc continuum fitting for those objects which require this correction. We find that in this sub-sample the host galaxy contribution is between 6% and 50% at 6200Å and smaller than 3% at 3000Å. We also tested several stellar populations in the age range from 1 to 11 Gyr, but we find no significant changes in the corrected spectrum (see paper III for details).

Finally, combining the X-Shooter spectra obtained by three different arms (UV, Optical and NIR) may introduce additional uncertainties. As explained in Paper I, in most cases, the overlap and connection between the VIS and UVB arms are satisfactory, with no need for further adjustments but this is not the case for the VIS-NIR joint, as can be seen for J0043 in Fig. 2.2.3. For several objects, the slope of the VIS arm was adjusted based on comparison to SDSS (see Paper I for more details). We therefore allow our fitting to rescale the *global* continuum up to 10% in each of the regions covered by each arm (1200-2200Å, 2200-4000Å, 4000-9000Å) to take into account the arm calibration uncertainties.

2.3.2 Blended iron lines

For an adequate modeling of Hβ and Mg II line profiles it is crucial to first subtract the iron line emission, originating from a large number of blended features of Fe II and Fe III. Generally, this is done by choosing the best-fit broadened, shifted and scaled empirical iron line template. We constrain line center shifts to be smaller than 1000 km s^{-1} and broadening is constrained to the range 1000-20000 km s^{-1}. For the optical region around Hβ (4000-7000Å) we used the iron template from Boroson & Green (1992). For the UV region around Mg II (1700-3647Å) we initially used the Tsuzuki et al. (2006) template (hereafter T06). However, the fits obtained using this template was not satisfactory, mainly due to an over-estimation of the continuum emission. We therefore built a new iron template (see Apppendix A.2 and figure A.A.2) based on the spectrum of I Zw 1 reported by T06, which is a composite of their UV (HST) observation and the optical (KPNO) observation reported by Laor et al. (1997).

One of the main differences between the *local* and *global* approaches is that under the *local* approach different scaling factors for the UV iron template at each side of the Mg II line are required in order to guarantee an acceptable match to the observed spectrum. The scale factor in the red side of Mg II is found to be always larger than the one for the blue side, but by no more than 10%. This type of correction is not needed in the *global* approach, when the complete continuum model (AD+BC) is considered. Given that under the *local* approach the BC cannot be accounted for directly and that the BC is monotonically increasing from 2200 to 3647Å, we suspect that the larger scale factor in the red side of Mg II might be due to the BC and not to intrinsic changes in iron line emission.

2.3.3 Emission Line Measurements

For the emission line modeling we have followed a procedure similar to the one described in TN12 (see their appendix C) and Shang et al. (2007) In short, after removing the continuum emission (following either the *local* or *global* approaches) and the iron template, we model the prominent broad emission lines with two broad Gaussian

components. We allow for a range of line widths and shifts for each component, where the FWHM ranges between 1000 km s^{-1} and 10000 km s^{-1}and the line shifts are limited to $+/-1000$ km s^{-1} for the Hα, Hβ and Mg II lines, while for the C IV line we allowed blue-shifts of up to -3000 km s^{-1}. These different choices are motivated by the findings of several earlier studies (e.g., Vestergaard & Peterson (2006), S07, R13, Park et al. (2013)). In the case of doublet lines (C IV and Mg II), we used 4 Gaussians, forcing the two broad and two narrower components to have the same profiles and intensity, and the theoretical wavelength separation. We fixed the Mg II and C IV doublet intensity ratios to 1:1, suitable for optically thick line emission. For each of the Hα, Hβ and C IV lines we have also included a third Gaussian component when needed to account for the additional emission originating from the narrow line region (NLR). Each of these narrow components are modelled by a single Gaussian profile, their FWHM is constrained not to exceed 1300 km s^{-1}, and their line centres are tied to each other, with shifts of 400km s^{-1}, at most. We chose not to include a narrow component in the modeling of the Mg II and C IV lines (as in, e.g., Wills et al., 1993; Sulentic et al., 2007), since we found no significant difference in the Mg II measurements (or fit quality) when trying to include it.[1] For other, weaker emission lines (including He II1640, N IV1718, Si III]1892) we used only a single Gaussian component. These lines are not necessary for the purpose of the present work except for limiting the continuum placement.

All the Gaussian components we used are symmetric and defined by three parameters: peak flux density, FWHM, and central wavelength. We have made several simple, physically motivated simplifying assumptions, in order to minimize the number of free parameters: the Gaussian components of lines of the same species were forced to share an identical width; we have also tied together the relative shifts in the central wavelengths of some lines, based on their laboratory wavelengths; and assume line-intensity ratios for some lines based on their statistical weights (See Appendix A.3 and Table A.1 for further details on the different emission line parameters, their assumed ranges, inter-connections and delimitation of the emission line regions). Our line fitting procedure runs separately on each of the main emission line regions, while all the lines in each line region are fitted simultaneously.

Generally, the *global* (see Figure 2.2.3) and *local* (see Figure 2.2.4) continuum approaches follow the same line fitting procedures in terms of the number of components per emission line and the way they are tied together. One important difference is that in the *global* approach, the C III] and C IV line regions are considered a single region and are therefore fitted simultaneously. The reason for this is that under the *local* approach we take as continuum windows the region around 1700Å following the same procedure of previous works (e.g., S07, TN12, and references therein). However, this region is usually contaminated by weak emission lines like N IV1718, and consequently the thin disc continuum fit does not allow us to fit C IV and C III] independently.

In order to account for possible uncertainties in our spectral measurements, we per-

[1]For example, for C IV we find that a narrow component typically contributes $\sim 3\%$, and at most 6%, of the total line luminosity.

formed 100 Monte-Carlo realizations for each of the spectra. In each of these realizations, the flux density at each spectral pixel was altered from the observed value by a random, normally distributed value, assuming the corresponding level of noise (i.e., using the noise spectrum). From these sets of best-fit models we extracted, for each emission line, the line width FWHM, the velocity dispersion ($\sigma_{\rm line}$; following Peterson et al. (2004)), integrated luminosity (L), rest-frame equivalent width (EW), the luminosity at the peak of the fitted profile ($L_{\rm P}$) as well as its corresponding wavelength ($\lambda_{\rm P}$) and the offset of the line center (relative to the laboratory wavelength; Δv). The line offsets were calculated using the flux-weighted central wavelength of the broad line profile:

$$\Delta v = \left(\int \lambda f_{\lambda}\left(\text{line}\right) d\lambda / F\left(\text{line}\right) - \lambda_0 \right) c/\lambda_0 \tag{2.2.2}$$

where $f_{\lambda}\left(\text{line}\right)$ is the flux density of the broad line profile at λ; $F\left(\text{line}\right)$ is the integrated broad line flux, $F\left(\text{line}\right) = \int f_{\lambda}\left(\text{line}\right) d\lambda$; λ_0 is the laboratory wavelength of the line; and c is the speed of light.

The best-fit values for all these parameters were taken from the medians of the parameter distribution, and the corresponding uncertainties were estimated from the central 68% percentiles. This "re-sampling" approach for the estimation of measurement-related uncertainties was used in several recent studies of spectral decomposition of AGN UV-optical spectra (e.g., Shen & Liu, 2012). Based on our experience, such errors reflect the true uncertainties related to measuring emission line profiles, while those provided by the (statistical) spectral fitting procedure itself tend to underestimate the "real" uncertainties.

The measured parameters, and uncertainties, for the most prominent emission lines under the *local* approach are summarized in Tables 2.2 and 2.3.

2.4 Results and Discussion

2.4.1 Local versus global continuum measurements

In this subsection we compare the *local* and *global* continuum approaches in order to quantify the possible biases that are introduced when the real underlying shape of the continuum cannot be accurately established. As we will describe below in detail, our main conclusion is that *local* continuum measurements of FWHMs, continuum luminosities and, consequently, black hole masses present very small but systematic offsets with respect to the corresponding *global* continuum measurements.

Table 2.2: *Monochromatic continuum luminosities ($\lambda L\,[\lambda]$), line peak luminosity densities ($L_{\rm P}$) and line offsets (Δv), under the* **local** *approach..*

Object	log (λL_λ/erg s^{-1})								log (L_{line}/erg s^{-1})		log ($L_{\rm P}$/erg s^{-1} Å)						-$\Delta\,v$ [km s^{-1}]							
name	1450	Δ	3000	Δ	5100	Δ	6200	Δ	Hα	Δ	Si IV+O IV]	Δ	C IV	Δ	C III]	Δ	C IV	Δ	Mg II	Δ	Hβ	Δ	Hα	Δ
J1152+0702	46.81	0.01	46.55	0.01	46.11	0.01	46.17	0.01	44.8	0.01	43.15	0.02	43.43	0.01	42.94	0.16	-2452.68	104.71	-97.53	101.35	1042.62	148.83	-79.15	70.63
J0155-1023	46.62	0.01	46.41	0.01	46.13	0.01	46.07	0.01	44.87	0.01	43.17	0.01	43.29	0.01	42.88	0.07	-2294.86	123.19	-139.62	75.73	510.34	86.22	-172.03	90.25
J0303+0027	46.53	0.01	46.36	0.01	46.03	0.01	45.99	0.01	44.79	0.02	43.01	0.02	43.21	0.01	42.49	0.27	-484.41	61.98	157.4	123.36	1094.57	53.3	-386.05	193.83
J1158-0322	46.52	0.01	46.35	0.01	46.08	0.01	45.99	0.01	44.82	0.01	43.02	0.03	43.22	0.01	42.83	0.05	-1775.53	40.87	-4.04	66.53	-1067.76	168.86	-534.82	64.61
J0043+0114	46.46	0.01	46.26	0.01	45.93	0.01	45.89	0.01	44.68	0.01	42.9	0.03	43.11	0.01	42.87	0.06	-2823.52	102.51	-340.23	67.91	-583.57	94.8	-330.63	51.76
J0209-0947	46.56	0.01	46.38	0.01	46.09	0.01	46.01	0.01	44.86	0.01	43.05	0.01	43.47	0.01	42.95	0.03	-1534.54	19.99	-109.47	74.22	668.06	296.98	-328.73	105.64
J0842+0151	46.39	0.01	46.21	0.01	45.79	0.04	45.78	0.02	44.74	0.02	42.97	0.05	43.24	0.01	42.81	0.08	-2393.53	53.53	-249.3	65.66	488.33	346.79	-545.4	222.08
J1002+0331	46.55	0.01	46.29	0.01	45.99	0.01	45.97	0.01	44.83	0.01	42.02	0.39	43.34	0.03	43.27	0.02	-1425.91	67.7	-224.11	84.88	771.98	121.85	127.18	72.02
J0323-0029	46.51	0.01	46.27	0.01	45.95	0.01	45.92	0.01	44.81	0.01	43.03	0.02	43.37	0.01	43.14	0.02	278.52	85.01	-477.62	92.79	674.22	97.41	-141.79	107.94
J0152-0839	46.31	0.01	46.11	0.01	45.83	0.01	45.69	0.01	44.56	0.01	42.7	0.02	43.02	0.01	42.57	0.09	-2152.61	48.73	-245.03	100.87	-523.93	142.87	-512.4	104.87
J0941+0443	46.27	0.01	46.08	0.01	45.79	0.02	45.74	0.01	44.68	0.01	42.73	0.02	43.11	0.01	42.6	0.09	306.62	92.72	-27.67	138.44	-174.21	401.45	-191.83	45.64
J0148+0003	46.4	0.01	46.38	0.01	46.11	0.02	46.07	0.01	44.97	0.01	42.85	0.07	43.05	0.08	42.92	0.06	-933.05	104.45	-60.68	95.14	799.06	63.93	-360.83	64.41
J0934+0005	46.15	0.01	45.92	0.01	45.68	0.01	45.62	0.01	44.43	0.01	42.7	0.02	42.77	0.02	42.62	0.06	-2156.93	71.57	-155.35	80.23	556.3	140.5	-449.29	174.13
J0019-1053	45.89	0.01	45.78	0.01	45.4	0.01	45.39	0.01	44.26	0.01	42.33	0.03	42.79	0.01	42.35	0.09	-571.41	38.73	269.01	71.92	789.89	108.23	725.37	59.2
J0850+0022	45.8	0.01	45.73	0.01	45.52	0.01	45.48	0.01	44.14	0.01	42.8	0.02	42.85	0.02	42.53	0.12	-2754.99	225.22	-41.26	125.73	316.41	196.98	-1044.97	142.74
J0404-0446	45.9	0.01	45.72	0.01	45.62	0.03	45.46	0.02	43.92	0.05	42.79	0.02	42.71	0.01	42.51	0.12	-3440.87	99.7	-214.1	86.61	-435.09	451.73	-560.96	145.65
J1052+0236	45.78	0.01	45.7	0.02	45.44	0.02	45.39	0.02	44.21	0.03	42.14	0.14	42.59	0.06	42.07	0.07	-70.84	116.54	263.36	147.25	1059.5	215.22	475.95	166.7
J0223-0007	45.86	0.01	45.67	0.01	45.32	0.06	45.28	0.05	44.19	0.04	42.4	0.02	42.7	0.01	42.36	0.03	-1568.3	56.19	7.56	99.2	-481.33	692.18	-404.17	271.04
J0240-0758	45.89	0.01	45.76	0.01	45.43	0.02	45.36	0.01	44.32	0.01	42.51	0.02	42.98	0.01	42.53	0.03	-293.37	33.52	185.33	57.24	478.62	212.48	710.93	26.89
J0136-0015	45.80	0.01	45.64	0.01	45.28	0.03	45.2	0.01	44.12	0.02	42.48	0.13	42.59	0.01	42.33	0.04	-2756.36	79.89	-318.27	89.48	656.58	232.12	-648.21	114.67
J0213-1003	46.2	0.01	45.93	0.01	45.64	0.02	45.58	0.01	44.39	0.01	42.98	0.05	42.98	0.01	42.65	0.04	-1739.83	261.66	-27.74	144.11	-360.87	278.85	-666.62	72.89
J0341-0037	45.73	0.01	45.56	0.01	45.3	0.03	45.22	0.03	44.12	0.03	42.39	0.02	42.6	0.01	42.33	0.03	-2330.08	129.88	-222.25	102.02	-840.53	688.41	-536.48	261.4
J0143-0056	45.72	0.01	45.52	0.01	45.18	0.02	45.1	0.04	43.99	0.04	42.35	0.03	42.73	0.01	42.24	0.06	-524.69	40.00	264.87	77.58	396.95	199.42	587.99	149.68
J0927+0004	45.74	0.01	45.51	0.01	45.18	0.02	45.18	0.01	44.04	0.02	42.33	0.03	42.71	0.01	42.17	0.09	486.01	220.26	72.03	72.29	1010.25	278.06	345.72	94.13
J0213-0036	45.64	0.01	45.46	0.01	45.15	0.02	45.12	0.02	44.11	0.01	42.29	0.05	42.86	0.01	42.29	0.04	-643.71	19.59	137.23	103.97	174.78	261.3	27.18	206.44
J1050+0207	45.61	0.01	45.43	0.02	45.12	0.06	44.94	0.03	43.89	0.03	41.89	0.07	42.36	0.03	41.92	0.07	-591.26	218.74	443.37	152.79	122.92	566.2	526.65	337.22
J0948+0137	45.43	0.01	45.3	0.02	45.03	0.04	45.02	0.05	43.96	0.03	42.09	0.11	42.53	0.02	42.13	0.08	-961.26	106.85	176.82	190.95	-62.	414.8	-424.22	354.05
J0042+0008	45.42	0.01	45.21	0.01	44.87	0.05	44.76	0.03	43.67	0.04	41.95	0.2	42.21	0.08	41.81	0.02	-1683.76	138.32	-312.02	99.56	697.42	205.71	26.51	160.33
J1013+0245	45.38	0.01	45.18	0.02	45.08	0.04	45.01	0.03	43.59	0.05	42.03	0.07	42.19	0.01	41.95	0.09	-1110.04	244.02	-113.76	240.13	-1167.31	1020.54	-197.79	213.94
J1021-0027	44.96	0.02	44.97	0.01	44.78	0.05	44.89	0.02	43.88	0.01	42.02	0.04	42.35	0.25	41.83	0.01	206.99	527.72	-219.52	49.35	1100.26	105.14	-925.29	101.62
J0038-0019	45.1	0.01	44.97	0.01	44.78	0.04	44.81	0.02	43.45	0.02	41.51	0.12	42.21	0.05	41.65	0.04	51.63	92.82	18.95	162.72	-647.1	338.03	445.16	83.86
J0912-0040	45.11	0.01	44.93	0.01	44.71	0.12	44.73	0.05	43.44	0.04	41.67	0.14	42.17	0.38	41.58	0.09	-1396.33	110.18	-79.1	162.0	600.7	567.47	-116.43	117.77
J1048-0019	45.09	0.02	44.88	0.01	44.57	0.08	44.32	1.9	43.2	0.25	41.69	0.1	42.22	0.21	41.53	0.06	-322.86	79.87	-190.12	165.63	241.99	335.73	270.64	155.81
J1045-0047	44.92	0.03	44.79	0.02	44.31	0.06	44.43	0.05	43.37	0.03	41.14	0.37	42.02	0.23	41.36	0.07	-990.37	115.71	-37.63	155.99	-158.89	564.79	66.88	89.9
J0042-0011	44.87	0.02	44.77	0.01	44.63	0.07	44.47	0.05	43.06	0.04	41.62	0.09	41.92	0.17	41.37	0.02	-2104.9	83.54	-341.65	209.76	327.91	322.67	-169.64	73.31
J1046+0025	44.97	0.01	44.7	0.02	44.42	0.1	44.41	0.1	42.48	0.12	41.66	0.09	42.07	0.34	41.43	0.05	-1255.21	69.88	-791.01	175.69	-801.5	452.36	-1299.09	125.12
J0930-0018	44.81	0.02	44.66	0.02	44.36	0.97	44.11	0.11	42.95	0.26	41.4	0.25	41.98	0.28	41.38	0.03	-1115.71	371.44	-878.01	115.31	-1023.75	423.79	-996.61	147.11
J1108+0141	46.53	0.01	46.47	0.01	46.2	0.01	46.09	0.01	44.82	0.01	43.1	0.03	42.95	0.02	42.93	0.06	-523.43	73.63	-729.27	47.84	1298.13	19.36	-354.62	45.75
J1005+0245	45.96	0.01	46.05	0.01	45.87	0.01	45.89	0.01	44.74	0.01	42.57	0.13	42.75	0.04	42.79	0.03	-1202.56	828.92	11.81	79.42	1257.99	96.71	126.41	100.23

Table 2.3: *Broad line widths and corresponding mass estimates, under the* **local** *approach..*

Object	FWHM [$\mathrm{km\,s^{-1}}$]								σ_{line} [$\mathrm{km\,s^{-1}}$]								$\log(M_{\mathrm{BH}}(\mathrm{FWHM})/\mathrm{M}_\odot)$									
name	C IV	Δ	Mg II	Δ	Hβ	Δ	Hα	Δ	C IV	Δ	Mg II	Δ	Hβ	Δ	Hα	Δ	C IV	Δ	Mg II	Δ	Hβ	Δ	$\mathrm{H}\alpha_{6200}$ [a]	Δ	$\mathrm{H}\alpha_{\mathrm{line}}$ [b]	Δ
J1152+0702	6573	133	3202	1356	4730	271	4283	240	3870	352	2165	179	4611	80	3186	247	9.65	0.02	9.47	0.04	9.44	0.06	9.48	0.05	9.32	0.06
J0155-1023	6582	92	3468	67	5458	140	4786	116	5553	132	2113	129	2602	50	4010	147	9.54	0.01	9.46	0.02	9.58	0.03	9.51	0.02	9.46	0.03
J0303+0027	5914	186	4790	136	7342	166	6230	100	3856	382	2519	220	3884	62	4898	309	9.39	0.03	9.7	0.03	9.77	0.02	9.69	0.02	9.64	0.02
J1158-0322	4836	72	3376	133	5192	408	4855	169	2679	52	1901	107	4517	348	4114	262	9.21	0.01	9.39	0.04	9.5	0.08	9.47	0.03	9.44	0.04
J0043+0114	7324	121	3380	93	4058	493	3227	123	3928	10	2509	204	5329	93	3633	83	9.54	0.02	9.34	0.03	9.19	0.12	9.06	0.04	9.01	0.04
J0209-0947	5032	56	2900	64	5124	278	4723	176	4031	60	2299	146	4314	331	3974	147	9.26	0.01	9.28	0.02	9.5	0.06	9.46	0.04	9.44	0.04
J0842+0151	6525	110	3952	128	5231	563	4956	56	3626	233	2045	166	4409	196	5901	137	9.39	0.02	9.45	0.03	9.32	0.12	9.36	0.02	9.42	0.02
J1002+0331	5017	440	2564	70	5465	596	4738	82	2446	42	1854	235	4000	126	3316	276	9.26	0.08	9.12	0.03	9.49	0.11	9.44	0.02	9.43	0.02
J0323-0029	5190	68	1890	69	2991	446	3127	668	3284	58	3207	48	3442	174	2955	189	9.26	0.01	8.84	0.04	8.94	0.14	9.05	0.22	9.05	0.21
J0152-0839	6481	70	3116	158	4306	340	4814	164	3754	349	2110	186	3871	228	5716	259	9.34	0.01	9.18	0.05	9.18	0.08	9.28	0.03	9.29	0.04
J0941+0443	7721	63	4218	286	6151	308	6520	121	3811	34	2949	95	3823	430	4161	142	9.46	0.01	9.42	0.07	9.46	0.06	9.58	0.02	9.62	0.02
J0148+0003	6662	1461	4543	184	6475	340	5411	68	3845	258	2278	233	3458	115	4510	185	9.42	0.22	9.67	0.04	9.72	0.06	9.62	0.01	9.62	0.01
J0934+0005	6536	282	2807	58	2880	145	2694	163	2702	10	1635	236	2573	255	2995	597	9.25	0.04	8.98	0.02	8.73	0.05	8.73	0.06	8.71	0.06
J0019-1053	5220	90	4426	77	5709	376	5909	506	3484	195	2818	115	2850	480	4694	467	8.9	0.02	9.28	0.02	9.15	0.07	9.27	0.09	9.3	0.08
J0850+0022	6116	272	2415	124	3503	960	3763	419	2905	124	1750	438	4856	322	3436	136	8.98	0.04	8.73	0.05	8.8	0.29	8.93	0.11	8.84	0.11
J0404-0446	4341	304	1966	51	2788	1364	2732	140	1841	100	1667	264	868	230	6567	769	8.74	0.06	8.54	0.03	8.66	0.6	8.64	0.06	8.43	0.08
J1052+0236	9628	852	5412	422	10110	1132	8118	339	5192	273	2702	340	5727	568	4513	409	9.37	0.08	9.41	0.08	9.66	0.11	9.54	0.05	9.55	0.05
J0223-0007	5240	175	3078	81	3416	549	5009	271	3500	374	2426	288	5199	404	5461	1392	8.88	0.03	8.9	0.03	8.65	0.19	9.05	0.08	9.12	0.07
J0240-0758	5859	136	2828	94	3542	445	4190	159	3014	33	2185	133	5569	276	4137	445	9.0	0.02	8.88	0.03	8.75	0.13	8.95	0.04	9.03	0.04
J0136-0015	7052	115	3554	87	2731	1000	3468	276	4490	435	2249	192	3648	195	5069	586	9.1	0.02	9.01	0.03	8.43	0.42	8.68	0.08	8.76	0.08
J0213-1003	5093	167	2742	251	3393	279	4054	193	3523	932	1939	288	4174	871	4579	118	9.06	0.03	8.96	0.09	8.85	0.08	9.06	0.05	9.05	0.05
J0341-0037	5247	131	2571	106	3219	2612	3406	611	3982	399	1901	277	3567	737	4448	908	8.8	0.02	8.68	0.04	8.58	1.47	8.68	0.19	8.74	0.19
J0143-0056	3890	77	2857	107	5510	1372	3894.	571	3277	107	1400	212	1877	121	4418	1204	8.54	0.02	8.75	0.04	8.97	0.26	8.72	0.16	8.78	0.16
J0927+0004	8308	153	5664	203	7419	916	6256	149	4556	292	2478	190	4266	356	4497	558	9.21	0.02	9.34	0.04	9.23	0.13	9.18	0.03	9.23	0.03
J0213-0036	4064	102	3463	155	5697	1019	4459	172	2720	42	1812	159	2680	569	4998	672	8.53	0.02	8.88	0.05	8.98	0.19	8.85	0.04	8.97	0.04
J1050+0207	7608	817	4889	763	5205	1494	5402	504	4416	211	2410	197	2442	346	5261	707	9.06	0.1	9.15	0.16	8.88	0.33	8.9	0.1	9.01	0.1
J0948+0137	5116	252	3364	331	3766	729	3881	392	3293	179	1997	368	3373	769	2879	1026	8.6	0.05	8.75	0.1	8.54	0.21	8.67	0.13	8.77	0.11
J0042+0008	5362	348	2944	121	4020	346	3608	160	4970	293	1844	224	4028	473	5323	540	8.64	0.06	8.58	0.04	8.5	0.11	8.44	0.06	8.54	0.06
J1013+0245	8990	304	4603	709	8396	1031	7716	873	5124	469	2679	214	6547	3017	3038	291	9.07	0.04	8.95	0.16	9.27	0.14	9.25	0.12	9.15	0.14
J1021-0027	4913	629	3260	159	9085	1676	8818	719	2790	343	2410	158	5061	526	4593	184	8.29	0.13	8.52	0.05	9.15	0.21	9.29	0.09	9.43	0.08
J0038-0019	4333	333	2657	190	3558	284	3304	118	3398	353	2037	227	5495	664	2146	273	8.26	0.08	8.35	0.07	8.33	0.1	8.39	0.04	8.34	0.04
J0912-0040	4885	332	3860	252	5804	3022	4746	227	3199	193	2002	196	2165	214	2015	582	8.37	0.07	8.65	0.07	8.71	0.73	8.66	0.07	8.65	0.07
J1048-0019	4756	650	2901	155	2279	350	2967	1313	3168	288	2261	203	967	372	1261	249	8.34	0.14	8.37	0.06	7.81	0.2	7.99	0.136	8.11	0.71
J1045-0047	6028	520	2833	308	9707	3147	4724	4041	3842	184	2203	228	6403	1426	2820	152	8.44	0.1	8.29	0.11	8.9	0.38	8.46	0.11	8.6	0.1
J0042-0011	4198	217	1829	210	1578	123	1490	95	2929	161	1098	599	1701	475	1177	165	8.1	0.06	7.9	0.11	7.52	0.12	7.49	0.09	7.42	0.08
J1046+0025	3971	481	3210	164	4320	1113	3383	585	2916	146	2207	227	1014	985	1004	196	8.11	0.12	8.35	0.06	8.26	0.33	8.16	0.24	7.81	0.24
J0930-0018	6704	857	5059	417	7035	797	6080	7367	4590	423	3059	416	842	247	1509	1415	8.47	0.13	8.72	0.09	8.65	0.496	8.48	0.106	8.59	0.134
J1108+0141	7469	410	2601	92	4093	592	4751	64	3351	125	2831	1189	3948	434	4185	134	9.59	0.05	9.24	0.04	9.37	0.14	9.52	0.01	9.42	0.02
J1005+0245	6095	1551	2476	144	3879	3285	5052	199	4574	822	1745	154	4291	196	4054	189	9.07	0.26	8.94	0.06	9.11	1.64	9.45	0.04	9.44	0.04

[a] $M_{\mathrm{BH}}(\mathrm{H}\alpha)$ measurements obtained through FWHM(Hα) and L_{6200}.
[b] $M_{\mathrm{BH}}(\mathrm{H}\alpha)$ measurements obtained through FWHM(Hα) and $L(\mathrm{H}\alpha)$.

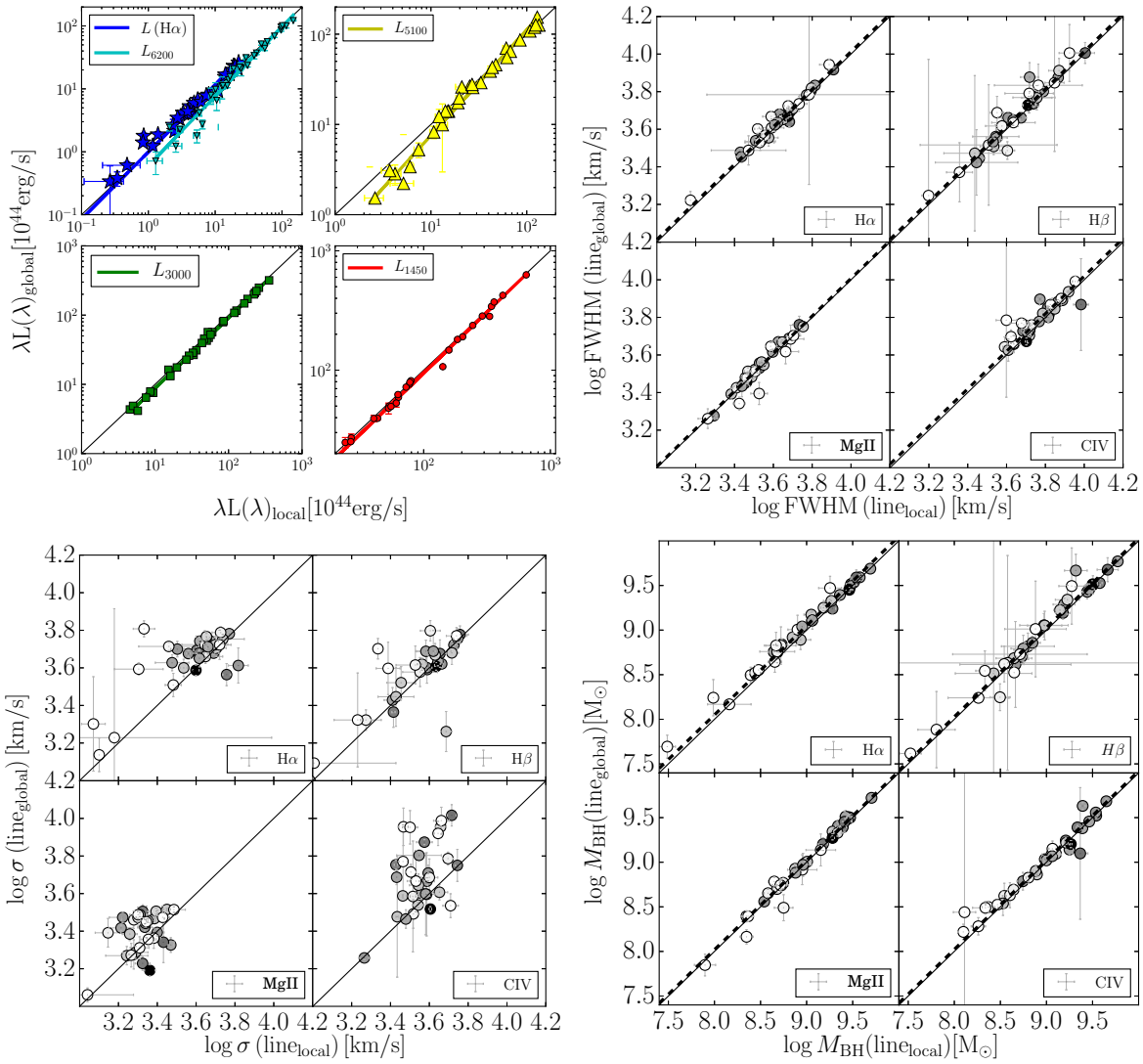

Figure 2.2.5: Comparison of various line and continuum properties measured under the two general assumptions of *local* (horizontal axis) and *global* (vertical axis) SEDs. Top-Left panel: L (Hα)(blue stars), L_{6200}(cyan triangles), L_{5100} (yellow triangles), L_{3000} (green squares) and L_{1450} (red dots). The colored solid lines are the best linear fits to the corresponding data. Top-Right panel: FWHM(Hα) (top-left), FWHM(Hβ) (top-right), FWHM(Mg II) (bottom-left) and FWHM(C IV) (bottom-right) lines measurements. Bottom-left panel: Same as Top-Right panel but comparing $\sigma_{\rm line}$s instead of FWHMs (note the much larger scatter in this case). Bottom-right panel: $M_{\rm BH}$ comparison between *local* and *global* approaches. In the top-right and bottom-right panels black dashed lines represents the median offset between *global* and *local* measurements. In all panels the black solid diagonal line represents the 1:1 relation. Points have been color-coded in gray scale by S/N where darker colors correspond to larger S/N.

2.4.1.1 Continuum biases

In figure 2.2.5 we present the comparison between $L_{\rm local}$ and $L_{\rm global}$ (top-left panel) for different chosen wavelengths. We generally find small but systematic offsets between quantities derived via the *local* versus *global* approach. We find that the L_{1450}, L_{3000}, L_{5100} and L_{6200} median offsets ($\Delta L \equiv \log(L_{\rm global}/L_{\rm local})$) are typically small ($\lesssim |-0.05|$ dex, see Table 2.4 for details). These offset are consistent with a very subtle overestimation of the continuum emission when the *local* approach is adopted (see Fig. 2.2.4 for a particular example).

2.4.1.2 Line width biases

The *systematic continuum overestimation* that we found coming from adopting the *local* instead of the *global* approach will naturally lead to *systematical* FWHM *underestimation* as can be also seen in Figure 2.2.5 (top-right panel). Indeed, all the relevant line width measurements present small median offsets (ΔFWHM $\equiv \log$ FWHM$_{\rm global}$/FWHM$_{\rm local}$) smaller than $\lesssim 0.02$ dex as can be seen in Table. 2.4. As mentioned in §2.2 the measurements of FWHM(Hβ) are more challenging for low S/N and/or objects where most iron emission is suppressed by telluric absorption. This explains the outliers and large uncertainties for some objects in the FWHM(Hβ)$_{\rm local}$-FWHM(Hβ)$_{\rm global}$ plot. Except for these few outliers, the FWHM$_{\rm local}$ measurements of all the emission lines are proportional to, and systematically but slightly smaller than the FWHM$_{\rm global}$ measurements.

When we perform the same analysis on the velocity dispersion $\sigma_{\rm line}$ (see the bottom-left panel in Fig. 2.2.5) we find a large scatter (~ 0.14 dex) and usually weak, if any, correlations ($P > 0.01$) between the *local* and *global* measurements in Hα, Mg II and C IV. On the other hand, the Hβ line shows a much tighter correlation ($r_{\rm s} < 0.78$, $P = 2 \times 10^{-9}$) but the scatter is still very large (~ 0.12 dex). These results indicate a strong and perhaps non-linear dependency between the measured $\sigma_{\rm line}$ and the level of its local continuum. As a result $\sigma_{\rm line}$-based determinations of $M_{\rm BH}$ may be unreliable for data of limited spectral coverage. In particular, such estimates may suffer from higher systematic uncertainties compared to those based on FWHM.

2.4.1.3 Black hole mass biases

In §§2.4.4 we will describe in detail the methods that we follow for $M_{\rm BH}$ calibration using the *local* and *global* approaches. The form of the virial mass estimator (see Eqn. 2.2.1) indicates that biases in $M_{\rm BH}$ determinations are mainly driven by the (small) line width biases. This is not the case for the continuum luminosity since one can, in principle, re-calibrate the $R_{\rm BLR} - L$ relations to use either one of the *local* or *global* measured continuum luminosities, thus completely eliminating the systematic

Table 2.4: *Median induced offsets when the local approach is used instead of the global approach.*

Line	$\Delta M_{\rm BH}$ (dex)	ΔFWHM (dex)	ΔL^1 (dex)	$\Delta L_{\rm line}$ (dex)
Hα	$0.03^{+0.06}_{-0.06}$	$0.015^{+0.020}_{-0.015}$	$0.05^{+0.04}_{-0.06}$	$0.05^{+0.04}_{-0.06}$
Hβ	$0.04^{+0.09}_{-0.05}$	$0.020^{+0.035}_{-0.025}$	$-0.01^{+0.03}_{-0.05}$	$0.03^{+0.12}_{-0.05}$
Mg II	$0.01^{+0.03}_{-0.02}$	$0.010^{+0.015}_{-0.010}$	$-0.03^{+0.03}_{-0.02}$	$0.03^{+0.03}_{-0.03}$
C IV	$0.05^{+0.06}_{-0.03}$	$0.020^{+0.025}_{-0.020}$	$-0.02^{+0.02}_{-0.03}$	$0.07^{+0.06}_{-0.07}$

biases.

After following the procedure described in §§2.4.4 and the strict virial assumption ($M_{\rm BH} \propto {\rm FWHM}^2$) we found that the $M_{\rm BH}$ offsets ($\Delta M_{\rm BH} = \log M_{\rm BH,\ global}/M_{\rm BH,\ local}$) are in very good agreement with our predictions, as can be seen in the bottom-right panel of Figure 2.2.5 and are smaller than $\lesssim$0.04 dex (see Table 2.4). From the values listed in Table 2.4 and from a visual inspection of Fig. 2.2.5 one can conclude that Hα, Mg II, and C IV are consistent (within the scatter) with $\Delta M_{\rm BH}$ being independent of $M_{\rm BH}$. Hβ is again a bit more complicated, due to the difficulties we mentioned above. However, after removing the low-quality outliers we eventually find Hβ to be consistent with $\Delta M_{\rm BH}$ being independent of $M_{\rm BH}$. Among all the lines considered here, we find Mg II to be the one showing the smallest biases when following the *local* approach . This is somewhat surprising, given the several important spectral features (BC, FeII lines) that are influencing this spectral region.

2.4.1.4 Line luminosity biases

Line luminosities are more sensitive to continuum placement than the other quantities we examined. Indeed, we found line luminosity median offsets ($\Delta L_{\rm line} = \log L\,({\rm line})_{\rm global}\,/L\,({\rm line})_{\rm local}$) of $0.06^{+0.08}_{-0.08}$ dex , $0.03^{+0.06}_{-0.04}$ dex, $0.02^{+0.09}_{-0.08}$ dex and $0.05^{+0.04}_{-0.06}$ dex for C IV, Mg II, Hβ and Hα, respectively. Furthermore, we find that the large scatter that is generally found in $\Delta L_{\rm C\,IV}$, $\Delta L_{\rm Mg\,II}$, $\Delta L_{\rm H\beta}$ and $\Delta L_{\rm H\alpha}$ is due to the fact that these quantities are anti-correlated with continuum luminosity. In particular, the relations between these line luminosity biases and L_{5100} show $r_{\rm s}$ correlation coefficients of -0.38, -0.44, -0.65 for C IV, Mg II, Hβ and Hα, respectively. This implies that using the local approach to estimate line luminosities generally leads to an underestimation of the latter, and its effect is larger for low luminosity objects (up to 0.14 dex, or 38%, in the case of C IV).

In summary, the impact of using the *local* approach to estimate the local luminosities, lines widths and black hole masses when the *global* continuum is unknown

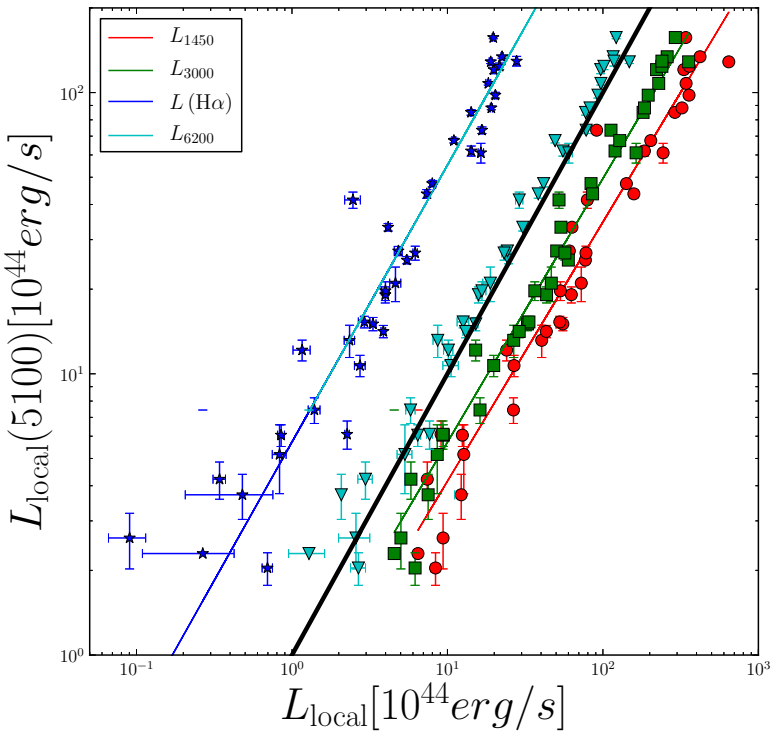

Figure 2.2.6: *local* Hα line luminosity (blue), L_{6200} (cyan) L_{3000} (green) and L_{1450} (red) vs $L_{5100}^{\rm local}$. The color solid lines represent the best linear fits to the corresponding data. Black solid line represents the 1:1 relation.

is found to be small (< 0.06 dex). However, the impact using the *local* approach to estimate *line luminosities* is found be luminosity dependent, being stronger for low luminosity objects. The median values of ΔFWHM, ΔL, $\Delta M_{\rm BH}$, and $\Delta L_{\rm line}$ that we found are summarized in Table 2.4. Based on the general good agreement between *local* and *global* measurements and in order to provide the community with strategies more applicable to observations with limited wavelength coverage, in *the analysis that follows is based only on the local measurements*, unless otherwise stated.

2.4.2 Luminosity Correlations

Figure 2.2.6 presents a comparison between L_{5100} and the luminosity indicators most commonly used in the context of $M_{\rm BH}$ estimates. The best-fit parameters of all the correlations can be found in Table 2.5. These relations provide us with the links necessary to connect each luminosity indicator and $R_{\rm BLR}$ (Hβ), through the $R_{\rm BLR}-L_{5100}$ relation obtained from reverberation mapping experiments (Kaspi et al., 2000, 2005; Bentz et al., 2009, 2013). For the purposes of the present work, we use the same calibration as in TN12, which is appropriate for sources with $L_{5100} \gtrsim 10^{44}\,{\rm erg\,s^{-1}}$:

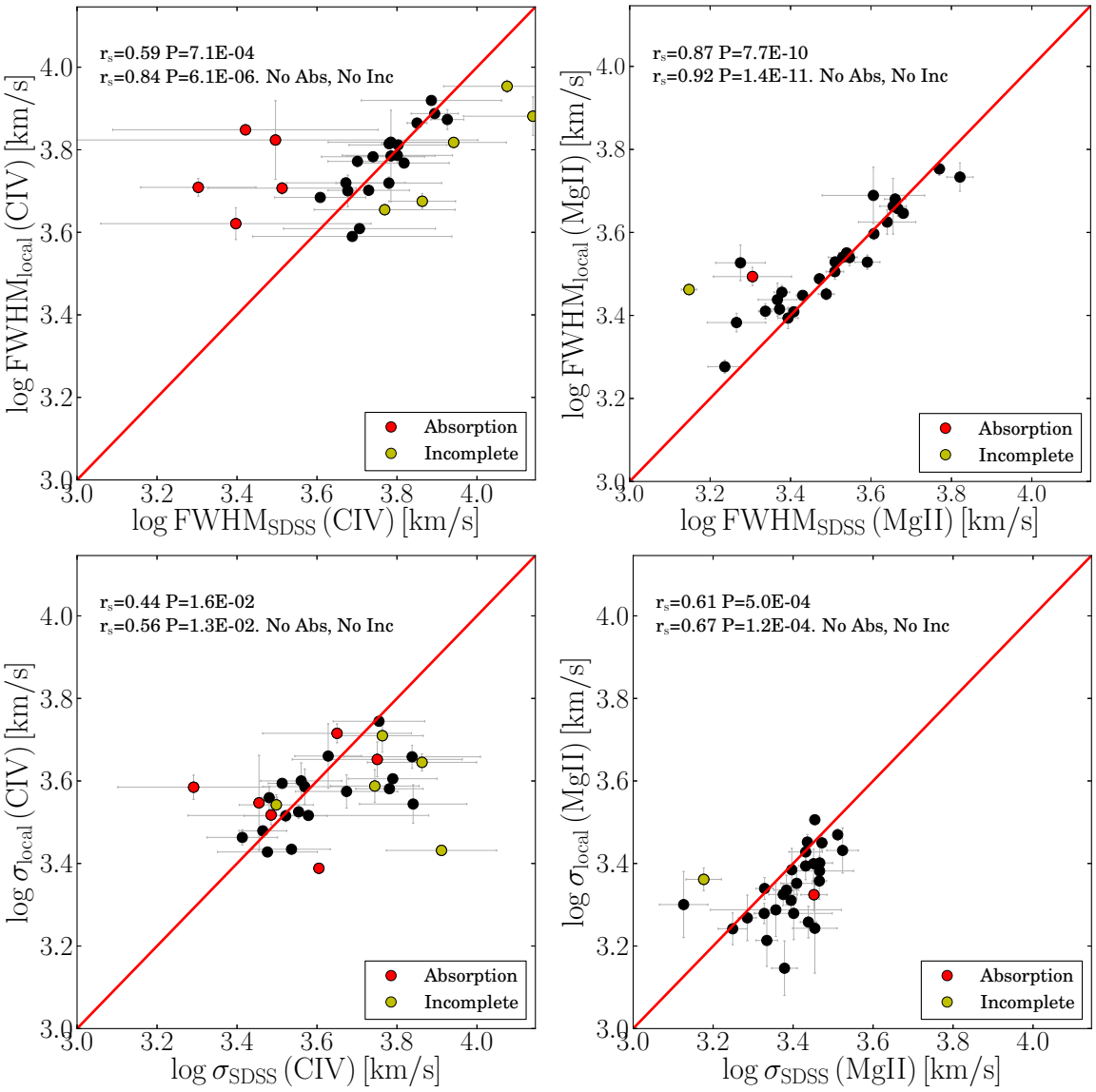

Figure 2.2.7: FWHMs (top-panels) and $\sigma_{\rm line}$s (bottom-panels) of the C IV (left) and Mg II (center) profiles found with low quality SDSS data versus those measured in our high quality X-Shooter using the *local* continuum approach. The right panels shows C IV vs Mg II line widths measured with SDSS data. Red solid line shows the 1:1 relation and red dashed line represents FWHM (C IV) $= \sqrt{3.7}$ FWHM (Mg II). Red dots represent objects with noticeable absorption features while yellow dots are objects with SDSS incomplete profiles. It can be seen that C IV profiles with strong absorption features artificially populate the zone where FWHM (C IV) $<$ FWHM (Mg II).

Table 2.5: *Best fit power law parameters to the following relations:* [a] $L_{5100}^{local} = AL_{local}^{\gamma}$, [b] $L_{5100}^{local} = AL_{global}^{\gamma}$, [c] $L_{global} = AL_{local}^{\gamma}$.

	$L_{5100}^{\rm local}$ vs $L_{\rm local}$ [a]		$L_{5100}^{\rm local}$ vs $L_{\rm global}$ [b]		$L_{\rm global}$ vs $L_{\rm local}$ [c]	
	γ	A	γ	A	γ	A
L(Hα)	1.04	4.73	1.09	3.59	0.94	1.32
L_{6200}	0.98	1.23	0.94	1.57	0.96	1.28
L_{5100}	1	1	0.89	1.61	1.15	0.60
L_{3000}	0.92	0.67	0.91	0.77	1.01	0.88
L_{1450}	0.88	0.56	0.87	0.64	1.02	0.87

$$R_{\rm BLR}\left({\rm H}\beta\right) = 538\left(\frac{L_{5100}}{10^{46}\,{\rm erg\,s^{-1}}}\right)^{0.65}\ {\rm lt\text{-}days} \tag{2.2.3}$$

As shown in Fig. 2.2.6 the $L\left({\rm H}\alpha\right)$-$L_{5100}$ relation shows a larger scatter than those involving UV continuum luminosities (L_{1450}-L_{5100} and L_{3000}-L_{5100}). This may therefore contribute to an increased uncertainty in $L\left({\rm H}\alpha\right)$-based determinations of $M_{\rm BH}$. This is not surprising, given the expected range of conditions in the BLR. Consequently, we also investigate use of L_{6200} as an alternative to $L\left({\rm H}\alpha\right)$. As can be seen in Fig. 2.2.6 (cyan inverted triangles) the L_{6200}-L_{5100} relation shows an even smaller scatter than L_{1450} and L_{3000}. This is particularly the case for objects with $L_{5100} \gtrsim 10^{45}\,{\rm erg\,s^{-1}}$, where host galaxy contribution is negligible.

L_{1450}-L_{5100} and L_{3000}-L_{5100} luminosity correlations are supra-linear, in the sense of showing $L \propto L_{5100}^{\beta}$ and $\beta > 1$ (see first column of Table 2.5 and note that $\beta = \gamma^{-1}$). This has been noted earlier by Vanden Berk et al. (2004) but is in contrast to Shen & Liu (2012) who found consistency with $\beta = 1$ in the sample of high luminosity quasars ($L_{5100}\,[{\rm erg\,s^{-1}}] > 10^{45.4}$).

While there are various correlations with $M_{\rm BH}\left({\rm H}\alpha\right)$ and $L/L_{\rm Edd}$ (measured from Hα) that can, perhaps, explain these differences, it is important to note that our sample is by no means complete. It was chosen to sample the high-L z=1.55 AGN population by giving equal weight to a group of sources with the same $M_{\rm BH}$ and $L/L_{\rm Edd}$ (see paper I). Hence, the relationship found here should be checked in a larger and complete sample that represents the entire AGN population.

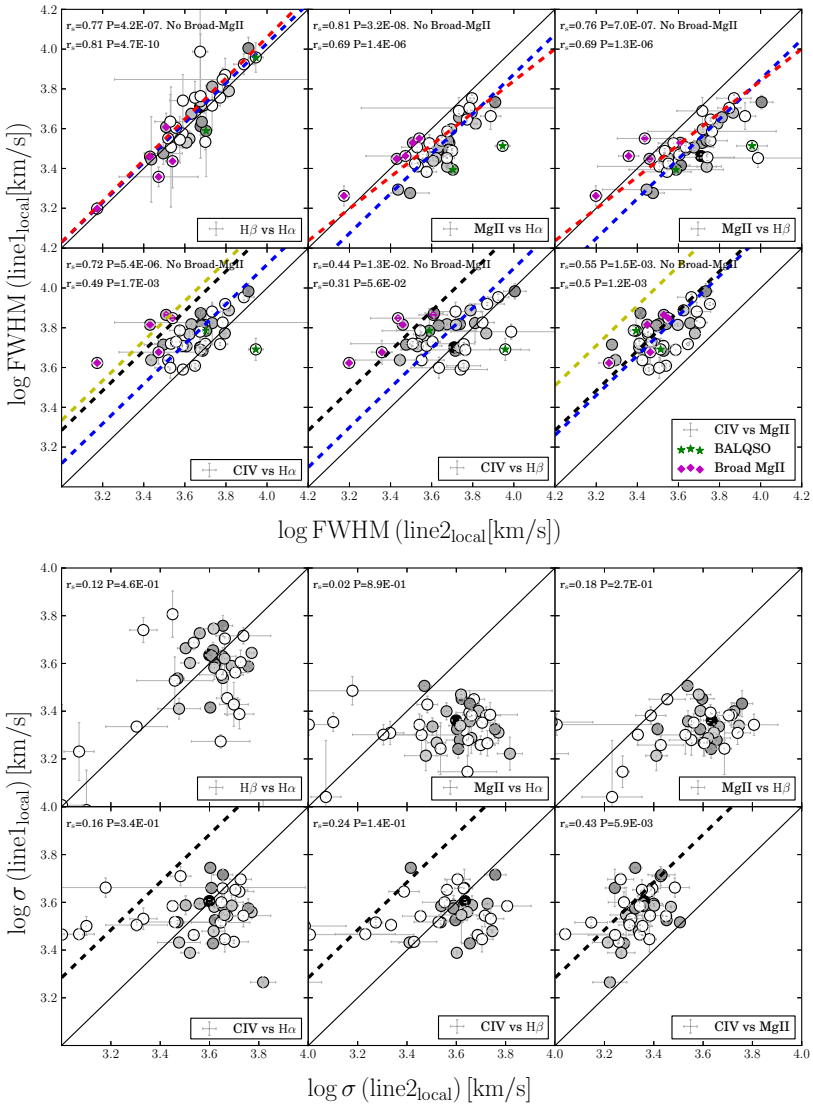

Figure 2.2.8: FWHM (top) and σ (bottom) comparisons between different lines in the **local** continuum approach as indicated in the inserts of each panel (line1 vs line2). The black solid lines represents the 1:1 relation. The black dashed line represents FWHM (C IV) $= \sqrt{3.7}$FWHM (line). The yellow dashed line represents FWHM (C IV) $= \sqrt{3.7}$FWHM (Hβ) after rescaling the FWHM of each line to FWHM(Hβ) using the median value of FWHM (Hβ) /FWHM (*line*). Red dashed lines represent previous scaling relations (FWHM(Hβ) vs FWHM(Mg II) from TN12, and FWHM(Hβ) vs FWHM(Hα) from Greene & Ho (2005)). Blue dashed lines represent the best fit after assuming FWHM(Hβ)$\propto$FWHM(Hα)$\propto$FWHM(Mg II)$\propto$FWHM(C IV). Points are color-coded in gray scale by the S/N of the continuum bands around Hβ where darker colors translates into larger S/N. Broad absorption lines quasars (BALQSO, green stars) and the broad-Mg II objects (magenta diamonds, see §2.4.3.4) are the main sources of discrepancies of the C IV and Mg II FWHMs when compared to the Hα and Hβ FWHMs.

2.4.3 Line widths and line offsets

2.4.3.1 Comparison with SDSS data

At the redshift range of our sample, the archival SDSS spectroscopy covers both the C IV and Mg II lines in 29 out of 39 objects.[2] In Figure. A.A.1 we show an example of the SDSS and X-Shooter spectra in the overlapping region. Comparing SDSS and X-shooter data allow us to test the effects of having only survey-grade data, with limited S/N and spectral resolution, on the measurement of line widths. To this end, we used our C IV and Mg II fitting code for the lower quality archival SDSS DR7 spectra. In Fig. 2.2.7 we compare the FWHM (top-panels) and $\sigma_{\rm line}$ (bottom-panels) values of the C IV and Mg II lines obtained from the SDSS data, with those obtained from our higher quality spectra under the *local* approach. We also show the Spearman correlation coefficients and corresponding P-values in each panel.

We find that SDSS-based FWHM(C IV) for objects with absorption features which are unresolved in the SDSS data (4 out of 29 objects, red symbols), or those with partially-observed profiles because of the limited SDSS wavelength coverage (5 out of 29, yellow symbols) result in FWHM measurements which are systematically different from those obtained from the higher quality data. Specifically, while *unresolved absorption* features are likely to result in a systematic *underestimation* of FWHM(C IV), by about $50 \pm 10\%$, *incomplete* profiles are likely to lead to a systematic *overestimation* of FWHM(C IV), by about $40 \pm 20\%$. This result was found in previous works (e.g. Denney et al., 2013; Park et al., 2013; Tilton & Shull, 2013) and could explain, to some extent, the over-population of narrow C IV objects that is reported in TN12. The Mg II line does not generally show strong absorption features. Indeed, we find that the SDSS-based FWHM(Mg II) measurements are generally consistent with our higher quality FWHM(Mg II) measurements with the exception of five objects. Of these 5 objects, three have very low S/N, one has an incomplete profile, and one shows signs of absorption.

Looking into the corresponding comparison with $\sigma_{\rm line}$ (bottom panels of Fig. 2.2.7), we generally find that sources with absorption features or incomplete profiles do not stand out from the "normal" population. The entire sample shows considerable scatter when comparing the SDSS and X-Shooter line measurements and show less signifcant correlations than the FWHM(top panels of Fig. 2.2.7). For σ (Mg II), we find the SDSS measurements to be systematically broader than our $\sigma_{\rm X\text{-}Shooter}$ (Mg II) estimations, and the scatter is larger than the one in the FWHM comparison. For σ (C IV), there is a large dispersion (0.2 dex) between SDSS and X-Shooter measurements, that could be caused by the high sensitivity of $\sigma_{\rm line}$ measurements to continuum placement.

We conclude that the usage of $\sigma_{\rm line}$ to measure line width in data of limited quality introduces significant scatter. For such data, the use of FWHM is preferred, especially

[2]For the remaining 10 objects, the only archival spectroscopy available is from the 2SLAQ survey, which is of limited S/N and is not flux calibrated.

Table 2.6: *Line width ratios and correlations. For each pair of lines, we list median values and scatter of* $\mathrm{Q} \equiv \log\left(FWHM\left(line1\right)/FWHM\left(line2\right)\right)$ *and the Spearman correlation coefficients betweenFWHM*(*line1*) *and FWHM*(*line2*)*. We tabulate these quantities for both the complete sample (under the local approach), and after excluding the five broad-Mg* II *and the two BALQSO.*

	-Hα-						-Mg II-						-C IV-					
	-All objects [a]-			-No Broad-Mg II[b]-			-All Objects [a]-			-No Broad-Mg II[b]-			-All Objects [a]-			-No Broad-Mg II [b]-		
line1	Q	scatter	r_s	Q	scatter	r_s	Q	scatter	r_s	Q	scatter	r_s	Q	scatter	r_s	Q	scatter	r_s
Hα	...	...	...	...	...	...	0.13	0.08	0.69	0.13	0.07	0.81	-0.12	0.14	0.48	-0.11	0.10	0.72
Mg II	-0.13	0.08	0.69	-0.13	0.07	0.81	...	...	...	...	...	...	-0.26	0.10	0.50	-0.25	0.10	0.55
Hβ	0.03	0.07	0.81	0.04	0.07	0.77	0.15	0.10	0.69	0.16	0.08	0.88	-0.10	0.17	0.31	-0.09	0.13	0.44

for the Mg II line. In addition, the absorption features often seen in the C IV line necessitate the use of high-quality spectra, in order to resolve and properly account for these features, even if one uses FWHM instead of $\sigma_{\rm line}$.

2.4.3.2 Line Offsets

We measured the line offsets with respect to the laboratory wavelengths of Hα, Hβ and Mg II. Their absolute values ($|\Delta v|$) are found to be (within the 16% and 84% percentiles) smaller than $600\,\mathrm{km\,s^{-1}}$, $550\,\mathrm{km\,s^{-1}}$ and $250\,\mathrm{km\,s^{-1}}$ respectively.

Many of the observed C IV lines show large negative velocity offsets ($\Delta v \simeq -1200 \pm 1000\ \mathrm{km\,s^{-1}}$) suggesting non virial equilibrium of the C IV emitting clouds. This has been noted in numerous earlier publications, (e.g. Shang et al., 2007; Wang et al., 2009; Shen & Liu, 2012; Trakhtenbrot & Netzer, 2012; Runnoe et al., 2013; Brotherton et al., 2015a). Moreover, the C IV velocity offsets are anti-correlated with $L/L_{\rm Edd}$ ($r_{\rm s} = -0.53$, $P = 0.0004$), i.e., higher $L/L_{\rm Edd}$ will translate into bluer line centers (e.g. Marziani et al., 2006; Sulentic et al., 2007). We also find that the much smaller velocity offsets of the Mg II lines are also anti-correlated with $L/L_{\rm Edd}$ ($r_{\rm s} = -0.49$, $P = 0.001$) which is also in agreement with Marziani et al. (2013b). We repeated the analysis using the normalized accretion rate ($\dot{m} \equiv L_{\rm model}/L_{\rm Edd}\left[M_{\rm BH}^{\rm model}\right]$) taken from the best-fit AD models (to be presented in paper III; see paper I for details). We find that our measured $\dot{m}$, too, is anti-correlated with C IV velocity offsets ($r_{\rm s} = -0.49$, $P = 0.001$), however the analogous correlation with Mg II velocity offsets becomes insignificant ($P = 0.07$). These results suggest that $L/L_{\rm Edd}$ is playing an important role in the line offsets of the C IV profile, while Mg II velocity offsets may involve additional parameters. As explained earlier, the way we selected our sample makes it difficult to make strong statements regarding the entire population of AGN. When the same analysis is done with the Balmer lines, we find no correlation between neither $L/L_{\rm Edd}$ nor $\dot{m}$ and the Balmer line velocity offsets ($P = 0.26$ and $P = 0.90$, for Hα and Hβ, respectively). We further confirm earlier results (e.g., Corbin, 1990; Richards et al., 2011) of a significant anti-correlation between the C IV blueshifts and the C IV line strength, EW(C IV) ($r_{\rm s} = 0.43$, $P = 0.006$), but not with EW(Mg II) ($r_{\rm s} = 0.25$,$P = 0.12$).

Several studies investigated the possibility that broad emission lines are gravitationally red-shifted by few hundred to few thousand $\mathrm{km\,s^{-1}}$ (e.g. Netzer, 1977; Zheng & Sulentic, 1990; Popovic et al., 1995; Müller & Wold, 2006; Tremaine et al., 2014). This effect is enhanced in very broad emission line components (FWHM $\gtrsim 7000\,\mathrm{km\,s^{-1}}$) that are formed close to the BH. In this work we made no attempt to include this in the modelling of the line profiles since we are mainly after the line FWHM which is insensitive to such small variations. We verified, however, that line offset due to this effect are smaller than the general uncertainty and scatter associated with our measurements of the line center velocity.

2.4.3.3 Line width correlations

Figure 2.2.8 presents a comparison between the widths of some of the broad emission lines in our X-shooter observations, in terms of FWHM (top panel) and line dispersion ($\sigma_{\rm line}$; bottom panel). For reference, we also illustrate the 1:1 relation (black solid line), and a constant scaling of FWHM (C IV) $= \sqrt{3.7}$ FWHM (Hα, Hβ, Mg II) (black dashed line). The latter scaling is motivated by the typical ratio of the corresponding BLR sizes for Hβ and C IV, as measured in RM experiments, and under the virialized BLR assumption (see detailed discussion in TN12). We have plotted in yellow a dashed line that represents FWHM (C IV) $= \sqrt{3.7}\left\langle \frac{\mathrm{FWHM(H}\beta)}{\mathrm{FWHM(H}\alpha,\mathrm{Mg\,II})} \right\rangle$ FWHM (Hα, Mg II) to account for the median FWHM ratio between FWHM(Hβ) and the FWHM of Hα and Mg II. Finally, we have color coded the points in gray scale by the S/N of the continuum bands around Hβ where darker colors translates into higher S/N. In Figures A.A.3 and A.A.4 of the Appendix A.4 we show the normalized Hα, Hβ, Mg II and C IV observed line profiles in velocity space to provide the reader with a direct visual comparison of the most prominent emission lines. The large error bars in the Hβ line widths are due to the low signal to noise and the difficulty of constraining the iron emission around Hβ, because of the telluric absorption (see §2.2).

We generally find very good agreement between the FWHMs of Hβ and Hα (Fig. 2.2.8 top-left panel). On average, FWHM(Hβ) is broader than FWHM(Hα) by 0.03 dex (see blue dashed line in Fig. 2.2.8), with a scatter of about 0.08 dex. This result is in good agreement with several previous studies, as well as with the scaling relation reported in Greene & Ho (2005) (see red dashed line in Fig. 2.2.8).

We also find that objects with $\log \mathrm{FWHM\,(H}\beta)\left[\mathrm{km\,s^{-1}}\right] \leq 3.6$ ($\sim 4000\,\mathrm{km\,s^{-1}}$) show FWHM(H$\beta$) slightly narrower than the median trend (i.e. below the blue dashed line in Fig. 2.2.8) by about 0.04 dex (10%). These objects are however fainter and their values are less accurate because of the difficulties with Hβ measurements. This results is in agreement with Denney et al. (2009a) where they found that the estimated FWHM(Hβ) in low quality data ($S/N \lesssim 20$) is not reliable.

From Fig. 2.2.8 we can also see that there are significant correlations between the FWHMs of: 1) Hα and Mg II (scatter of $\sigma_\Delta = 0.08$ dex), 2) Hβ and Mg II ($\sigma_\Delta =$

0.10 dex) and 3) Hα and Hβ (σ_Δ = 0.07 dex) in agreement with several previous works (e.g. Greene & Ho, 2005; Shang et al., 2007; Wang et al., 2009; Shen & Liu, 2012; Trakhtenbrot & Netzer, 2012; Marziani et al., 2013a). Also, FWHM(Mg II) is proportional to and narrower than FWHM(Hβ) by 0.16 dex (30%), with a scatter of about 0.08 dex and no dependence on FWHM(Hβ). There are however some outliers in these general trends: The two BALQSOs (green dots in Fig. 2.2.8) and 5 objects that show FWHM (Mg II) $\gtrsim$ FWHM (Hβ) and have high $L/L_{\rm Edd}$ ($>$ 0.17, hereafter broad-Mg IIobjects, magenta diamonds in Fig. 2.2.8). These 7 objects and their implications in the FWHM(Mg II)-Balmer lines correlations are further discussed in §2.4.3.4.

From the discussion above it is reasonable to assume that the emissivity weighted Mg II region is more distant from the central BH than the corresponding regions for the Hα and Hβ lines. On the other hand, both Balmer lines seem to come from the same part of the BLR. As a consequence and based on the FWHM linear correlation among Hα,Hβ and Mg II, assuming virialization of Hβ would reasonably imply virialization of Mg II and Hα.

The correlations of FWHM(C IV) with the measured FWHM of the other lines are weaker, occasionally insignificant (i.e. P>0.01) and non-linear: 1) Hα ($r_{\rm s}$ = 0.48, P= 0.02, σ_Δ = 0.14 dex), 2) Hβ (insignificant, P= 0.05) and 3)Mg II ($r_{\rm s}$ = 0.50, P= 0.001, σ_Δ = 0.10 dex). This would mean that FWHM(C IV) is not linearly proportional to the FWHM of Hα, Hβ and Mg II. For example, FWHM (C IV) $\propto$ FWHM (Hα)$^{1.41\pm0.50}$. Moreover, when combining the results of the RM experiments (e.g. Kaspi et al., 2007) with the virial assumption, it is expected that the C IV line would be broader than Hβ, by a factor of about $\sqrt{3.7}$. [3] In contrast, the vast majority of sources in our sample (35/39; 90%) show FWHM (C IV) $<$ $\sqrt{3.7}$ FWHM (Hβ) and one third of the sources have FWHM(Hβ)>FWHM(C IV). These results indicate either a non-virialized C IV emission region, or a very different ionization structure for objects with low and high FWHM(Hβ).

Finally, when we compare the velocity dispersion ($\sigma_{\rm line}$) between the lines of interest (bottom panels of Fig. 2.2.8) we only find one significant correlation between FWHM(Mg II) and FWHM(C IV) ($r_{\rm s}$ = 0.43, P= 0.005) in the *local* approach. However, even this correlation does not hold under the *global* approach (P = 0.36). Due to the fact that the correlations between the FWHM of different lines are much tighter than the $\sigma_{\rm line}$ correlations (under both continuum approaches), and the fact that $\sigma_{\rm line}$ is strongly affected by flux in the line wings, we choose to use the FWHM to estimate $M_{\rm BH}$ in the analysis that follows.

2.4.3.4 Broad-Mg ii and BALQSO objects

As discussed in §2.4.3 we found that Mg II profiles are generally and systematically narrower than Hα and Hβ profiles. However, the top right and top center panels

[3]The scaling factor is somewhat luminosity dependent. See TN12 for a discussion of this issue.

of Fig. 2.2.8 show that around $\log(\mathrm{FWHM}(\mathrm{H}\beta))$ and $\log\left(\mathrm{FWHM}(\mathrm{H}\alpha)\left[\mathrm{km\,s^{-1}}\right]\right) \lesssim 3.6$ ($\leq 4000\mathrm{km\,s^{-1}}$) there are a handful of objects (magenta diamonds) that show $\mathrm{FWHM}(\mathrm{Mg\,II}) \gtrsim \mathrm{FWHM}(\mathrm{H}\alpha, \mathrm{H}\beta)$ and were noted earlier as "broad-Mg II objects".

Marziani et al. (2013b) and Marziani et al. (2013a) presented a thorough Eigen-vector 1 analysis of the Mg II and Hβ profiles following Sulentic et al. (2002) from an SDSS selected sample of 680 quasars. Their classification is based on the location of type-I AGN in the R_{op}-FWHM(Hβ) plane where $R_{\mathrm{op}} = L\left(\mathrm{Fe\,II}\left(4750\text{Å}\right)\right)/L\left(\mathrm{H}\beta\right)$. They claimed that the so called "Broad-Mg II objects" belong to the extreme population A category (A3 and A4 according the their classification, see Fig. 8 in Marziani et al. (2013a)) and represents about 10% of the total population of high luminosity AGN. These extreme population A objects have narrow Hβ profiles ($\leq 4000\,\mathrm{km\,s^{-1}}$) and the highest R_{op} values. They are also among the objects with the highest Eddington ratios and largest velocity offsets. Unfortunately, our difficulties to properly measure the Fe II emission around Hβ do not allow us to measure R_{op} and test their assumptions. can however compare their L/L_{Edd} estimates to our Hα-based L/L_{Edd} estimates by applying a bolometric correction as described in TN12. As can be seen in Figure. 2.2.1 all these objects occupy the top 20 percentile of the L/L_{Edd} distribution in our sample ($L/L_{\mathrm{Edd}} \geq 0.20$) in agreement with Marziani et al. (2013a). The Broad-Mg II objects in our sample also show relatively large C IV and Mg II velocity blue-shifts (top 20%, $\Delta v_{\text{Broad-Mg II}}(\mathrm{C\,IV}) \lesssim -2200\,\mathrm{km\,s^{-1}}$, $\Delta v_{\text{Broad-Mg II}}(\mathrm{Mg\,II}) \lesssim -200\,\mathrm{km\,s^{-1}}$) which is also in agreement with Marziani et al. (2013a). We note however that broad-Mg II objects are not the only ones that meet the mentioned conditions.

As can be seen in Figure 2.2.8, the BALQSOs in our sample show exactly the opposite behavior. They show narrower Mg II profiles than usual. Unfortunately, it is impossible to draw any conclusion based on only two sources.

In Table 2.6 we present the median values and corresponding scatter of the ratio Q$\equiv \log(\mathrm{FWHM(line1)}/\mathrm{FWHM(line2)})$ as well as the Spearman correlation coefficient between the FWHM of the listed lines under two cases: a) including *all* objects in the analysis and b) excluding the broad-Mg II and the BALQSOs from the analysis. It can be seen in Table 2.6 and Fig. 2.2.8 that after removing these outliers the FWHM correlations becomes tighter (i.e. r_{s} increases) and the Q factors remain almost unchanged. We emphasize that this result is also true for FWHM(C IV)while the correlations between FWHM(C IV) and the FWHM of the Balmer lines approach to linearity after removing such 7 objects. Consequently, for the following M_{BH} analysis we exclude both the 5 Broad-Mg II objects and the two BALQSOs.

2.4.4 Black Hole Mass estimators

In this subsection we present the procedure we use to obtain, and compare, different M_{BH} estimates using the different line and continuum measurements. Our starting point, and the basis for all the following correlations, is the sub-sample of 32 AGN

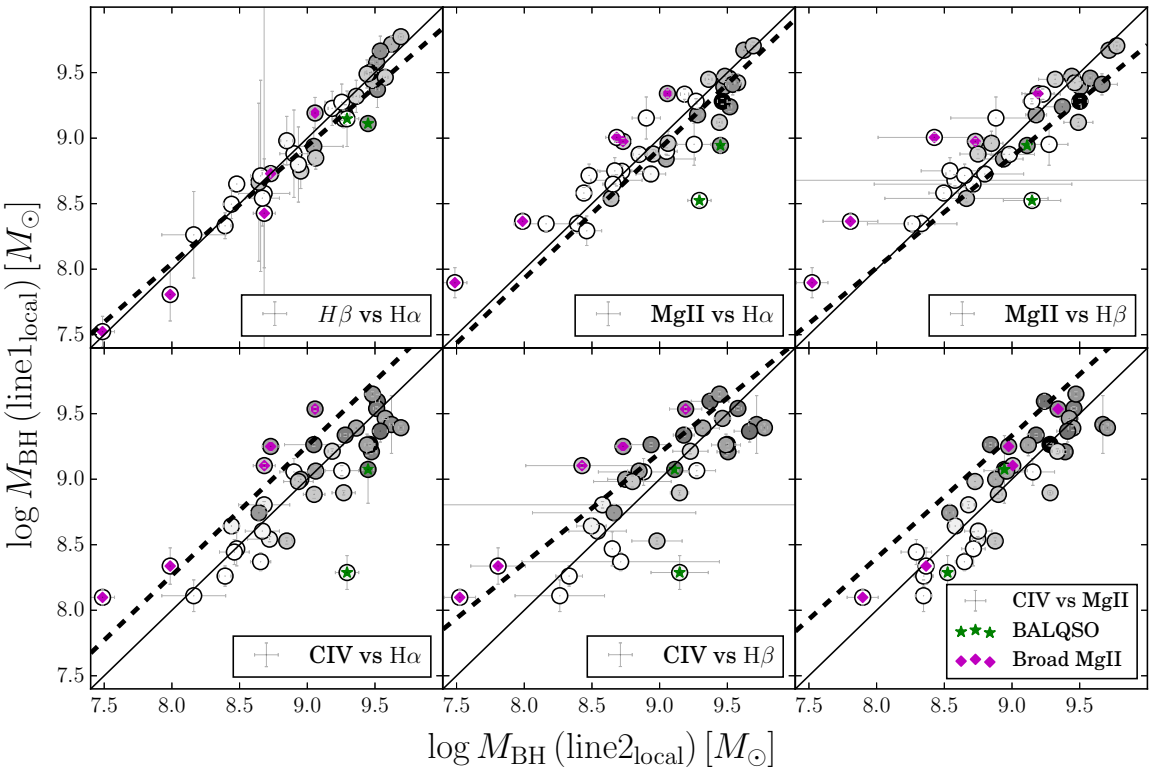

Figure 2.2.9: Comparisons between different $M_{\rm BH}$ estimates that are derived from different lines as indicated in the inserts of each panel. The black solid line represents the 1:1 relation. Hα values were derived using L_{6200}. The dashed black line represents the best fit to previous black hole mass estimators. Points are color-coded in gray scale by the S/N of the continuum bands around Hβ where darker colors translates into larger S/N. BALQSO and the broad-Mg II objects (see §2.4.3.4) are the labelled by green stars and magenta diamonds respectively.

obtained by removing from the original sample 5 sources showing large discrepancy between FWHM(Hβ) and FWHM(Mg II) (see §2.4.3.4) and the two BALQSOs in the sample. A major aim is to find a practical strategy that will allow the identification of sources that are not suitable for accurate mass determination based on single line and continuum measurement.

2.4.4.1 $L_{5100} - R_{\rm BLR}\,({\rm H}\beta)$ relation and Hβ

Most present-day single epoch mass measurements are based on the $R_{\rm BLR}\,({\rm H}\beta)$-$L_{5100}^{\rm local}$ relation, established through RM experiments (see §2.1 and Eq.2.2.3). In this case $L_{5100}^{\rm local}$ is a *local* estimation of the continuum and $R_{\rm BLR}$ is obtained from the time lag of the response of the Hβ line to (optical) continuum variations. This lag is assumed to properly represent the emissivity weighted radius of the broad Hβ line. $M_{\rm BH}$ is obtained from equation 2.2.1 where both ${\rm FWHM}\,({\rm H}\beta)_{local}$ and $L_{5100}^{\rm local}$ are obtained using *local* continuum measurements. These values can be used to obtain the "local" BH mass estimate, $M_{{\rm BH}local}$. We can then use the expressions derived in §2.4.2, and the various biases between the *local* and *global* L_{5100} and FWHM, to derive a *global* expression for $M_{\rm BH}\,({\rm H}\beta)$.

We start by using the local $M_{\rm BH}\,({\rm H}\beta)$ expression obtained by TN12. This expression is most appropriate for our intermediate and high luminosity AGN:

$$M_{\rm BH}\,({\rm H}\beta)_{\rm local} = 5.26\times10^{6}\,M_{\odot}\left(\frac{L_{5100}^{\rm local}}{10^{44}\,{\rm erg\,s^{-1}}}\right)^{0.65}\left(\frac{{\rm FWHM}\,({\rm H}\beta)_{\rm local}}{10^{3}\,{\rm km\,s^{-1}}}\right)^{2}, \quad (2.2.4)$$

Obtaining the equivalent *global* expression is not trivial since we need first to find a relation between $R_{\rm BLR}$ measured from RM and $L_{5100}^{\rm global}$ and not simply use the recipe that connects local measurements. However, we do not know $L_{5100}^{\rm global}$ for the objects targeted by RM campaigns and we have to rely on the scaling relation between $L_{5100}^{\rm local}$ and $L_{5100}^{\rm global}$ that we find in this work (see table 2.5). Substituting in Eq. 2.2.3 we get:

$$M_{\rm BH}\,({\rm H}\beta)_{\rm global} = 7.17\times10^{6}\,M_{\odot}\left(\frac{L_{5100}^{\rm global}}{10^{44}\,{\rm erg\,s^{-1}}}\right)^{0.58}\left(\frac{{\rm FWHM}\,({\rm H}\beta)_{\rm global}}{10^{3}\,{\rm km\,s^{-1}}}\right)^{2}, \quad (2.2.5)$$

It is important to note that we have simply re-scaled the empirical $R_{\rm BLR}\,({\rm H}\beta)$ vs $L_{5100}^{\rm local}$ relation to a $R_{\rm BLR}\,({\rm H}\beta)$ vs $L_{5100}^{\rm global}$ relation that is adjusted to predict the *same* $R_{\rm BLR}$ measurements. Consequently, we do not expect any systematic bias in $M_{\rm BH}$ measurements coming from intrinsic $L_{5100}^{\rm global}$-$L_{5100}^{\rm local}$ biases. The bias between $M_{\rm BHlocal}$ and $M_{\rm BHglobal}$ are simply the results of the intrinsic differences between the ${\rm FWHM_{local}}$ and ${\rm FWHM_{global}}$ (see §2.4.1). The small $M_{\rm BH}$ biases that we found are shown in the bottom right set of panels in Figure 2.2.5.

Table 2.7: *Virial BH mass calibrations of Equation 2.2.1 ($M_{BH} = K(L_\lambda)^\alpha FWHM^2$) based on different line width and luminosity combinations for 32/39 objects in our sample, calibrated against the Hβ virial mass calibration given in Equation. 2.2.4.* [a] *M_{BH} calibration based on local measurements.* [b] *M_{BH} calibration based on global measurements.* [c] *local M_{BH} calibrations corrected for the* small *systematic offsets that we found with respect to global M_{BH}. Note that the values in this table are valid for L in units of 10^{44} erg s^{-1} and FWHM in units of 1000 km s^{-1}. For these calibration we assume $f = 1$ which is appropriate for FWHM M_{BH} estimates.*

	Local[a]			global[b]			Local$^b_{corr}$		
	$\log K$	α	scatter (dex)	$\log K$	α	scatter (dex)	$\log K$	α	scatter (dex)
FWHM(Hα), L_{5100}	6.779	0.650	0.16	6.958	0.569	0.19	6.845	0.650	0.16
FWHM(Hα), L_{6200}	6.842	0.634	0.16	7.062	0.524	0.22	6.891	0.634	0.16
FWHM(Hα), L (Hα)	7.072	0.563	0.18	7.373	0.514	0.23	7.389	0.563	0.18
FWHM(Hβ), L_{5100}	6.721	0.650	0.00	6.864	0.568	0.00	6.740	0.650	0.00
FWHM(Mg II), L_{3000}	6.906	0.609	0.25	6.955	0.599	0.29	6.925	0.609	0.25
FWHM(C IV), L_{1450}	6.331	0.599	0.33	6.349	0.588	0.38	6.353	0.599	0.33

2.4.4.2 Other lines

In order to calibrate Hα, Mg II and C IV line measurements to match the $M_{\rm BH}$ (Hβ) predictions we follow standard procedures (e.g. McLure & Dunlop, 2004; Vestergaard & Peterson, 2006; Trakhtenbrot & Netzer, 2012) that basically rescale $R_{\rm BLR}$ (L_{5100}) to $R_{\rm BLR}$ (L_λ) (see Eqn. 2.2.3) and then rescale μ (λ) to $M_{\rm BH}$ (Hβ) where $\mu(\lambda) = G^{-1} R_{\rm BLR}$ (L_λ) FWHM (line)^2.

This approach assumes that $M_{\rm BH}$ scales as FWHM^2, which follows from a virialization of the line emitting region. According to the direct proportionality that we found between FWHM(Hβ), FWHM(Hα) and FWHM(Mg II) (see 2.4.3), it will be enough to assume virialization of the Hβ emitting region. We note that several previous studies have instead allowed total freedom to the dependence of $M_{\rm BH}$ on FWHM (e.g., Shen & Liu, 2012), instead of assuming a virial relation. However, there is no physical motivation for this approach (except perhaps for C IV) apart from the attempt to minimize residuals with regard to $M_{\rm BH}$ (Hβ). We focus on identifying those sources which appear to represent the largest deviation from virial equilibrium, and excluding them from the analysis. As explained in §2.4.3.4, these are the five sources with the largest deviations between FWHM(Hβ) and FWHM(Mg II), that are mostly small width (FWHM (Hβ) $< 4000\,{\rm km\,s^{-1}}$), high $L/L_{\rm Edd}$ ($\gtrsim 0.17$) sources , and the two BALQSOs. In such cases $M_{\rm BH}$ (Hα) and $M_{\rm BH}$ (Hβ) are the only methods providing reliable $M_{\rm BH}$ determination.

The results of the rescaled single epoch $M_{\rm BH}$ estimators based on Hα, Hβ, Mg II and C IV in 32/39 sources are summarized in Table 2.7 and shown in Figure 2.2.9 where the black solid lines represent the 1:1 relations. We also show the 7 removed sources; BALQSOs in green and objects with discrepant FWHM(Hβ) and FWHM(Mg II) in magenta.

Figure 2.2.9 shows that the main sources of scatter in all the $M_{\rm BH}$ relationships in the original sample are the above 7 sources. Removing these objects leaves almost perfect correlations ($r_{\rm s} > 0.85$, $P < 10^{-12}$) between mass estimates based on Hα, Hβ and Mg II and even C IV. In fact, the scatter in $M_{\rm BH}$ (Hα)-$M_{\rm BH}$ (Mg II) and $M_{\rm BH}$ (Hα)-$M_{\rm BH}$ (C IV) is reduced from 0.23 to 0.15 dex and from 0.29 to 0.16 respectively for the L_{6200}-FWHM(Hα) estimates. Unfortunately, it is not easy to identify and remove such objects from a sample where only the C IV line region is observable. We come back to this issue later in the chapter.

The use of L (Hα) in Xiao et al. (2011), as well as other studies (e.g., Greene & Ho, 2005), is motivated by the possibility of host-light contribution to L_{6200}, especially in low luminosity (low-redshift) AGN. However, as previously mentioned (§2.3), most of our objects have negligible host galaxy contamination, and we have accounted for it in the few objects where it is relevant. Thus, we can safely use L_{6200} for Hα-based $M_{\rm BH}$ estimates. In table 2.7 we present both L_{6200}-FWHM(Hα) and L (Hα)-FWHM(Hα) $M_{\rm BH}$ calibrations.

In Figure 2.2.9 we also present the best-fit relations that compare our new mass prescriptions with previously published ones (black dashed lines). Particularly we compared our new calibrations with the TN12 Mg II-based calibration, the Xiao et al. (2011) Hα-based calibration (an updated version of Greene & Ho (2005)) and the Vestergaard & Peterson (2006) C IV-based calibration. We note that these are somewhat simplified comparisons, as a proper analysis of the deviation from each $M_{\rm BH}$ calibration is not straightforward, due to the usage of different f factors; different $R_{\rm BLR} - L$ relations; assumed cosmology; and even of fitting procedures. Nevertheless, it is evident from the diagram that the deviation from the earlier mass estimates based on C IV are the largest among the three (bottom panel of Fig. 2.2.9).

2.4.4.3 X-Shooter versus SDSS $M_{\rm BH}$ estimates

In Fig. 2.2.10 we compare the $M_{\rm BH}$ estimations using the (lower-S/N) SDSS spectra and (higher S/N) X-Shooter spectra, by plotting Δ log $M_{\rm BH} \equiv \log\left(M_{\rm BH}\,({\rm line})\,/M_{\rm BH}\,({\rm H}\alpha)\right)$ for Mg II and C IV versus the S/N of the continuum around Mg II([S/N] (Mg II)). We note that the typical difference between the data sets is $(S/N)_{XSh} \simeq 4 \times (S/N)_{\rm SDSS}$. As expected (see §2.4.3), objects with unresolved absorption features or incomplete line profiles generally show the largest offsets in mass. Apart from these objects, the scatter in $M_{\rm BH}$ (C IV) and $M_{\rm BH}$ (Mg II) estimates is *independent* of the S/N. This is not surprising because of the good agreement between X-Shooter- and SDSS-based FWHM(C IV) measurements (see §2.4.3.1). We conclude that the scatter in Mg II- and C IV-based mass estimates is dominated by intrinsic differences between FWHM(Mg II)-FWHM(C IV) and FWHM(Hα) as well as between L_{5100}-L_{3000} and L_{6200}.

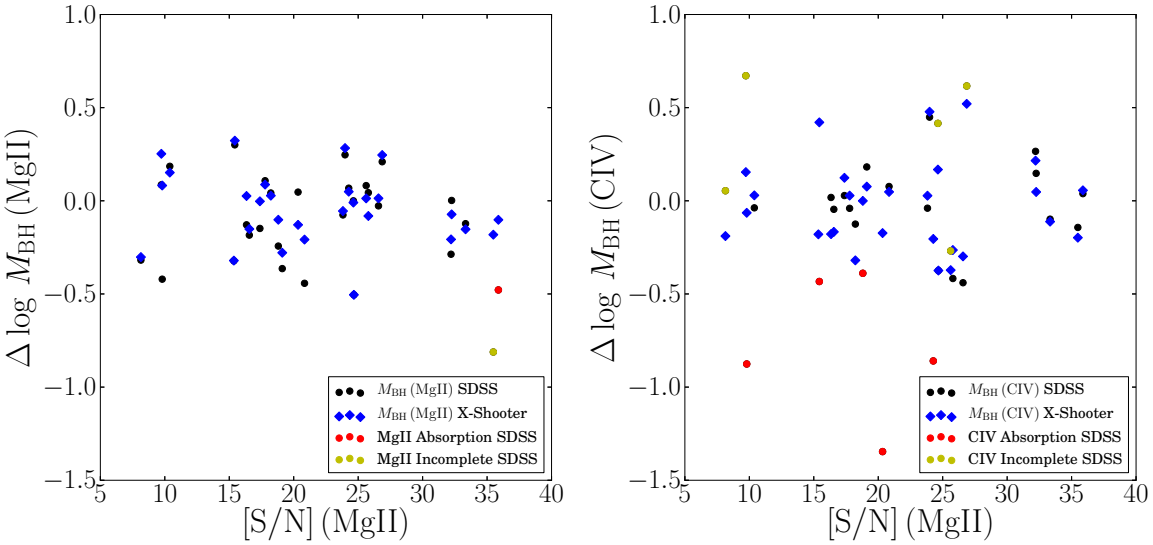

Figure 2.2.10: A comparison of $M_{\rm BH}$ estimates from X-Shooter and SDSS spectra. We show the offsets in mass estimates, $\Delta \log M_{\rm BH} \equiv \log\left(M_{\rm BH}\,({\rm line})\,/M_{\rm BH}\,({\rm H}\alpha)\right)$, vs. the S/N of the continuum around Mg II ([S/N] (Mg II)) using SDSS (black dots) and X-Shooter (blue diamonds) data for the Mg II (left panel) and C IV (right panel) lines. SDSS data with unresolved absorption features (red dots) or incomplete line profiles (yellow dots) are also shown.

2.4.5 The C iv line as a Black Hole mass estimator

As can be seen in Figure 2.2.8 and also mentioned in §§2.4.3, the width of C IV shows only weak correlations (if at all) with the widths of the other lines we study in this chapter. This result together with the significant blue-shifts observed in the C IV line center ($\Delta v = -1200 \pm 1000$) make mass estimates based on the C IV line significantly more uncertain. However, In high-z objects ($2 \lesssim z \lesssim 5$) C IV is the only prominent broad emission line that lies within the optical window. It is therefore important to explore possibilities to improve $M_{\rm BH}$ determination by means of C IV. There have been already some attempts in this direction. For instance, Runnoe et al. (2013) and Brotherton et al. (2015a) claim a correlation between the line peak ratio $L_P\,({\rm Si\,IV + O\,IV]}\,)\,/L_P\,({\rm C\,IV})$ and the FWHM ratio FWHM (C IV) /FWHM (Hβ) driven by Eigenvector 1 (Boroson & Green, 1992) that would help to reduce the scatter in $M_{\rm BH}$ from 0.43 dex to 0.30 dex, Denney et al. (2013) propose that having high quality spectra and using the velocity dispersion of the line ($\sigma_{\rm line}$), instead of FWHM, will lead to accurate $M_{\rm BH}$ estimations. However, Denney et al. (2013) sample is limited to only 6 objects and our larger, high quality sample does not show any correlation between $\sigma_{\rm line}$ (Hβ) and $\sigma_{\rm line}$ (C IV).

In the following section we test the Runnoe et al. (2013) suggested relation as well as other relationships that can be used to improve the C IV-based mass determination method.

Table 2.8: *Spearman correlation coefficients, probability, scatter, and the best fit parameters ($\log FWHM_{ratio} = \beta \log L_P^{ratio} + C$) between the listed quantities.*

	log (L_P (Si IV + O IV] λ1400) / L_P (C IV))					log (L_P (C III] λ1909) / L_P (C IV))				
	r_s	P	scatter(dex)	β	C	r_s	P(%)	scatter (dex)	β	C
log (FWHM (C IV) /FWHM (Hα))	0.36	0.02	0.35	0.76	-0.51	0.34	3	0.34	0.72	-0.55
log (FWHM (C IV) /FWHM (Hβ))	0.44	0.003	0.32	0.55	-0.31	0.47	0.2	0.30	0.57	-0.33
log (FWHM (C IV) /FWHM (Mg II))	0.51	0.003	0.28	0.69	-0.72	0.57	0.02	0.19	0.52	-0.52
log (FWHM (C IV) /FWHM (Hβ)) from R13	0.64	3×10^{-9}	0.26	0.57	-0.36	- - -	- - -	- - -	- - -	- - -

2.4.5.1 Rehabilitating C iv?

In Table 2.8 we show the correlation coefficient, correlation probability and scatter between $L_{\rm P}$ (Si IV + O IV]) /$L_{\rm P}$ (C IV) and FWHM (C IV) /FWHM (Hβ) as well as several other similar line peak and FWHM ratios that are listed in the table. In Figure 2.2.11 we compare such quantities.

As can be seen in table 2.8 and Fig. 2.2.11, we confirm the correlation reported by Runnoe et al. (2013), however with a lower level of significance and larger scatter. These differences may be attributed to the the smaller size of our sample (39 objects here vs. 85 in R13), and the somewhat lower S/N in the Hβ region for the fainter sources in our sample, compared with R13. We can also see in Table 2.8 and Fig. 2.2.11 that our best fit relation between $L_{\rm P}$ (Si IV + O IV]) /$L_{\rm P}$ (C IV) and FWHM (C IV) /FWHM (Hβ) (black solid line in top-middle panel) is in very good agreement with the one presented in R13 (red dashed line in top-middle panel).

We also find that $L_{\rm P}$ (C III]) /$L_{\rm P}$ (C IV) correlations are slightly stronger than the analogous $L_{\rm P}$ (Si IV + O IV]) /$L_{\rm P}$ (C IV) correlations. At the same time the strongest correlations are those involving these line peak ratios and FWHM (C IV) /FWHM (Mg II). These relationships can be used to derive "corrected" $M_{\rm BH}$ estimates in cases where the relevant line peak ratios can be observed.

Below we present the corrected $M_{\rm BH}$ that can be derived from C IV and Si IV+O IV] measurements:

$$M_{\rm BH}\,({\rm Mg\,II})_{\rm pred} = 1.13 \times 10^6 \left(\frac{L_{1450}}{10^{44}}\right)^{0.57} \times \left(\frac{\rm FWHM\,(C\,IV)}{10^3\,{\rm km\,s^{-1}}}\right)^2 \times \left(\frac{L_P\,({\rm Si\,IV + O\,IV]\ })}{L_P({\rm C\,IV})}\right)^{-1.66} \quad (2.2.6)$$

and from C IV and C III] measurements:

$$M_{\rm BH}\,({\rm Mg\,II})_{\rm pred} = 5.71 \times 10^5 \left(\frac{L_{1450}}{10^{44}\,{\rm erg\,s^{-1}}}\right)^{0.57} \times \left(\frac{\rm FWHM\,(C\,IV)}{10^3\,{\rm km\,s^{-1}}}\right)^2 \times \left(\frac{L_{\rm P}\,({\rm C\,III])}}{L_{\rm P}\,({\rm C\,IV})}\right)^{-2.09} . \quad (2.2.7)$$

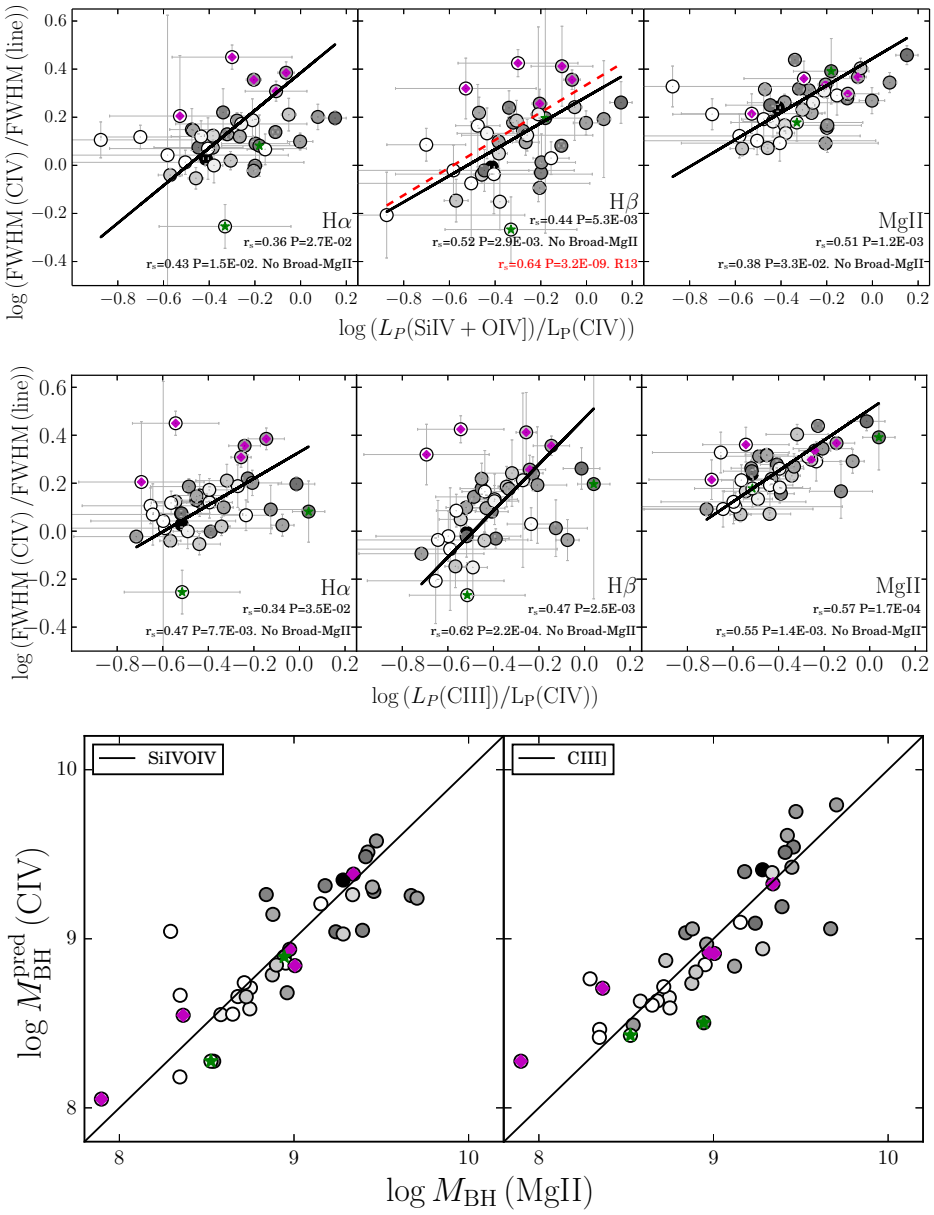

Figure 2.2.11: Top panel: Comparison of the Hα-C IV (left), Hβ-C IV (middle) and Mg II-C IV (right) FWHM ratios with the Si IV+O IV]- C IV line peak ratio.The Red dashed line represents the best-fit relation reported by Runnoe et al. (2013) and the black solid lines represent our best fit relation. Middle panel: same as top panel but this time we compare with the C III]- C IV line peak ratio. Bottom panel: Predicted M_{BH} masses using the correlations of the Mg II-C IV FWHM ratio with the Si IV+O IV]- C IV (bottom-left) and the C III]- C IV (bottom-right) line peak ratios. Green stars represent Broad absorption lines quasars (BALQSO) and magenta points represent the broad-Mg II objects. The black solid lines represent the 1:1 relation.

The confirmation of the Runnoe et al. (2013) correlation, and the new correlations reported here, should assist in rehabilitating C IV for more reliable $M_{\rm BH}$ measurements, by relying on the nearby Si IV+O IV] and/or C III] emission lines. Even for those combinations of observables which do not significantly reduce the scatter in $M_{\rm BH}$ determinations, they provide an improvement in the *accuracy* of rest-frame UV-based $M_{\rm BH}$ estimations since these prescriptions compensates the effect of $L/L_{\rm Edd}$ in the C IV profile.

Chapter 3

Can we improve C iv-based single epoch supermassive black hole mass estimations?

3.1 Introduction

The mass of SMBHs is known to be related to their host-galaxy properties through the so-called $M_{\rm BH}$-$\sigma_\star$ relation (e.g. Ferrarese & Merritt, 2000; Häring & Rix, 2004; Gültekin et al., 2009; Xiao et al., 2011; Kormendy & Ho, 2013; McConnell & Ma, 2013). Consequently, for a complete understanding of the formation and growth of SMBHs and their host galaxies it is crucial to obtain precise and accurate measurements of $M_{\rm BH}$.

The single epoch (SE) black hole mass estimation method is very broadly used on large samples of unobscured, type-I AGN (Croom et al., 2004; McLure & Dunlop, 2004; Onken et al., 2004; Fine et al., 2006; Shen et al., 2008; Rafiee & Hall, 2011; Trakhtenbrot & Netzer, 2012). This method relies on two basic ingredients: (1) the assumption of virialized gas kinematics in the broad line region (BLR) and (2) the empirical relation from reverberation mapping (RM) experiments between the BLR size ($R_{\rm BLR}$) and the continuum luminosity at al particular wavelength λ ($L_\lambda \equiv \lambda L(\lambda)$) where $R_{\rm BLR} = K'(L_\lambda)^\alpha$ with $\alpha \sim 0.5-0.7$ and K' a normalizing constant (Kaspi et al., 2000, 2005; Bentz et al., 2009; Park et al., 2012; Bentz et al., 2013).

Under these assumptions the full width at half maximum (FWHM) of the broad emission lines is a good proxy for the virial velocity of the BLR clouds. $M_{\rm BH}$ can thus be expressed as:

$$M_{\rm BH} = fG^{-1}R_{\rm BLR}V^2_{\rm BLR} = K(L_\lambda)^\alpha {\rm FWHM}^2. \tag{3.3.1}$$

Here G is the gravitational constant, f is a geometrical factor that accounts for the

unknown structure and inclination to the line of sight of the BLR. In this chapter, we assume $f = 1$, which is an appropriate median value for $M_{\rm BH}$ estimates using the FWHM (Woo et al., 2015). However, there is a large uncertainty in this value (50%) that can be even larger if it depends on luminosity and/or other line properties (e.g. equivalent widths, line offsets, FWHM; Shen, 2013; Collin et al., 2006). We will come back to this issue in chapter 4.

The most reliable RM-based $R_{\rm BLR}-L$ relation is the $R_{\rm BLR}\,({\rm H}\beta)-L_{5100}$ relation. This relation is the only one that has been established over a large number of sources and covering a large luminosity range ($10^{43} \lesssim L_{5100} \lesssim 10^{46}\,{\rm erg\,s^{-1}}$). As a consequence, SE $M_{\rm BH}$ calibrations for other lines need to be re-calibrated to match $M_{\rm BH}$ measurements based on Hβ and L_{5100}. Such re-calibrations are used to determine $M_{\rm BH}$ values at different redshifts where the Hβ line maybe too faint or impossible to detect directly. In optical surveys, the Hα (λ6526Å) and Hβ lines can be used up to $z \lesssim 0.8$ (e.g. Greene & Ho, 2005; Xiao et al., 2011; Shen & Liu, 2012), the Mg II λ2798 (hereafter Mg II) can assist for $M_{\rm BH}$ on sources where $0.6 \lesssim z \lesssim 2.2$ (e.g. McLure & Jarvis, 2002; Vestergaard & Osmer, 2009; Wang et al., 2009; Trakhtenbrot et al., 2011; Shen & Liu, 2012; Trakhtenbrot & Netzer, 2012) and the C IV λ1549 line (hereafter C IV) is used to estimate black hole masses at even higher redshifts ($2.0 \lesssim z \lesssim 5.0$; Vestergaard & Peterson, 2006; Park et al., 2013).

$M_{\rm BH}$ calibrations based on low ionization lines (i.e. Hα, and Mg II) generally show good agreement with the Hβ $M_{\rm BH}$ estimator with a typical scatter of $\lesssim 0.2$ dex (Greene & Ho, 2005; Xiao et al., 2011; Trakhtenbrot & Netzer, 2012). However, the analogue recalibration using the C IV high ionization line is more problematic and shows large scatter (0.4-0.5 dex) because of several issues. First, the width of C IV is only weakly correlated, if at all, with the width of the low ionization lines and presents large scatter, in many AGN samples (e.g., Baskin & Laor, 2005; Netzer et al., 2007; Shang et al., 2007; Shen et al., 2008; Fine et al., 2010; Ho et al., 2012; Shen & Liu, 2012; Trakhtenbrot & Netzer, 2012; Tilton & Shull, 2013). Second, the C IV integrated profiles show large blue-shifts (up to several thousands ${\rm km\,s^{-1}}$; Richards et al., 2002; Baskin & Laor, 2005; Shang et al., 2007; Richards et al., 2011) that indicates non virial motions. Third, Denney (2012) found that the core of the broad C IV line does not reverberate as a response to continuum variations. This implies that not only the innermost but also the *outermost* C IV emitting regions may not be virialized.

Given that C IV is the most widely used line for $M_{\rm BH}$ determination at high redshift ($z \gtrsim 2$) in optical surveys, it is crucial to design practical methodologies to mitigate the issues related to C IV-based $M_{\rm BH}$ determinations. There have been many efforts to improve single-epoch $M_{\rm BH}$ determinations from C IV (e.g. Vestergaard & Peterson, 2006; Denney et al., 2013; Park et al., 2013; Runnoe et al., 2013; Tilton & Shull, 2013; Brotherton et al., 2015a; Coatman et al., 2016). The studies of Denney et al. (2013) and Tilton & Shull (2013) claimed that in spectra of limited S/N and/or spectral resolution, FWHM(C IV) measurements are underestimating the "real" line widths, in objects with strong intrinsic absorption features that cannot be deblended from the emission lines.

This would partially explain the fact that about 40% of the objects show C IV profiles narrower than the Hβ profiles (Trakhtenbrot & Netzer, 2012). However, Corbin & Boroson (1996) found that even objects with no evidence of absorption features, show FWHM(C IV)<FWHM(Hβ). After correcting for intrinsic C IV absorption, Denney et al. (2013) claimed that although FWHM(C IV) still does not correlate well with FWHM(Hβ), σ(C IV) shows a strong correlation with σ(Hβ) and can safely be used for C IV based $M_{\rm BH}$ determinations. Motivated by this results, Park et al. (2013) obtained high quality data for 39 out of 45 objects of the RM experiments campaign (Bentz et al., 2009) and improved the Vestergaard & Peterson (2006) C IV-based $M_{\rm BH}$ estimator based on the σ(C IV). We note however that Denney et al. (2013) as well as Park et al. (2013) used non homogeneous and multi-epoch samples that could affect their results. In addition, $\sigma_{\rm line}$ measurements are highly dependent on the continuum determination method even in high quality data (Peterson et al., 2004; Mejía-Restrepo et al., 2016).

Recently, Coatman et al. (2017) found a strong correlation between the blue-shift of the C IV line centroid and FWHM (C IV) /FWHM (Hβ) for a sample of 66 high luminosity ($10^{46.5}$erg s^{-1} < $L_{\rm Bol}$ < $10^{47.5}$erg s^{-1}) and high redshift quasars ($z > 2.1$). They suggest that this correlation can assist to improve C IV-based black-hole masses reducing the scatter between C IV and Hα based $M_{\rm BH}$ determinations from 0.40dex to 0.24dex. However, this procedure is not practical because of the difficulty to accurately determine the redshift of the source without information from low ionization lines. Runnoe et al. (2013) and Brotherton et al. (2015a) used a sample of 85 low-redshift ($0.03 < z < 1.4$) and low-luminosity (43.37erg s^{-1} < log L_{5100} < 46.45erg s^{-1}) AGN with quasi-simultaneous UV and optical rest-frame spectra to propose a method to rehabilitate C IV for $M_{\rm BH}$ determination. The method consisted of using a correlation that they found between the Si IV+O IV] λ1400−C IV line peak intensity ratio and the Hβ−C IV FWHM ratio. Using this correlation it is possible to predict FWHM(Hβ) from measurements of the Si IV+O IV] λ1400 (Si IV+O IV] hereafter) emission to obtain more accurate C IV based mass measurements. They specifically claim that the scatter between C IV and Hβ estimations is reduced from 0.43 dex to 0.33 dex.

In our previous studies, we presented a sample of 39 high-quality, simultaneous (rest-frame) UV-optical spectra of type-1 AGN at z∼1.5 obtained with X-Shooter Capellupo et al. (2015, 2016). Using this sample, Mejía-Restrepo et al. (2016) were able to reproduce the correlation found in Runnoe et al. (2013) but with a weaker statistical significance. Mejía-Restrepo et al. (2016) also found a similar but alternative correlation between the C III] λ1909-C IV line peak intensity ratio and the Hβ−C IV FWHM ratio. In general, we found that the ratios of FWHM(C IV) to the FWHM of the Hα, Hβ and Mg II low ionization lines are correlated with both, the Si IV+O IV]−C IV and the C III] λ1909−C IVline peak ratios. In spite of these correlations, we found that none of them are able to reduce the scatter between C IV-based $M_{\rm BH}$ estimations and the low ionization line $M_{\rm BH}$ estimations.

It is important to point out that the findings of Coatman et al. (2017), Mejía-

Restrepo et al. (2016) and Runnoe et al. (2013) are all obtained from relatively small samples (230, 69 and 39 objects respectively) that map different regions of the parameter space of the AGN population (see §3.2). Thus, the significance of their findings may be affected by statistical fluctuation and/or could not be applicable to the overall population of non-obscure type-I AGN population.

The purpose of this chapter is to test on large survey quality samples the validity of these practical alternatives to improve C IV-based $M_{\rm BH}$ estimations proposed to date. To accomplish this goal, in this chapter we use data from the Sloan Digital Sky Survey (SDSS York et al., 2000).We select quasars with simultaneous spectral coverage of the Si IV+O IV], C IV, C III] λ1909 (C III] hereafter), and Mg II emission lines from the spectroscopic quasar catalogue of the SDSS-III data release 12 (DR12Q; Pâris et al., 2016) and the spectroscopic quasar catalogue from the SDSS-II data release 7 (DR7Q; Schneider et al., 2010). All the alternatives that we are testing here stand on correlations that relates FWHM (C IV) /FWHM (Hβ) with the C IV line itself or with the properties of emission lines or of continuum windows that are close the C IV line. Due to the lack of simultaneous coverage of C IV and Hβ lines in the optical SDSS survey, we will carry our analysis in terms of FWHM (C IV) /FWHM (Mg II) $\equiv$ FWHM [C IV/Mg II] instead of FWHM (C IV) /FWHM (Hβ). The reasons for this choice are that FWHM(Mg II) is known to be tightly correlated with FWHM(Hβ) and that $M_{\rm BH}$ estimations from these two emission lines are known to agree within 0.2dex of accuracy (e.g Wang et al., 2009; Shen & Liu, 2012; Trakhtenbrot & Netzer, 2012; Mejía-Restrepo et al., 2016). Thus, FWHM(Mg II) is a good proxy for FWHM(Hβ).

This chapter is structured as follows. In section §3.2 we present the samples and introduce the most relevant parameters that we measured for our analysis. In §3.3 we present and discuss our main results and in §3.4 we highlight our most important findings. Throughout this chapter we assume a flat ΛCDM cosmology with the following values for the cosmological parameters: $\Omega_\Lambda = 0.7$, $\Omega_{\rm M} = 0.3$ and $H_0 = 70\,{\rm km\,s^{-1}\,Mpc^{-1}}$.

3.2 Samples, Data and Analysis

In this section we describe in detail two large samples, namely, the SDSS DR7Q and the DR12Q samples, as well as three small samples taken from Coatman et al. (2017), Mejía-Restrepo et al. (2016) and Runnoe et al. (2013). We also describe the fitting procedure and the the emission line and continuum properties that were obtained for the analysis presented here.

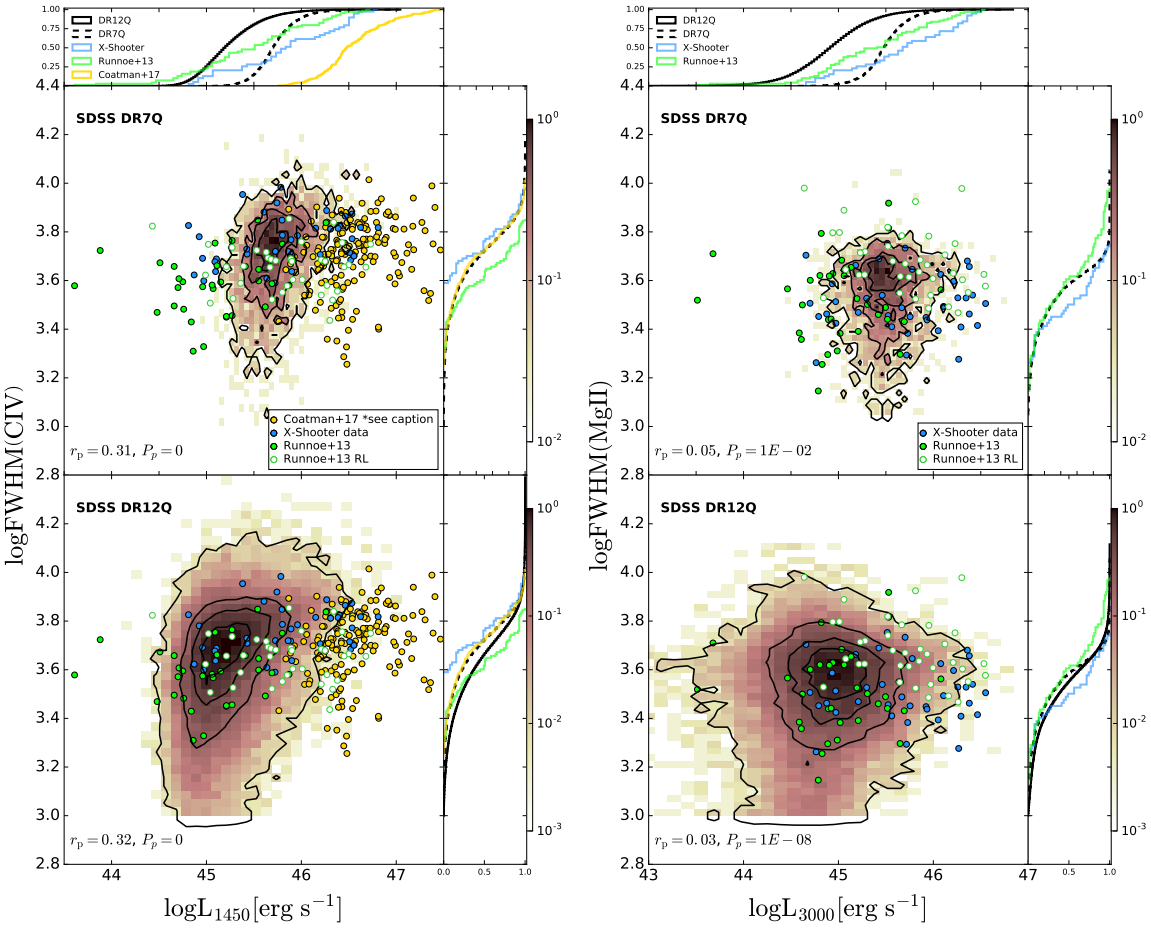

Figure 3.3.1: Left column: L_{1450}-FWHM(C IV) bi-dimensional distributions in the SDSS DR7Q (top-left) and DR12Q (bottom-left) samples. The intensity of the colour represents the relative density of points as shown in the colour bars on the right. The black thin lines represent the 25%, 50%, 75% and 99% contours centred at the maximum density point. In the top a right side diagrams we show the projected CDFs of L_{1450} and FWHM(C IV), respectively. We superimpose in each panel analogue data from the small X-Shooter, Runnoe+13 and Coatman+17 samples as summarized in the legend. Runnoe+13 is split in RL and RQ objects in the scatter plots. For the Coatman+17 sample we show L_{1350} as a proxy for L_{1450} (L_{1450} is not listed in Coatman et al., 2016). We also show the Pearson correlation coefficients (r_P) and associated probabilities (P_P) for upholding the null hypothesis of independence of the compared quantities. Right column: L_{3000}-FWHM(Mg II) bi-dimensional distributions. Description is identical to the left column. Coatman+17 data are not available for these quantities.

3.2.1 Large Samples

To accomplish our goal, we need to guarantee the simultaneous coverage of the Mg II C III] C IV and Si IV+O IV] and emission lines. According to the spectroscopic coverage of the DR7Q (3800-9200Å) and the DR12Q (3600-10400Å) samples, we selected objects with 1.79<z<2.0 and with $1.70 < z < 2.3$ respectively. These redshift constraints translate into a total of 4817 objects for the DR7Q catalogue and 69092 objects for the DR12Q catalogue. For the DR12Q sample we adopt the visually inspected redshifts from Pâris et al. (2016) and for the DR7Q sample we used the improved SDSS redshifts provided by Hewett & Wild (2010). The visually inspected redshift in the SDSS DR12Q catalogue have associated systematic errors of the order of 500 $\mathrm{km\,s^{-1}}$. Additionally, in many cases redshifts are estimated using the C IV line centre (Pâris et al., 2012). This makes line shift estimations in the SDSS DR12Q sample less reliable than in the DR7Q sample which have typical uncertainties of 200 $\mathrm{km\,s^{-1}}$.

3.2.2 Small Samples

We complement our analysis with three additional smaller samples with considerably higher-quality spectroscopic data. These samples correspond to the original samples used to propose the different methodologies to improve C IV-based M_{BH} estimations that we described in the introduction.

The first of these samples is described in Runnoe et al. (2013, the Runnoe+13 sample hereafter) consisting of 69 objects including 37 radio-loud (RL) and 32 radio-quiet (RQ) quasars with multi-epoch observations of the (rest-frame) X-ray, Ultraviolet (UV) and optical . The sample comprises objects with $0.03 < z < 1.4$ and $10^{43.6}\mathrm{erg\,s^{-1}} < L_{1450} < 10^{46.7}\mathrm{erg\,s^{-1}}$.

The second sample is described in Capellupo et al. (2016, the X-Shooter sample hereafter) consisting of 39 RQ quasars observed by the X-Shooter spectrograph that guaranteed simultaneous observations of the rest-frame UV and optical. The sample comprises objects with $1.45 < z < 1.69$ and $10^{44.8}\mathrm{erg\,s^{-1}} < L_{1450} < 10^{46.8}\mathrm{erg\,s^{-1}}$.

Finally, the sample described in Coatman et al. (2017, the Coatman+17 sample hereafter) consists of 230 RQ quasars with observations of the rest-frame UV and optical. The sample comprises objects with $1.5 < z < 4.0$ and $10^{45.7}\mathrm{erg\,s^{-1}} < L_{1350} < 10^{47.7}\mathrm{erg\,s^{-1}}$. This sample has not reported Mg II emission line measurements but includes Hα emission line measurements that can be used as a proxy for Mg II line measurements.

3.2.3 Line and continuum measurements

For each object in the SDSS DR7Q and DR12Q samples we fitted the line profiles of the Si IV+O IV], C IV, C III] and Mg II emission lines as described in Appendix B.1. From the best fit model of the emission lines of each object we measured the line FWHM, the velocity dispersion ($\sigma_{\rm line}$; following Peterson et al., 2004), the rest-frame equivalent width (EW (line)), the integrated line luminosity (L (line)) and the luminosity at the peak of the fitted profile ($L_{\rm peak}$ (line)). As line blue-shift indicators we measured two different quantities: (1) the shift of the emission line peak ($\Delta V_{\rm peak}$) and (2) the line centroid shift defined as the weighted shift of the entire profile ($\Delta V_{\rm line}$). For each line we also computed the monochromatic luminosities at different wavelengths ($L_\lambda \equiv \lambda\ L(\lambda)$). We particularly measured L_{1350}, L_{1450}, L_{2000} and L_{3000} that correspond to continuum windows adjacent to the Si IV+O IV], C IV, C III] and the Mg II emission lines, respectively. Finally, from the large DR7Q and DR12Q samples we excluded the Broad Absorption Line Quasar (BALQSO) and objects with unreliable fits following the strategy described in Appendix B.1. We ended up with 3267 objects from the DR7Q catalogue (out of 4817) and 35674 from the DR12Q catalogue (out of 69062 objects). In the case of the Runnoe+13, X-Shooter, and Coatman+17 samples we also extracted from the published data the measurements of the aforementioned quantities whenever available.

3.2.3.1 Line wing dependent and weakly dependent quantities

Mejía-Restrepo et al. (2016) showed that $\sigma_{\rm line}$ and L (line) are very sensitive to the continuum placement because of their strong dependence on the line wings. Analogously, $\Delta V_{\rm line}$ (C IV), one of the most widely used blue-shift indicators, is also affected by the continuum placement. This fact motivates us to use the alternative blue-shift estimators $\Delta V_{\rm peak}$ (see definition above). Similarly, EW (line) is also sensitive to continuum placement. We will consequently use $L_{\rm peak}$ (line) $/L_\lambda$ as proxy for EW (line) because it depends only weakly on continuum placement.

We thus have a set of quantities that are weakly sensitive to continuum placement given by FWHM, $L_{\rm peak}$ (line), $\Delta V_{\rm peak}$ and $L_{\rm peak}$ (line) $/L_\lambda$, as well as a set of quantities that are strongly affected by the placement of the continuum emission given by $\sigma_{\rm line}$, L (line), $\Delta V_{\rm line}$ and EW (line). We emphasize however that the latter quantities are also important because they carry information of the broadest components of the emission lines and of the innermost region of the BLR.

From all the quantities considered here, the most relevant parameters for our analysis are the following:

- L_{1450}
- L_{3000}

- FWHM(C IV)
- FWHM(Mg II)
- FWHM [C IV/Mg II] $\equiv$ FWHM (C IV) /FWHM (Mg II)
- $L_{\rm peak}$ [C IV/SiOIV] $\equiv L_{\rm peak}$ (C IV) $/L_{\rm peak}$ (Si IV + O IV])
- $L_{\rm peak}$ [C IV/C III]] $\equiv L_{\rm peak}$ (C IV) $/L_{\rm peak}$ (C III])
- $L_{\rm peak}$ $\left[\text{C IV}/1450\text{Å}\right] \equiv L_{\rm peak}$ (C IV) $/L\left(1450\text{Å}\right)$
- $\Delta V_{\rm line}$ (C IV), blue-shift of the C IV line centroid.
- $\Delta V_{\rm peak}$ (C IV), blue-shift of the C IV line peak.

In Figures 3.3.1, 3.3.2, 3.3.3 and 3.3.4 we present relevant information associated to these quantities. First, In Fig. 3.3.1 we show the bi-dimensional distribution of log FWHM (C IV) versus log L_{1450} (left column) and log FWHM (Mg II) versus log L_{3000} (right column) for the DR7Q (top panels) and the DR12Q (bottom panels) samples. In Figures 3.3.2 and 3.3.3 we show the bi-dimensional distributions of log FWHM (C IV) and log FWHM [C IV/Mg II] versus log $L_{\rm peak}$ [C IV/SiOIV] (left), log $L_{\rm peak}$ [C IV/C III]] (centre-left) and log $L_{\rm peak}$ $\left[\text{C IV}/1450\text{Å}\right]$ (centre-right) of the DR7Q and the DR12Q samples respectively. Finally, in Figure 3.3.4 we show the bi-dimensional distributions of log FWHM [C IV/Mg II] versus $\Delta V_{\rm peak}$ (C IV) and $\Delta V_{\rm line}$ (C IV) of the DR7Q (columns 1 and 2 from left to right) and the DR12Q (columns 3 and 4) samples. We also show the cumulative distribution funtion (CDF) of all the quantities and superimpose the analogue X-Shooter, Runnoe+13 and Coatman+17 data whenever the information is available in the literature. We also show the Pearson correlation coefficient ($\rm r_P$) for the DR7Q and DR12Q bi-dimensional distribution of the associated quantities. The associated probability for upholding the null hypothesis ($\rm P_P$) is also shown whenever $\rm P_P > 1 \times 10^{-20}$ otherwise it is approximated to $\rm P_P = 0$.

As can be observed from all the figures described above, all samples used for this chapter are subject to different limitations and, potentially, different selection effects and biases. On the one hand, large samples have the advantage of sampling the overall quasar population. However, they not only have relatively low data quality but are also limited at low luminosity (because of flux limits) and high luminosities (because of the upper redshift cuts Labita et al., 2009). On the other hand, our small samples have very good data quality but can only barely represent the overall quasar population. In Appendix B.2 we compare all the samples and discuss the advantages and limitations associated to them.

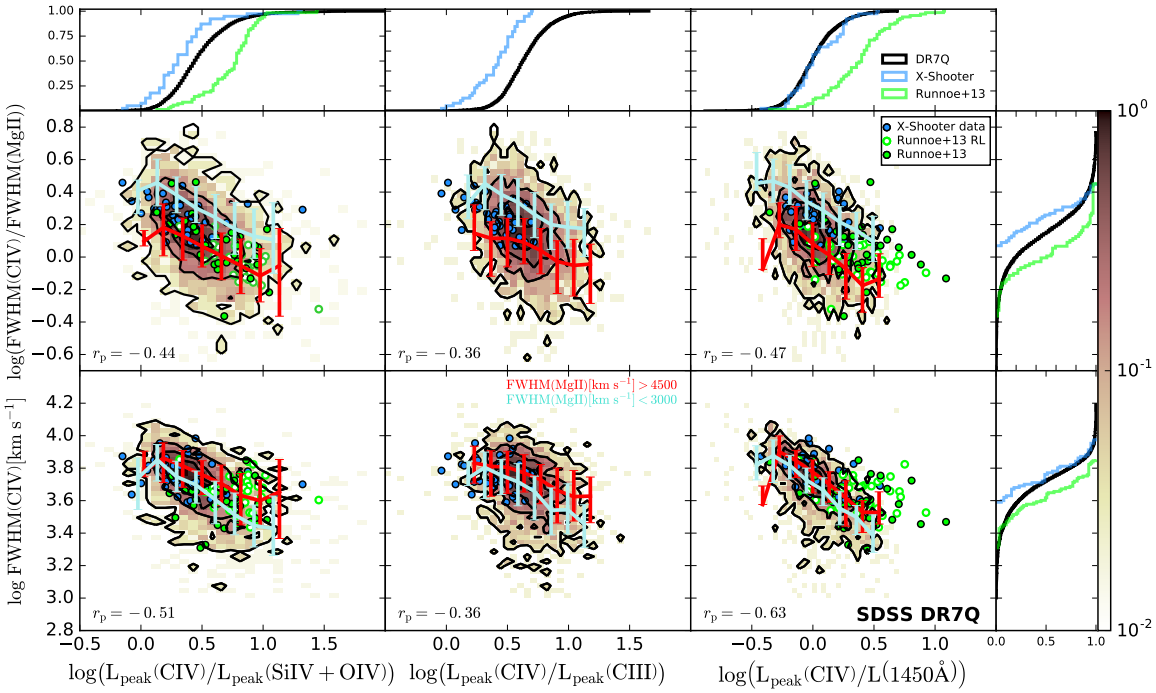

Figure 3.3.2: Bidimensional distributions of FWHM [C IV/Mg II] (top-row) and FWHM(C IV) (bottom row) vs $L_{\rm peak}$ [C IV/SiOIV] (left-column), $L_{\rm peak}$ [C IV/C III]] (centre-column) and $L_{\rm peak}$ [C IV/1450Å] (right-column) in the **SDSS DR7Q** sample. The intensity of the colour represents the relative density of points as shown in the colour bar on the right. The black thin lines represent the 25%, 50%, 75% and 99% contours centred at the maximum density point. The projected CDFs of each of the quantities are also shown in the right and top side diagrams. We superimpose to each panel analogue data of the Runnoe+13 and X-Shooter small samples as indicated in the legends. Coloured trend lines represent the median values of FWHM [C IV/Mg II] (middle panels) and FWHM(C IV) (bottom panels) as a function of the different line peak ratios for objects with FWHM (Mg II) < 3000km s^{-1} (light-turquoise) and FWHM (Mg II) > 4500km s^{-1} (red). The dispersion bars represent the 1-σ dispersion of the points around these trends. Note that the dynamic range that is shown for FWHM(C IV) and FWHM(Mg II) coincides (1.6dex). The same situation occurs with the dynamic range that is shown for $L_{\rm peak}$ [C IV/SiOIV], $L_{\rm peak}$ [C IV/C III]] and $L_{\rm peak}$ [C IV/1450Å] (2.5dex). We also show the correlation coefficient r_P. In all these cases $P_P < 10^{-90}$ and are not shown in the panels.

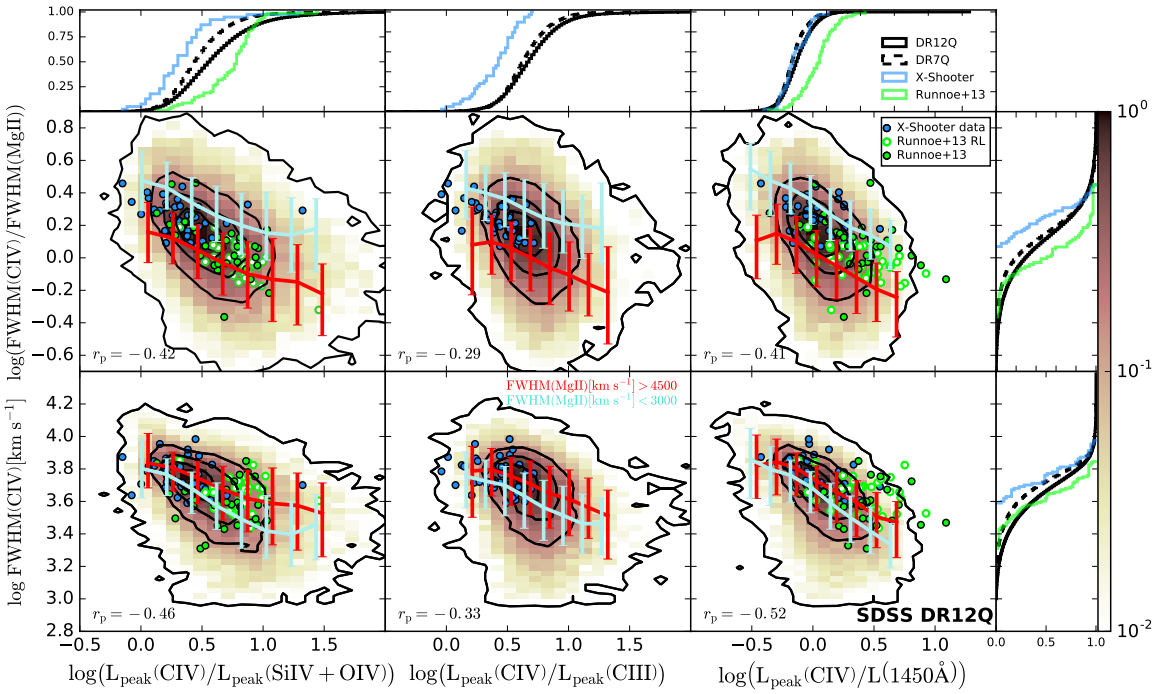

Figure 3.3.3: As in Figure 3.3.2 but for the **SDSS DR12Q** sample.

3.3 Results

In this section we explore in detail the different methods that have been proposed by Runnoe et al. (2013), Mejía-Restrepo et al. (2016) and Coatman et al. (2017) to improve C IV-based $M_{\rm BH}$ estimations. First we will analyse our results from the largest SDSS DR7Q and DR12Q samples to subsequently contrast them with those obtained from the Runnoe+13, X-Shooter and Coatman+17 samples and discuss the possible problems in the analysis done with such small samples.

3.3.1 SDSS DR7Q and DR12Q samples

3.3.1.1 Line Peak Ratios

Here, we first explore the statistical significance of the anti-correlations that link FWHM [C IV/Mg II] with $L_{\rm peak}$ [C IV/SiOIV], $L_{\rm peak}$ [C IV/C III]], and $L_{\rm peak}$ [C IV/1450Å] and which are used to improve C IV-based $M_{\rm BH}$ estimations. The reason to include $L_{\rm peak}$ [C IV/1450Å] in this analysis, which has not been considered in the literature, is its independence on other emission lines. Hereafter we will refer to these three quantities as the line peak ratio quantities.

Figures 3.3.2 and 3.3.3 show the bidimensional distributions of log FWHM (C IV)

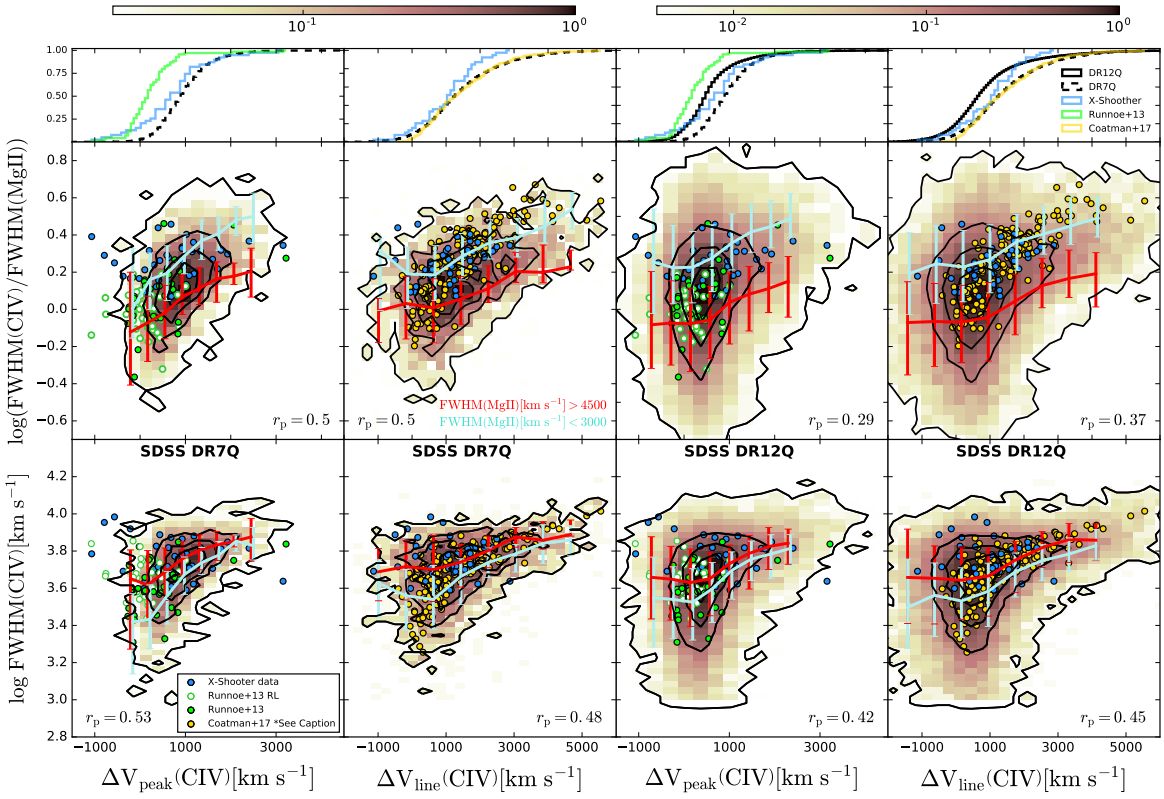

Figure 3.3.4: Bidimensional distributions of FWHM (C IV) /FWHM (Mg II) (top-panels) and FWHM (C IV) (bottom panels) vs the C IV blueshift proxies ΔV_{peak}(left) and ΔV_{line} (right) in the SDSS DR7Q (two left columns) and DR12Q (two right columns) samples. The intensity of the colour represents the relative density of points as shown in the colour bar on the top. The black thin lines represent the 25%, 50%, 75% and 99% contours centred at the maximum density point. The small samples are superimposed as indicated in the legends. The projected CDFs of ΔV_{peak} and ΔV_{line} are also shown in the top diagrams. In Coatman+17 sample there are not available measurements for the FWHM(Mg II). We then used 0.75FWHM (Hα) as a proxy for FWHM(Mg II) where 0.75 represent the median value of FWHM (Mg II) /FWHM (Hα) in the X-Shooter sample from Mejía-Restrepo et al. (2016). Coloured trend lines represent the median values of FWHM [C IV/Mg II] (middle panels) and FWHM(C IV) (bottom panels) as a function of the different blueshift estimators for objects with FWHM (Mg II) < 3000km s^{-1} (light-turquoise) and FWHM (Mg II) > 4500km s^{-1} (red). The dispersion bars represent the 1-σ dispersion of the points around these trends. Measurements of the blue-shift are less reliable in the DR12Q sample than in the DR7Q sample because of the redshift determination (see §3.2). We also show the correlation coefficient r_P. In all these cases $P_P < 10^{-90}$ and are not shown in the panels.

Table 3.1: *Scatter found in correlations between the listed quantities in the DR7Q and DR12Q samples*

	scatter			
	FWHM [C IV/Mg II]		FWHM(C IV)	
	DR7Q	DR12Q	DR7Q	DR12Q
$L_{\rm peak}$ [C IV/SiOIV]	0.21	0.27	0.17	0.21
$L_{\rm peak}$ [C IV/C III]]	0.22	0.29	0.19	0.23
$L_{\rm peak}$ [C IV/1450Å]	0.20	0.25	0.14	0.19
$\Delta V_{\rm peak}$ (C IV)	0.19	0.28	0.16	0.22
$\Delta V_{\rm line}$ (C IV)	0.21	0.29	0.19	0.24

(bottom row) and log FWHM [C IV/Mg II] (middle row) versus log $L_{\rm peak}$ [C IV/SiOIV] (left), log $L_{\rm peak}$ [C IV/C III]] (middle-left) and log $L_{\rm peak}$ [C IV/1450Å] (middle-right) for the SDSS DR7Q and DR12Q samples respectively. We also show the Pearson correlation coefficients (r_p) and associated probabilities of upholding the null hypothesis (P_p). The reader can notice that we are mapping the same dynamical range for log FWHM (C IV) and log FWHM [C IV/Mg II] (1.6 dex in both cases) as well as for log $L_{\rm peak}$ [C IV/SiOIV], log $L_{\rm peak}$ [C IV/C III]] and log $L_{\rm peak}$ [C IV/1450Å] (a total of 2.5 dex in all of them).

We can see that FWHM [C IV/Mg II] as well as FWHM(C IV) are anti-correlated with $L_{\rm peak}$ [C IV/1450Å], $L_{\rm peak}$ [C IV/SiOIV] and $L_{\rm peak}$ [C IV/C III]] in both SDSS quasar samples. By looking at the r_p values, we observe that in most cases the anti-correlations of the three line peak ratio quantities with FWHM(C IV) are tighter than those with FWHM [C IV/Mg II] with the exception of $L_{\rm peak}$ [C IV/C III]] in the DR7 sample where the r_p values are equal. Furthermore, we find that the scatter of the correlations associated to FWHM(C IV) are smaller than in those associated to FWHM [C IV/Mg II] in both SDSS quasar samples as summarize in Table 3.1.

One possibility to explain this behaviour is that the correlations associated to FWHM [C IV/Mg II] are caused by the more fundamental FWHM(C IV) correlations. This interpretation is supported by the tight correlation between FWHM(C IV) and FWHM [C IV/Mg II] that we find in both SDSS samples ($r_p = 0.71$ in both cases). Thus, FWHM [C IV/Mg II] is just increasing the scatter of the original correlations with FWHM(C IV).

To check this idea we first subdivided our DR7Q and DR12Q samples into two groups: Objects with FWHM (Mg II) $< 3000 {\rm km\,s^{-1}}$ (narrow-group) and objects with FWHM (Mg II) $> 4500 {\rm km\,s^{-1}}$ (broad-group) corresponding to the lower and upper 25%. Then, we binned each group by the line peak ratio quantities. For each bin we computed the median value of FWHM [C IV/Mg II] and FWHM(C IV) and the corresponding 1-σ scatter. The light-turquoise and red solid lines in Figs. 3.3.2 and 3.3.3 represent the median values and corresponding 1-σ dispersion in the narrow- and broad-groups, respectively. We can see that light-turquoise and red lines are very close to each other and that their dispersion bars overlap in the diagrams associated to FWHM(C IV) (bottom panels). In those panels the median red lines are just *slightly above* the light-

turquoise lines (roughly 0.07 dex) in all diagrams. However, in those diagrams associated to FWHM [C IV/Mg II] (middle panels) we can see a clearer separation between light-turquoise and red lines. Particularly red lines (FWHM (Mg II) $> 4500 \mathrm{km\,s^{-1}}$) are now roughly 0.3 dex *under* the light-turquoise lines (FWHM (Mg II) $< 3000 \mathrm{km\,s^{-1}}$) in all diagrams. This indicates that FWHM(Mg II) is driving the dispersion in the correlation between FWHM [C IV/Mg II] and the line peak ratio quantities.

To obtain further support for the previous finding, we looked at the residuals of the line peak ratios when expressed as a function of FWHM(C IV). In the case that FWHM(Mg II) is driving the dispersion in the FWHM [C IV/Mg II] correlations, we would find significant anti-correlation between these residuals and FWHM(Mg II). To address this, we fit the line peak ratios in terms of FWHM(C IV) and FWHM [C IV/Mg II] using bisector linear regressions. We find that for the peak ratios as functions of FWHM [C IV/Mg II], all the line-peak-ratio-residuals are significantly anti-correlated with FWHM(Mg II) ($|r_p| > 0.41$ in both samples) as expected. Moreover, for the line peak ratios versus FWHM(C IV) we do not find any significant correlations between any of the residuals with FWHM(Mg II) ($|r_p| < 0.23$ in both samples).

An additional test consists of estimating the statistical significance of the difference between the correlation coefficients associated to FWHM(C IV) and those associated to FWHM [C IV/Mg II] in both SDSS quasar samples. The William's test, using Fisher-z transformations, provides a procedure to test the equality of two Pearson correlation coefficients obtained from the same sample and sharing one common variable (Dunn & Clark, 1969). By applying this method to the correlations of FWHM(C IV) and FWHM [C IV/Mg II] with the common variable L_{peak} [C IV/SiOIV], we find an associated probability for upholding the null hypothesis of $P_{\mathrm{William}} < 10^{-5}$ in both SDSS quasar samples. This result discards the equivalence of both the FWHM(C IV)-L_{peak} [C IV/SiOIV] and the FWHM [C IV/Mg II]-L_{peak} [C IV/SiOIV] correlations coefficients. We find similar behaviours for the case of the FWHM(C IV)-L_{peak} $\left[\mathrm{C\,IV/1450\AA}\right]$ and FWHM [C IV/Mg II]-L_{peak} $\left[\mathrm{C\,IV/1450\AA}\right]$ correlations where we find $P_{\mathrm{William}} < 10^{-14}$ in both samples. Finally, for the case of the FWHM(C IV)-L_{peak} [C IV/C III]] and FWHM [C IV/Mg II]-L_{peak} [C IV/C III]] correlations we find $P_{\mathrm{William}} = 10^{-9}$ in the DR12Q sample.

From all the evidence that we have collected, we can conclude that the prescriptions proposed by Runnoe et al. (2013) and Mejía-Restrepo et al. (2016) are of limited applicability for correcting C IV-based estimates of M_{BH} because the correlations between the line peak ratios and FWHM(C IV) are statistically stronger and very likely causing the weaker correlations associated to FWHM [C IV/Mg II].

3.3.1.2 C iv blueshifts

We continue to test whether or not the use of ΔV_{line} (C IV) proposed by Coatman et al. (2017) can be used to improve C IV-based measurements. In addition to ΔV_{line} (C IV)

we will also include $\Delta V_{\rm peak}$ (C IV) in our analysis. The reason for this choice is the better stability of $\Delta V_{\rm peak}$ (C IV) to continuum placement as we discussed in § 3.2.

In Fig. 3.3.4 we show the bi-dimensional distribution of FWHM [C IV/Mg II] and FWHM(C IV) versus the C IV blue-shift indicators $\Delta V_{\rm peak}$ (C IV) and $\Delta V_{\rm line}$ (C IV) in both SDSS samples. In each panel we map the same dynamic range for FWHM(C IV) and FWHM [C IV/Mg II]. We also present the Pearson correlation coefficients for each diagram.

Fig. 3.3.4 demonstrates that FWHM [C IV/Mg II] and FWHM(C IV) are both correlated with $\Delta V_{\rm peak}$ (C IV) and $\Delta V_{\rm line}$ (C IV) in both SDSS samples. It is also noticeable that in most cases, the correlations between both blue-shift estimators and FWHM(C IV) are tighter than with FWHM [C IV/Mg II]. The only exception is with $\Delta V_{\rm line}$ (C IV) in the DR7Q sample where both correlations show similar significance. We can also notice in Table 3.1 that the scatter of the FWHM(C IV) correlations is smaller than the scatter in the corresponding FWHM [C IV/Mg II] correlations in both SDSS samples. These results would indicate that the correlations associated to FWHM(C IV) are causing the correlations associated to FWHM [C IV/Mg II].

We repeated the same three tests to further check the reliability of these results. First, when dividing the samples into two subsets according to their FWHM(Mg II), we find that the separation of the median trends of objects with FWHM (Mg II) < 3000 of those with FWHM (Mg II) $> 4500 {\rm km\,s^{-1}}$ (light-turquoise and red lines in Fig. 3.3.4) is increased from roughly -0.08 dex in the FWHM(C IV) diagrams to roughly 0.25 dex in the FWHM [C IV/Mg II] diagrams. Second, the analysis of residuals suggests significant anti-correlations with FWHM(Mg II) in all the blue-shift-residuals associated to FWHM [C IV/Mg II] ($|r_s| > 0.36$ in both samples) and no correlations with FWHM(Mg II) in all the blue-shift-residuals associated to FWHM(C IV) ($|r_s| < 0.10$ in both samples). Finally, the relative significance test shows that FWHM(C IV) correlations are indeed stronger than the FWHM [C IV/Mg II] correlations ($\rm P_{William} < 0.006$) for $\Delta V_{\rm peak}$ (C IV) and $\Delta V_{\rm line}$ (C IV) in the DR12Q sample and for $\Delta V_{\rm line}$ (C IV) in the DR7Q sample. This test shows that the FWHM(C IV)-$\Delta V_{\rm line}$ (C IV) and the FWHM [C IV/Mg II]-$\Delta V_{\rm line}$ (C IV) correlation coefficients in the DR7Q samples (0.48 and 0.50 respectively) are not statistically different to each other ($\rm P_{William} = 0.1$, smaller than two-sigma significance). All these results support idea that the FWHM(C IV) correlations with the C IV blue-shifts are the main cause for the analogue correlations with FWHM [C IV/Mg II] and suggest that the prescription suggested by Coatman et al. (2017) is of limited applicability to improve C IV mass measurements.

3.3.2 Small Samples

We continue our analysis exploring the small samples described in §3.2. Below we analyse the behaviour of the line peak ratios and the blue-shift relations with FWHM(C IV) and FWHM [C IV/Mg II] in those samples and discuss the similarities and divergences

Table 3.2: *Pearson correlation coefficients of (1)* $\log FWHM(C\,\textsc{iv})$ *and (2)* $\log FWHM[C\,\textsc{iv}/Mg\,\textsc{ii}]$ *versus the line peak quantities in (a) the X-Shooter sample, (b) the Runnoe+13 sample, (c) the combination of the X-Shooter and Runnoe+13 samples and (d) the combination of the X-Shooter and Runnoe+13 samples excluding the RL objects.* $L_{\rm peak}\,[C\,\textsc{iv}/C\,\textsc{iii}]]$ *measurements are not available for the Runnoe+13 sample.*

	X-Sh[a]		R+13[b]		Both[c]		Both RQ[d]	
	1	2	1	2	1	2	1	2
$\log L_{\rm peak}$ [C IV/SiOIV]	-0.27	-0.46	-0.02	-0.60	-0.44	-0.65	-0.54	-0.54
$\log L_{\rm peak}$ [C IV/1450Å]	-0.50	-0.36	-0.23	-0.38	-0.52	-0.59	-0.60	-0.59
$\log L_{\rm peak}$ [C IV/C III]]	-0.25	-0.56	–	–	–	–	–	–

with respect to our findings in the large SDSS samples.

3.3.2.1 Line Peak Ratios

Given that line peak related information is only available for the X-Shooter and Runnoe+13 samples we limit the analysis of the line peak ratios to these samples. In addition to the SDSS data, in Figures 3.3.2 and 3.3.3 we also show the data points and distribution functions associated with the X-Shooter (light-blue dots) and Runnoe+13 samples (lime open dots and lime filled dots for RL and RQ objects, respectively).

As we discuss in Appendix B.2, we remark that both Runnoe+13 and the X-Shooter samples are not complete. Indeed, Runnoe+13 and X-Shooter samples are sampling totally different regions of the parameter spaces determined by (1) the peak quantities and FWHM [C IV/Mg II] and by (2) the line peak quantities vs FWHM(C IV). The Runnoe+13 sample has a large number of RL objects. In consequence, we would expect that the combination of the X-Shooter and the Runnoe+13 samples will return a closer representation of the total type-1 AGN population after the exclusion of the RL objects from the Runnoe+13 sample.

In table 3.2 we show the correlation coefficients of the line peak quantities versus FWHM(C IV) (1) and FWHM [C IV/Mg II] (2) in the following configurations:

- The individual X-Shooter and Runnoe+13 samples (a and b).
- The combination of the X-Shooter and the Runnoe+13 samples including RL objects (c).
- The combination of the X-Shooter and the Runnoe+13 samples excluding RL objects (d).

From the information in table 3.2 we can observe that for the individual samples in most cases the correlations of FWHM [C IV/Mg II] with the line peak quantities are tighter than those associated with FWHM(C IV). The same behaviour is found for the

Table 3.3: *Absolute values of the Pearson correlation coefficients ($|r_p|$) of the quantities in the first column versus FWHM(C IV) (1) and FWHM[C IV/Mg II](2). The central values correspond to the medians obtained from the 100 randomly generated sub-samples selected to have flat distributions in L_{1450}(a),FWHM(C IV)(b), FWHM[C IV/Mg II](c), and L_{1450}-FWHM(C IV)(d) from the SDSS DR7Q and DR12Q samples. Errors correspond to the central 68% of the $|r_p|$ distribution.*

Random Sampling ⇒	L_{1450}[a]				FWHM(C IV)[b]				FWHM [C IV/Mg II][c]				L_{1450}-FWHM(C IV)[d]			
	DR12Q		DR7Q		DR12Q		DR7Q		DR12Q		DR7Q		DR12Q		DR7Q	
	1	2	1	2	1	2	1	2	1	2	1	2	1	2	1	2
L_{peak} [C IV/SiOIV]	$0.63^{+0.03}_{-0.03}$	$0.55^{+0.03}_{-0.04}$	$0.59^{+0.10}_{-0.11}$	$0.52^{+0.09}_{-0.09}$	$0.58^{+0.05}_{-0.04}$	$0.55^{+0.05}_{-0.05}$	$0.61^{+0.08}_{-0.06}$	$0.54^{+0.08}_{-0.08}$	$0.58^{-0.06}_{-0.04}$	$0.57^{+0.04}_{-0.05}$	$0.62^{+0.08}_{-0.10}$	$0.57^{+0.08}_{-0.08}$	$0.49^{+0.02}_{-0.02}$	$0.47^{+0.02}_{-0.02}$	$0.61^{+0.04}_{-0.04}$	$0.56^{+0.05}_{-0.04}$
L_{peak} [C IV/C III]]	$0.37^{+0.04}_{-0.04}$	$0.37^{+0.04}_{-0.04}$	$0.37^{+0.11}_{-0.11}$	$0.37^{+0.11}_{-0.12}$	$0.42^{+0.05}_{-0.06}$	$0.41^{+0.04}_{-0.05}$	$0.44^{+0.11}_{-0.11}$	$0.42^{+0.11}_{-0.12}$	$0.42^{+0.06}_{-0.04}$	$0.37^{+0.05}_{-0.07}$	$0.49^{+0.07}_{-0.13}$	$0.49^{+0.09}_{-0.10}$	$0.36^{+0.03}_{-0.02}$	$0.36^{+0.02}_{-0.03}$	$0.46^{+0.05}_{-0.06}$	$0.42^{+0.05}_{-0.05}$
L_{peak} [C IV/1450Å]	$0.70^{+0.03}_{-0.02}$	$0.56^{+0.03}_{-0.04}$	$0.72^{+0.06}_{-0.08}$	$0.52^{+0.09}_{-0.11}$	$0.62^{+0.03}_{-0.04}$	$0.52^{+0.05}_{-0.04}$	$0.67^{+0.05}_{-0.08}$	$0.53^{+0.09}_{-0.06}$	$0.59^{+0.04}_{-0.05}$	$0.49^{+0.05}_{-0.05}$	$0.73^{+0.07}_{-0.09}$	$0.61^{+0.09}_{-0.09}$	$0.57^{+0.01}_{-0.02}$	$0.49^{+0.02}_{-0.02}$	$0.69^{+0.03}_{-0.04}$	$0.54^{+0.05}_{-0.04}$
ΔV_{peak} (C IV)	$0.48^{+0.04}_{-0.05}$	$0.42^{+0.02}_{-0.03}$	$0.60^{+0.09}_{-0.11}$	$0.56^{+0.08}_{-0.09}$	$0.44^{+0.05}_{-0.06}$	$0.37^{+0.06}_{-0.05}$	$0.62^{+0.08}_{-0.09}$	$0.58^{+0.08}_{-0.10}$	$0.42^{+0.06}_{-0.05}$	$0.34^{+0.06}_{-0.06}$	$0.67^{+0.06}_{-0.11}$	$0.64^{+0.06}_{-0.06}$	$0.48^{+0.02}_{-0.02}$	$0.41^{+0.03}_{-0.02}$	$0.60^{-0.05}_{+0.04}$	$0.57^{+0.05}_{-0.04}$
ΔV_{line} (C IV)	$0.62^{+0.03}_{-0.03}$	$0.54^{+0.04}_{-0.04}$	$0.54^{+0.08}_{-0.09}$	$0.56^{+0.08}_{-0.09}$	$0.42^{+0.05}_{-0.06}$	$0.41^{+0.05}_{-0.06}$	$0.55^{+0.09}_{-0.09}$	$0.55^{+0.09}_{-0.08}$	$0.42^{+0.04}_{-0.05}$	$0.40^{+0.05}_{-0.05}$	$0.63^{+0.07}_{-0.10}$	$0.65^{+0.06}_{-0.08}$	$0.46^{+0.02}_{-0.02}$	$0.45^{+0.02}_{-0.03}$	$0.52^{+0.04}_{-0.05}$	$0.56^{+0.04}_{-0.05}$

combination of both samples including the RL objects. However, we find that when the RL objects are excluded from the analysis the FWHM [C IV/Mg II] and FWHM(C IV) correlations coefficients are statically indistinguishable.

3.3.2.2 C iv blueshifts

Before reporting the results of our comparative analysis for the Coatman+17 sample, we remark that this sample leans towards large luminosity objects as can be seen in Fig. 3.3.1. Nonetheless, its ΔV_{line} (C IV) and FWHM(C IV) distribution are in very good agreement with the SDSS-DR7Q sample (see Appendix B.2 and Figures 3.3.1, 3.3.4 for detalis).

Using the results reported in Coatman et al. (2017), we find that in their sample ΔV_{line} (C IV) is very tightly correlated with FWHM(C IV) ($r_p = 0.82$). However, we also find that the ΔV_{line} (C IV)-FWHM (C IV) /FWHM (Hα) Pearson correlation coefficient is essentially equal ($r_p = 0.83$). It is also remarkable that Fig. 9 in Coatman et al. (2017) shows that the scatter in the FWHM (C IV) /FWHM (Hα) vs ΔV_{line} (C IV) correlation is clearly dominated by FWHM(Hα). These results support our hypothesis that the FWHM(C IV)-ΔV_{line} (C IV) correlation is the driver of the FWHM (C IV) /FWHM (Hα)-ΔV_{line} (C IV) correlation.

3.3.3 Resampling tests

In this subsection we present different tests designed to check the validity of our findings. They consist of re-sampling our SDSS DR7Q and DR12Q samples in four different ways.

- Flat distribution in L_{1450}.
- Flat distribution in FWHM.
- Flat distribution in FWHM [C IV/Mg II].
- L_{1450} and FWHM simultaneously.

The reason for these tests is to check whether our findings are biased by the peaky distribution in L_{1450}, FWHM(C IV) and FWHM [C IV/Mg II] and/or the known correlation between L_{1450} and FWHM(C IV) that we observe in Fig. 3.3.1 (see also Appendix B.2). To this end, we first divided our SDSS samples in bins of 0.5dex in L_{1450} starting at log $L_{1450} = 45.0$ in the DR7Q sample and at log $L_{1450} = 44.5$ in the DR12Q sample. For FWHM(C IV) and FWHM [C IV/Mg II] we divided our sample in bins of 0.4dex. To guarantee an equal number of objects in each bin, we selected 23 objects from the DR7Q sample and 100 objects from the DR12Q sample. We finally subdivided our SDSS samples in bi-dimensional bins of L_{1450} and FWHM(C IV) of (0.5 and 0.4 dex respectively). For each bin we selected 13 and 30 objects in the DR7Q and DR12Q samples. We repeated these procedures 100 times to account for statistical variance because of the limited sampling. In all cases we find that the FWHM(C IV) associated correlations show larger or equivalent statistical significance than the FWHM [C IV/Mg II] correlations as suggested by the William's method (See Table 3.3 for details).

3.4 Discussion

C IV-based $M_{\rm BH}$ estimations are known to be problematic. In the past few years Runnoe et al. (2013), Mejía-Restrepo et al. (2016) and Coatman et al. (2017) provided alternative methods attempting to improve C IV-based masses. All these methods were based on correlations between different observables associated to the C IVemission and the ratio of FWHM(C IV) and the FWHM of low-ionization lines (i.e. Hα, Hβ and Mg II). In spite of the good quality of the data used in these works, all these methods were derived using small samples with limited coverage of the parameter space of the observables involved in each method. Using SDSS DR7Q and DR12Q samples (which in spite of their quality limitations are more representative of the quasar population) we showed that all these methods are of limited applicability to improve C IV-based $M_{\rm BH}$ estimations. In fact, we find that the aforementioned methods depend on correlations that are actually associated to the FWHM of the C IV profile itself and not to an interconnection between FWHM(C IV) and the FWHMs of the low ionization lines. Additionally, our analysis suggests that from all the correlations that we considered with FWHM(C IV), those that are associated to $L_{\rm peak}$ [C IV/1450Å] are the tightest ones. We also find that other quantities considered in this work ($L_{\rm peak}$ [C IV/SiOIV], $L_{\rm peak}$ [C IV/C III]], $\Delta V_{\rm peak}$ (C IV) and $\Delta V_{\rm line}$ (C IV)) are all tightly correlated with $L_{\rm peak}$ [C IV/1450Å] (see Table. B.2).

Further support comes from the principal component analysis (PCA) described in Appendix B.3. This analysis reveals that the first Eigenvector is mostly driven by the anti-correlation between FWHM(C IV) and $L_{\rm peak}\left[\rm C\,IV/1450\AA\right]$. This occurs in such a way that the relations between these quantities and FWHM [C IV/Mg II], L_{1450}, EW(C IV), $L_{\rm peak}$ [C IV/SiOIV], $L_{\rm peak}$ [C IV/C III]], $\Delta V_{\rm peak}$ (C IV) and $\Delta V_{\rm line}$ (C IV) are basically driven by the FWHM(C IV)-$L_{\rm peak}\left[\rm C\,IV/1450\AA\right]$ anti-correlation. Notably, the second Eigenvector is mostly driven by FWHM(Mg II) and shows no correlation with any C IV related quantity. This indicates that the formation of the Mg II and C IV profiles is independent from each other. In other words, there is no-possibility to relate the non-virialized C IV emission with the virialized Mg II emission.

A possible explanation for this could be associated to the fact that the more luminous a quasar is, the smaller its EW(C IV). This phenomenon is known as the Baldwin Effect in honour its discoverer Baskin & Laor (2004, 2005); Richards et al. (2011); Ge et al. (2016). Both, the quasar luminosity and EW(C IV), are known to be related with the C IV blue-shift, the C IV asymmetry, and the relative strength of the X-ray emission (Richards et al., 2011). Indeed, if we take $L_{\rm peak}\left[\rm C\,IV/1450\AA\right]$ as a proxy for the EW of C IV and consider the anti-correlation between FWHM(C IV) and L_{1450}, we can conclude that the very tight anti-correlation between FWHM(C IV) and $L_{\rm peak}\left[\rm C\,IV/1450\AA\right]$ can be seen as inherited from the Baldwin Effect.

The Baldwin Effect is believed to the be driven by the Eddington ratio that induces radiation driven winds into the BLR region that produces the C IV emission. In this scenario, as the Eddington ratio increases, the wind become stronger and increases the velocity of the outflowing C IV material (this velocity is directly related to the C IV blueshift). If this scenario is at play, our findings would suggest that winds would also induce larger FWHM(C IV).

Chapter 4

Nuclear gas distribution effect on the mass determination of distant supermassive black holes

The material presented in this chapter is extracted from Mejia-Restrepo et al 2017 submitted to Nature-Astronomy.

4.1 Introduction

Active Supermassive black holes (SMBHs) are powered by accretion flows, probably in the form of accretion discs (ADs) that convert gravitational energy into radiation (Shakura & Sunyaev, 1973). Gas in the Broad Line Region (BLR), located in the vicinity of the SMBH and moving at Keplerian velocities of thousands of kilometres per second, is photo-ionized by the AD producing broad emission lines. Under virial equilibrium, the observed full width at half maximum ($\mathrm{FWHM_{obs}}$) of these lines can be used as a proxy for the virial velocity (V_{BLR}) and M_{BH} can be expressed as:

$$M_{\mathrm{BH}} = G^{-1} R_{\mathrm{BLR}}\ V^2_{\mathrm{BLR}} = f\ G^{-1} R_{\mathrm{BLR}}\ \mathrm{FWHM}^2_{\mathrm{obs}} \tag{4.4.1}$$

Here, G is the gravitational constant, R_{BLR} is the mean BLR distance to the SMBH and f is the virial factor that accounts for the differences between the unknown V_{BLR} and $\mathrm{FWHM_{obs}}$ that are mostly caused by the BLR gas distribution of each object. Since even in the closest active galaxies the BLR cannot be resolved with current capabilities, R_{BLR} is estimated from reverberation mapping (RM) experiments that show a strong correlation between this distance and the continuum luminosity (the $R_{\mathrm{BLR}}-L$ relation) (Kaspi et al., 2000; Bentz et al., 2013). f is assumed to be constant for all systems and is usually determined by requiring RM-based masses (from Equation 4.4.1) to agree, on average, with masses estimated from the relation between M_{BH} and the stellar velocity

dispersion found in local galaxies (Onken et al., 2004; Graham, 2015; Woo et al., 2015). This indirect technique to determine $M_{\rm BH}$ is known as the "single epoch virial method" (Trakhtenbrot & Netzer, 2012; Shen, 2013).

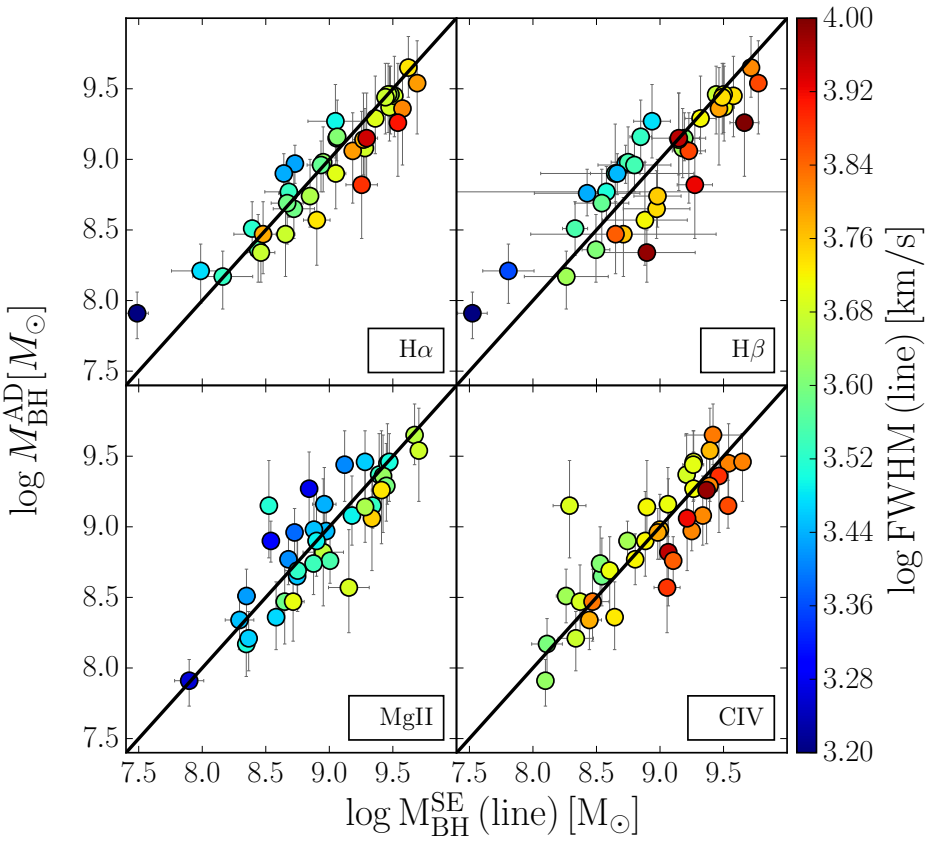

Figure 4.4.1: **Accretion-disk-derived Black Hole Mass versus Single Epoch Black Hole Masses**. The black solid line shows the 1:1 relation. The colour of the points scales with the $\rm FWHM_{obs}$ of the emission lines in each panel. The approaches yield masses in very good agreement with each other, albeit with a significant scatter. The scatter shows a strong gradient with $\rm FWHM_{obs}$, from small $\rm FWHM_{obs}$ (blue) above the 1:1 relation to large $\rm FWHM_{obs}$ (red) below.

Unfortunately, the virial method is subject to biases and uncertainties associated with our ignorance of the dependence of f on additional physical properties. These could include radiation pressure perturbations (Marconi et al., 2008; Netzer & Marziani, 2010), non virial velocity components (Denney et al., 2009b, 2010), the relative thickness ($H/R_{\rm BLR}$) of the Keplerian BLR orbital plane (Gaskell, 2009), and the line-of-sight inclination angle (i) (Wills & Browne, 1986; Shen & Ho, 2014; Runnoe et al., 2014) of this plane. An analytical expression for f in the case of a planar BLR of thickness $H/R_{\rm BLR}$ is given by:

$$f = \left[4\left(\sin^2 i + (H/R_{\rm BLR})^2\right)\right]^{-1} \tag{4.4.2}$$

where $\sin^2 i$ accounts for the line-of-sight projection of the Keplerian velocity of the BLR orbital plane (Collin et al., 2006; Decarli et al., 2008a). The nature of the velocity component responsible for the thickness of the BLR in unclear. However, ideas such as non-coplanar orbits, accretion disk pressure, induced turbulence and outflowing disc winds have been suggested in the literature as plausible mechanisms to puff up the BLR (Collin et al., 2006; Czerny et al., 2016). Given all these, the assumption of an universal f introduces an uncertainty in the single epoch method which is estimated to be at least a factor of 2-3.

Here we used an alternative method to estimate $M_{\rm BH}$ by fitting the AD spectra of 37 active galaxies at z$\sim$1.5 (about 1/3 of the current age of the universe), observed using the ESO X-Shooter spectrograph which provides simultaneous, very wide wavelength coverage of the AD emission (Capellupo et al., 2015, 2016) (see §4.3.1 in the Methods section for sample description). The spectra were fitted with standard, geometrically thin, optically thick AD models (Shakura & Sunyaev, 1973) including general relativistic and disc atmosphere corrections (Slone & Netzer, 2012). Each model is determined by several properties, mainly its $M_{\rm BH}$ ($M_{\rm BH}^{\rm AD}$), the normalized accretion rate (expressed as the Eddington ratio $\lambda_{\rm Edd} = L/L_{\rm Edd}$) and the black hole spin (a_*) (see §4.3.2.2 in the Methods section and Appendix C for model description). Because the method only relies on our ability to model the AD, the resulting $M_{\rm BH}^{\rm AD}$ are completely independent of the more uncertain BLR geometry and kinematics, and therefore of any assumptions on the f factor. In chapter 2 we estimated the associated single epoch black hole masses ($M_{\rm BH}^{\rm SE}$) of this sample from the Hα, Hβ, Mg II and C IV broad emission lines. This open the possibility to (1) compare both $M_{\rm BH}$ estimations and determine possible dependences of f in other observational properties and (2) infer the underlying distribution of the BLR gas.

4.2 Results and Discussion

$M_{\rm BH}$ determinations from the aforementioned methods are compared in Figure 4.4.1. The approaches yield masses in very good agreement with each other, albeit with significant scatter of a factor of about 2. We looked for possible drivers for this scatter and found a strong gradient in $\rm FWHM_{obs}$ across the relation, as can be seen by the colour gradient of the data points in Figure 4.4.1.

The ratio between $M_{\rm BH}^{\rm AD}$ and $M_{\rm BH}^{\rm SE}/f = G^{-1}R_{\rm BLR}{\rm FWHM}_{\rm obs}^2$ allows us to determine a proxy for the virial factor f which we define as:

$$f_{\rm AD}\,({\rm line}) \equiv M_{\rm BH}^{\rm AD} \,/\, \left(G^{-1}R_{\rm BLR}\ \left({\rm FWHM_{obs}\,(line)}\right)^2\right) \tag{4.4.3}$$

In Figure 4.4.2 we show $f_{\rm AD}\,({\rm line})$ as a function of the $\rm FWHM_{obs}$ for the Hα, Hβ, Mg II and C IV broad emission lines. Strong anti-correlations between $f_{\rm AD}$ and $\rm FWHM_{obs}$ are present for all lines. These correlations are found to be significantly stronger than the expected correlations between $f_{\rm AD}$ and $G^{-1}R_{\rm BLR}{\rm FWHM}_{\rm obs}^2$ (see Table 4.1 and see

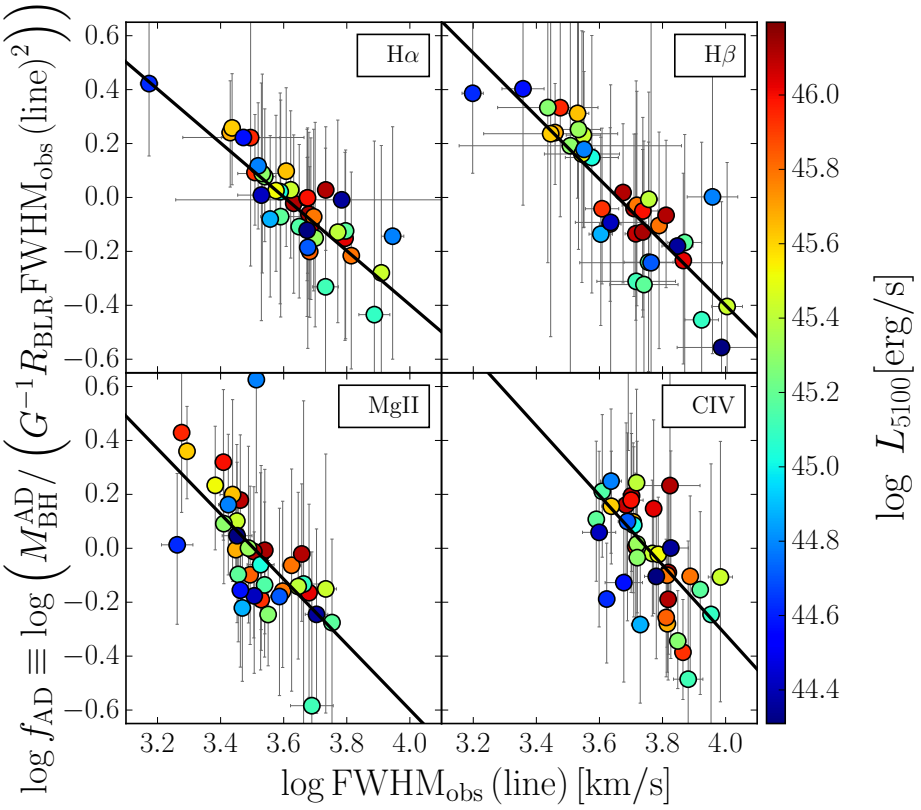

Figure 4.4.2: **Virial factor f as a function of FWHM$_{\rm obs}$ for the Hα, Hβ, Mg ii and C iv broad emission lines.** The black solid line is the best linear fit to the data. There is a clear anti-correlation between $f_{\rm AD}$ and FWHM$_{\rm obs}$ for all lines as suggested in Figure 4.4.1. The colour of the points scales with the measured monochromatic luminosity at 5100Å (L_{5100}) for each object, as indicated by the colour bar. Redder (bluer) points correspond to larger (smaller) values of L_{5100}. No clear gradient is seen in the scatter of these anti-correlations as a function of L_{5100}.

§4.3.3 in the Methods section for details). We can conclude that the $\mathrm{FWHM_{obs}}$ of the broad lines drives the discrepancies between $M_{\mathrm{BH}}^{\mathrm{AD}}$ and $M_{\mathrm{BH}}^{\mathrm{SE}}$.

We also determined how $M_{\mathrm{BH}}^{\mathrm{AD}}$ depends on $\mathrm{FWHM_{obs}}$ and L_λ (as described in §4.3.3 in the Method section). The dependence on $\mathrm{FWHM_{obs}}$ is close to linear and, therefore, very different from the expected squared dependency found in Equation 4.4.1. The dependence on the monochromatic luminosities is consistent, within errors, with that found for single epoch calibrations (i.e., $M_{\mathrm{BH}}^{\mathrm{AD}} \propto R_{\mathrm{BLR}}$). This indicates that L_λ has no impact on the scatter between $M_{\mathrm{BH}}^{\mathrm{SE}}$ and $M_{\mathrm{BH}}^{\mathrm{AD}}$ and that f can be expressed as a single function of the $\mathrm{FWHM_{obs}}$ of the broad emission lines. As can be seen in Table 4.1, our result are consistent within uncertainties with $f_{\mathrm{AD}} \propto \mathrm{FWHM_{obs}}^{-1}$ for all lines.

Table 4.1: ***The virial factor as a function of $FWHM_{\mathrm{obs}}$ for the broad emission lines.*** $\mathrm{FWHM^0_{obs}}$ *and* β *are best fit parameters found for* $f_{\mathrm{AD}} = \left(FWHM_{\mathrm{obs}}\,(line)\,/\mathrm{FWHM^0_{obs}}\right)^{\beta}$. r_{s} *and* P_{s} *are the Spearman correlation coefficient and associated null-hypothesis probability for the* f_{AD} *vs* $FWHM_{\mathrm{obs}}$ *(†) and* f_{AD} *vs* $G^{-1}R_{BLR}FWHM^2_{\mathrm{obs}}$ *(‡) correlations.*

			$\mathrm{FWHM_{obs}}$(†)		$G^{-1}R_{\mathrm{BLR}}\mathrm{FWHM^2_{obs}}$ (‡)	
Broad line	$\mathrm{FWHM^0_{obs}}\,[\mathrm{km\,s^{-1}}]$	β	r_{s}	P_{s}	r_{s}	P_{s}
Hα	4000±700	-1.00±0.10	-0.85	4×10^{-11}	-0.44	5×10^{-3}
Hβ	4550±1000	-1.17±0.11	-0.84	8×10^{-11}	-0.48	2×10^{-3}
Mg II λ2798	3200±800	-1.21±0.24	-0.75	9×10^{-8}	-0.23	2×10^{-1}
C IV λ1549	5650±3000	-1.29±0.35	-0.61	6×10^{-5}	-0.25	1×10^{-1}

Previous work attempted to derived f by comparing single epoch SMBH mass estimations with masses obtained using the scaling relations between the black hole mass and the luminosity (Decarli et al., 2008b) or stellar dispersion (Shen & Ho, 2014) of the host galaxy spheroidal components. The results of these works also exhibit an anti-correlation between f and the $\mathrm{FWHM_{obs}}$ of the broad emission lines and were understood as an effect of line of sight inclination of the BLR. However, these works applies the same prescription to all systems, assuming that all objects are well represented by the median trend of the scaling relations, and do not take into account the large intrinsic scatter in such relations. This is in sharp contrast with our sample where $M_{\mathrm{BH}}^{\mathrm{AD}}$ is independently obtained for each object through individual spectral fitting of the accretion disc emission.

The high quality spectra in our sample and the careful modelling of its broad emission lines allow us to explore in detail whether the line of sight inclination in a disc-like BLR can reproduce the observed trends. For this purpose we use the data and correlations determined from the Hα line because of its high signal-to-noise ratio (Mejía-Restrepo et al., 2016). We define $\mathrm{FWHM_{int}}$ as the *intrinsic* full width at half maximum of the virialized velocity component of the BLR. To recover the virial expectation $M_{\mathrm{BH}} \propto (\mathrm{FWHM_{int}})^2$ given by Equation 4.4.1 we use our result that $f \propto \mathrm{FWHM^{-1}_{obs}}$ for Hα (or equivalently $M_{\mathrm{BH}}^{\mathrm{AD}} \propto \mathrm{FWHM_{obs}}$) implying that, on aver-

age, $\mathrm{FWHM_{int}} \propto \mathrm{FWHM_{obs}^{1/2}}$. First, we adopt a model of a thin BLR (assuming that $H/R \to 0$ in Equation 4.4.2) and use Monte Carlo simulations to find the $\mathrm{FWHM_{int}}$ distribution that, after taking into account the line-of-sight inclination effects for randomly orientated BLRs, reproduces the cumulative FWHM(Hα) distribution (see §4.3.4 in the

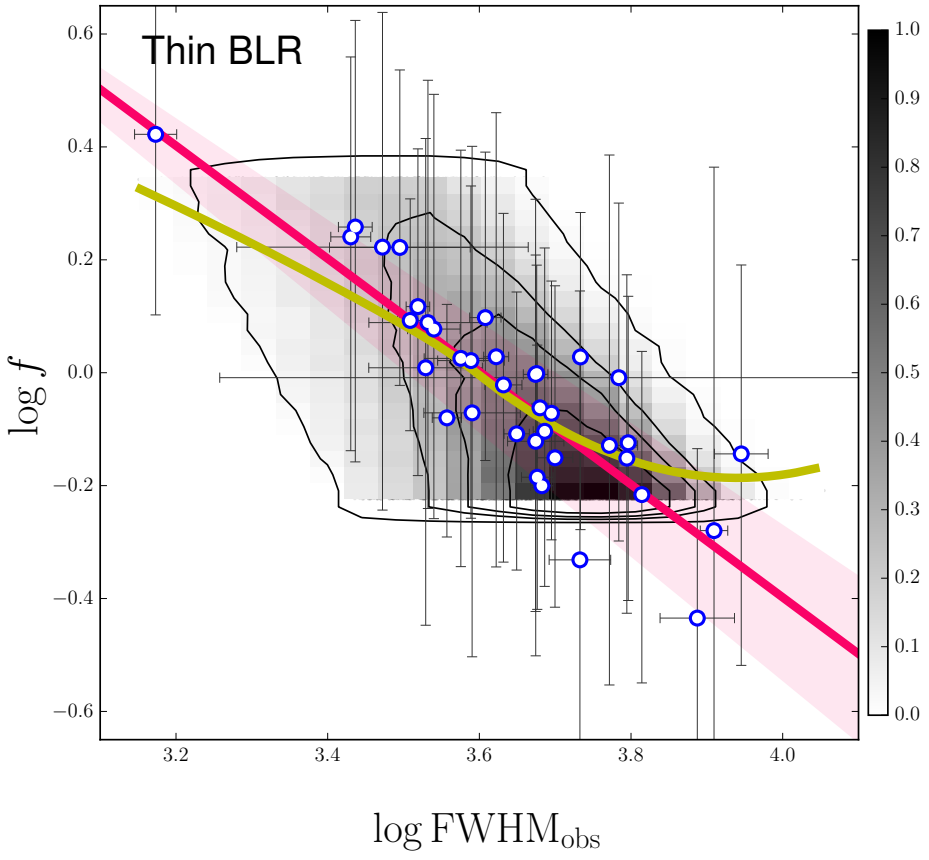

Figure 4.4.3: **Virial factor–$\mathrm{FWHM_{obs}}$ bi-dimensional distribution.** Predicted bi-dimensional probability distribution function of the virial factor versus $\mathrm{FWHM_{obs}}$ for a thin BLR ($H/R = 0$) modified by line-of-sight inclination is shown in gray. The darkest regions represent the most probable combinations of these quantities as quantified in the colour bar. The thin, black lines are the 25%, 50% and 75% and 99% confidence limit contours centred around the maximum probability point. The thick yellow line is the median of the f–$\mathrm{FWHM_{obs}}$ distribution derived from a quantile non-parametric spline regression. The open-blue circles are data taken from Figure 4.4.2 for the Hα line. The magenta thick line is the derived relation $f = \left(\mathrm{FWHM\,(H\alpha)}\,/4000\ \mathrm{km\,s^{-1}}\right)$ and the shadowed region the associated uncertainties. The yellow and magenta lines are in very good agreement within uncertainties. Additionally, the distribution of the data points shows a good agreement with the predicted bi-dimensional distribution confidence limits. Explicitly, we find 21% of the points inside the central 25% confidence level region, 51% inside the 50% confidence level region, 78% inside the 75% confidence level region and 87% inside the 99% confidence level region.

Methods section for details). Next, we generate a large population of objects drawn from the $\mathrm{FWHM_{int}}$ distribution and determine for each of these f and $\mathrm{FWHM_{obs}}$. Finally, we compare the bi-dimensional f–$\mathrm{FWHM_{obs}}$ distribution obtained from our observations with that generated from the simulations. We find that we are able to reproduce not only the mean trend of the observed correlation, but also the density distribution of data points, as can be seen in Figure 4.4.3. Furthermore, our simulations can recover the expected $\mathrm{FWHM_{int}} \propto \mathrm{FWHM_{obs}^{1/2}}$ correlation (see extended data Figure 4.4.7). These results strongly indicate that line-of-sight inclination effects cause the observed f–$\mathrm{FWHM_{obs}}$ anti-correlation.

We also considered the combined effect of inclination and BLR thickness by assuming an universal H/R within the range 0-1. We find that a wide range in thickness ratios ($H/R \lesssim 0.5$) can reproduce the cumulative distribution function of FWHM(Hα), but only relatively thin BLRs ($H/R \lesssim 0.1$) can reproduce the observed bi-dimensional distribution of f_{AD} and FWHM(Hα), and the predicted $\mathrm{FWHM_{int}} \propto \mathrm{FWHM_{obs}^{1/2}}$ dependence.

We have also examined possible alternative scenarios. In particular, the effects of radiation pressure force in a gravitationally bound BLR can predict $f \propto \mathrm{FWHM_{obs}^{-1}}$ for some configurations (Netzer & Marziani, 2010). This model predicts that the scatter in the relation will depend on the luminosity of the sources (see §4.3.5 in the Methods section). However, we do not find clear indications for this in our observations, as can be seen by the colour coded data points in Figure 4.4.2, where no clear gradient in L_{5100} is found across the f–$\mathrm{FWHM_{obs}}$ correlation. Note however that given the relatively narrow range in L_{5100} covered by our sample (a factor of 80), and the uncertainties in our estimations of f, radiation pressure remains a likely mechanism that should be explored further in the future (see Extended data figure 4.4.8).

In summary, our results favour the line-of-sight inclination as the best interpretation for the observed f–$\mathrm{FWHM_{obs}}$ correlation. As already discussed, this effect has been widely known to affect black hole mass measurements and is inherent to a flattened BLR geometry. At the same time, radiation pressure remains a viable mechanism and have been proven to affect high ionization emission lines, as it is the case of C IV, but there is no conclusive evidence for its effect in low ionization emission lines such as Hα, Hβ and Mg II(Mejía-Restrepo et al., 2016).

Regardless of its physical origin, the dependence of f with FWHM(Hα) implies that M_{BH} has been, on average, systematically overestimated for systems with large FWHM(Hα) ($\gtrsim 4000$ km s^{-1}) and underestimated for systems with small FWHM(Hα) ($\lesssim 4000$ km s^{-1}). The range of f_{AD} values presented in Figure 4.4.2, which are associated with FWHM(Hα)=1600-8000 km s^{-1}, imply a range in f, and hence M_{BH}, of factor $\sim$6. However, this range should not be taken as representative of the entire population of AGN since our sample is too small (37 objects) and was not defined to be complete in terms of BLR properties.

Even though our sample is selected at a specific epoch ($z \sim 1.5$), the physics of

a compact region such as the BLR is likely to remain constant over time. This has important implications for the study of active SMBHs at low and high redshifts. For example, the lowest $M_{\rm BH}$ sources at $z \sim 0$ typically show relatively narrow BLR profiles (1000 km s$^{-1}\lesssim$ FWHM(Hα) $\lesssim$ 2000 km s^{-1}). In this case, $M_{\rm BH}$ should be about 2-4 times larger than current estimates, and consequently $\lambda_{\rm Edd}$ should be smaller by the same factor. Another example is related to the mass of the most massive young known quasars found at $z \gtrsim 6$. Our proposed dependence of f with FWHM(Mg II) reduces the mass of the brightest known systems by up to a factor 2, as they typically show lines with FWHM(Mg II)$\geq$ 3200 km s^{-1}, somewhat alleviating the tension between their outstandingly large masses and the very early epochs at which they have been discovered (Mortlock et al., 2011; De Rosa et al., 2014; Wu et al., 2015).

4.3 Methods

4.3.1 Sample description

The sample we use in this letter consists of 39 type-I AGN selected to be within a narrow redshift range around $z \simeq 1.55$. For this sample we obtained high signal to noise (S/N) spectroscopic observations using the VLT/X-Shooter spectrograph. At the selected narrow redshift range, the X-Shooter spectrograph covers a wide range from ∼1200 Å to ∼9200 Å in the rest-frame. The sample was selected to homogeneously map the parameter space of $M_{\rm BH}$ and $\lambda_{\rm Edd} = L/L_{\rm Edd}$ within the sampled region. The initial values of these quantities were obtained from single-epoch (SE) calibrations (Trakhtenbrot & Netzer, 2012) of the Hα broad emission line and its adjacent continuum.

The broad spectral coverage and the high S/N in our sample allowed us to (1) recalibrate, compare and test the performance of the different SE $M_{\rm BH}$ estimators using Hα, Hβ, Mg II and C IV(Mejía-Restrepo et al., 2016); and (2) model and confidently constrain the observed Spectral Energy Distributions (SEDs) in 37 out of 39 objects using standard thin accretion disc models (Capellupo et al., 2015, 2016). The output of the SED fitting provided alternative estimations for $M_{\rm BH}$, $\dot{M}$, $\lambda_{\rm Edd}$ and a realistic estimate of a_*. For the sake of simplicity, hereafter when referring to paper I, II and III we will be citing references 22, 26 and 23, respectively.

4.3.2 Estimating $M_{\rm BH}$

In this section we briefly describe the two alternative approaches that we followed to derive $M_{\rm BH}$ and comment on the sources of uncertainties of each method.

4.3.2.1 Single Epoch $M_{\rm BH}$ estimates

We used new calibrations of the single epoch (SE) black hole mass estimators for the broad $H\alpha$, $H\beta$, MgII and CIV emission lines. In particular, we used the coefficients of the first two columns of Table 7 in Paper II. The underlying assumption in SE estimations is that Equation4.4.1 holds for all broad emission lines and $V_{\rm BLR}$ can be estimated from the $\rm FWHM_{obs}$ of the line in question using Equation 4.4.1. We used $f = 1$ as suggested from $M_{\rm BH}$-Stellar dispersion calibrations (Woo et al., 2015). $R_{\rm BLR}$ is obtained from the calibration of the $R_{\rm BLR} - L$ relation obtained from various RM studies (Kaspi et al., 2000, 2005; Bentz et al., 2009, 2013) which can be written as:

$$R_{\rm BLR} = R^0_{\rm BLR} \left(\frac{L_\lambda}{10^{44} {\rm erg\,s^{-1}}} \right)^{\alpha_{\rm line}} \tag{4.4.4}$$

where, $R^0_{\rm BLR}$ is the normalization constant which for the case of the Hβ line, and for $\lambda = 5100$Å, is 538 light-days (Mejía-Restrepo et al., 2016).

As we briefly discussed in the letter, the simple SE mass determination method is limited in various important ways:

1. The $R_{\rm BLR} - L$ relation has been obtained from a relatively small sample of low-z ($z \lesssim 0.3$) Seyfert I galaxies and low luminosity quasars ($L_{5100} \lesssim 10^{46} {\rm erg\,s^{-1}}$, where $L_{5100} \equiv 5100\text{Å} \times L\left(5100\text{Å}\right)$). Therefore, extrapolation of the $R_{\rm BLR} - L_{5100}$ relation is needed to estimate $M_{\rm BH}$ in high luminosity objects at high-z. Moreover, the intrinsic scatter in the $R_{\rm BLR} - L_{5100}$ relation is affected by intrinsic luminosity variations as well as by the disc inclination to the line-of-sight (Davis & Laor, 2011; Netzer & Trakhtenbrot, 2014; Capellupo et al., 2015).

2. The re-calibration of the Hβ-based single epoch method to other broad emission lines like Hα, Mg II λ2798 and C IV λ1549 induces intrinsic dispersion that can be as high as 0.5 dex for the C IV λ1549 line (Mejía-Restrepo et al., 2016).

3. The dependence of f on inclination is a major source of uncertainty. This has been explored in numerous papers. A recent paper used a sample of about 600 local SDSS type1-AGN to compare the $M_{\rm BH}$ estimations derived from the $M_{\rm BH}$-stellar dispersion relation ($M^{\sigma_\star}_{\rm BH}$) with those derived from the single epoch method (Shen & Ho, 2014). They found that $f_{\sigma\star} \equiv M^{\sigma_\star}_{\rm BH}/(G^{-1} R_{\rm BLR} {\rm FWHM\,(H}\beta)^2)$ is anti-correlated with FWHM(Hβ), and argued that this is a manifestation of the line-of-sight inclination in a flat, disc-like BLR. Earlier works also suggested an anti-correlation between the radio loudness of sources and the observed FWHM(Hβ)(Wills & Browne, 1986; Runnoe et al., 2014). Assuming that radio jets in AGN are aligned with the axis of symmetry of the BLR and that the flat BLR is aligned with the disc, their results strongly suggests that the BLR in radio-loud AGN are considerably flattened.

4. There are questions regarding the validity of virial equilibrium of the BLR material. Earlier results about AGN with multiple emission measurements (i.e., NGC3783, NGC5548, NGC7469 and 3C390.3) show that the velocity radial profiles that are in good agreement with the expectations for a Keplerian system (Peterson & Wandel, 2000; Onken & Peterson, 2002) (i.e., $V_{\rm BLR}(r) \propto r^{-1/2}$). Additionally, in some velocity resolved RM experiments, the blue wing of the Hβ line has been observed to lag behind the red wing, which generally rules out significant outflow of both high- and low-ionization lines (Done & Krolik, 1996; Ulrich & Horne, 1996; Sergeev et al., 1999). However, more recent RM observations revealed diverse kinematics of the BLR including inflows, outflows and virialized gas (Denney et al., 2009b, 2010).

5. The use of a single value of f for measuring $M_{\rm BH}$ in sources that are not part of RM samples introduces an additional uncertainty which results from the fact that the FWHM$_{\rm obs}$ measured from single-epoch spectra are systematically larger than those measured from the RMS profiles during a RM campaign (Collin et al., 2006). This can be easily verified by comparing the RMS FWHM(Hβ) (Bentz & Katz, 2015) with the one measured from the mean spectrum of the same sources (Du et al., 2015). This is also true when the standard deviation of the lines ($\sigma_{\rm obs}$) is used instead of the FWHM$_{\rm obs}$ and has not been taken into account, properly, in many studies. For example, from the results published in a recent paper (Batiste et al., 2017)we obtain FWHM$_{\rm mean}$/FWHM$_{\rm rms} = 1.17^{+0.37}_{0.15}$.

6. The line shape parameter FWHM$_{\rm obs}/\sigma_{\rm obs}$ provides information on the structure and kinematics of the BLR. For instance, FWHM$_{\rm obs}/\sigma_{\rm obs} \sim 3.4$ is found for a spherical shell of clouds moving with fix a velocity and random orientations, FWHM$_{\rm obs}/\sigma_{\rm obs} \sim 3$ is found for an face-on rotating ring with fixed velocity, FWHM$_{\rm obs}/\sigma_{\rm obs} = 2.35$ corresponds to Gaussian profiles, FWHM$_{\rm obs}/\sigma_{\rm obs} \sim 2$ is found for a face on rotating Keplerian disc, FWHM$_{\rm obs}/\sigma_{\rm obs} \sim 1$ ($\rightarrow 0$) corresponds to Lorentzian profiles due, for example, to turbulent motions, as well as logarithmic profiles which can be caused by in-/outflow motions, and FWHM$_{\rm obs}/\sigma_{\rm obs} \sim 0.98$ corresponds to exponential profiles caused by electron scattering within the photo-ionized BLR gas (Kollatschny & Zetzl, 2013). It is known that FWHM$_{\rm obs}/\sigma_{\rm obs}$ vary within a significant range (Collin et al., 2006; Kollatschny & Zetzl, 2011; Peterson et al., 2004) suggesting that BLR profiles are not universal and that the virial factor is far from being a constant value.

4.3.2.2 Black Hole Mass Estimates from SED fitting

As previously mentioned, in papers I and III we recently implemented an alternative method to estimate the black hole mass in type1-AGN based on the fitting of the SED of the accretion discs, using a geometrically thin, optically thick accretion disc model, and obtained successful fits in 37 out of 39 objects in our sample. The model is fully determined by $M_{\rm BH}^{\rm AD}$, a_*, $\dot{M}$, the AD inclination with respect to the line-of-sight ($i_{\rm LOS}$),

and intrinsic $A_{\rm V}$. The procedure consisted of a Bayesian minimization over a grid of models covering a range in values for these parameters. We assumed Gaussian priors for $M_{\rm BH}^{\rm SE}\,({\rm H}\alpha, L_{6200})$ and $\dot{M}_{\rm SE}$. Means were given by the single-epoch estimations for each object and standard deviations of 0.3 and 0.2 dex were adopted, respectively. $M_{\rm BH}^{\rm SE}\,({\rm H}\alpha, L_{6200})$ and $\dot{M}_{\rm SE}$ were calculated assuming a virial factor $f_{\rm FWHM_{obs}} = 1$. Flat priors were assumed for the remaining model parameters. The role of the priors is to penalize models which deviate significantly from the observational estimations of $M_{\rm BH}\,({\rm H}\alpha)$ and $\dot{M}_{\rm SE}$, but allow a symmetric parameter search on either side of the means. (See appendix C for details about the model and Bayesian procedure)

We have investigated the possibility that our initial choices of $f_{\rm FWHM_{obs}}$ and the standard deviation in $M_{\rm BH}^{\rm SE}\,({\rm H}\alpha, L_{6200})$ ($\sigma_{M_{\rm BH}}$), affect the resulting $M_{\rm BH}^{\rm AD}$. As shown in Figure 4.4.4, this is not the case. In this Figure, we compare the resulting $M_{\rm BH}^{\rm AD}$ for a large range of initial guesses in f and $\sigma_{M_{\rm BH}}$ with the original $M_{\rm BH}^{\rm AD}$ values obtained for our sample in paper III (where $f_{\rm FWHM_{obs}} = 1$ and $\sigma_{M_{\rm BH}} = 0.3$ were assumed). We find that for large enough $\sigma_{M_{\rm BH}}$ ($\gtrsim 0.8$ dex) there is basically no difference between the $M_{\rm BH}^{\rm AD}$ values obtained with our initial choices and those $M_{\rm BH}^{\rm AD}$ values obtained with an initial f varying over a large range (0.4-2.5).

We also tested the reliability of the $f_{\rm AD}$ anti-correlation with $\rm FWHM_{obs}$ found using our Bayesian algorithm. We explored whether the assumption of flat priors for $i_{\rm LOS}$ and $A_{\rm V}$ had an impact on our results. We tested various Gaussian priors on $\cos i_{\rm LOS}$ assuming as central values some randomly assigned numbers and different intrinsic scatters of 0.1, 0.2 and 0.3 dex. We also assumed Gaussian priors on $A_{\rm V}$. The central values were obtained from the recent calibrations of $A_{\rm V}$ based on the $L({\rm H}\alpha)/L({\rm H}\beta)$ ratio (Baron et al., 2016). The intrinsic scatter were varied from 0.1 to 0.3 dex. In all cases we recover the anti-correlation between $\log f_{\rm AD}$ and the $\rm FWHM_{obs}$ for the Balmer lines with similar statistical significance. We also used $M_{\rm BH}^{\rm SE}\,({\rm C\,IV}, L_{1450})$ as the central value for the $M_{\rm BH}$ prior and tested using the median values, instead of the mean, for $M_{\rm BH}$ and $\dot{M}$. In both cases we recover the aforementioned anti-correlation with similar statistical significance. We conclude that our findings are not an artefact of the fitting code.

One important drawback from our modelling is a large degeneracy between the accretion rate and the inclination angle of the disc. For a given flux, larger inclinations will return larger intrinsic luminosities which in turn will return larger accretion rates. Fortunately, the derived black hole mass does not strongly depend on either inclination nor accretion rate and the mass estimates are consistent within 0.1 dex regardless of the final derived inclinations and accretion rates. As a consequence, the derived disc inclinations are very uncertain and are *not* good indicators of the real inclinations of the disc and consequently of the flat BLRs. Therefore, these values are not used as proxies for the inclination of the BLR and the determination of the virial factor.

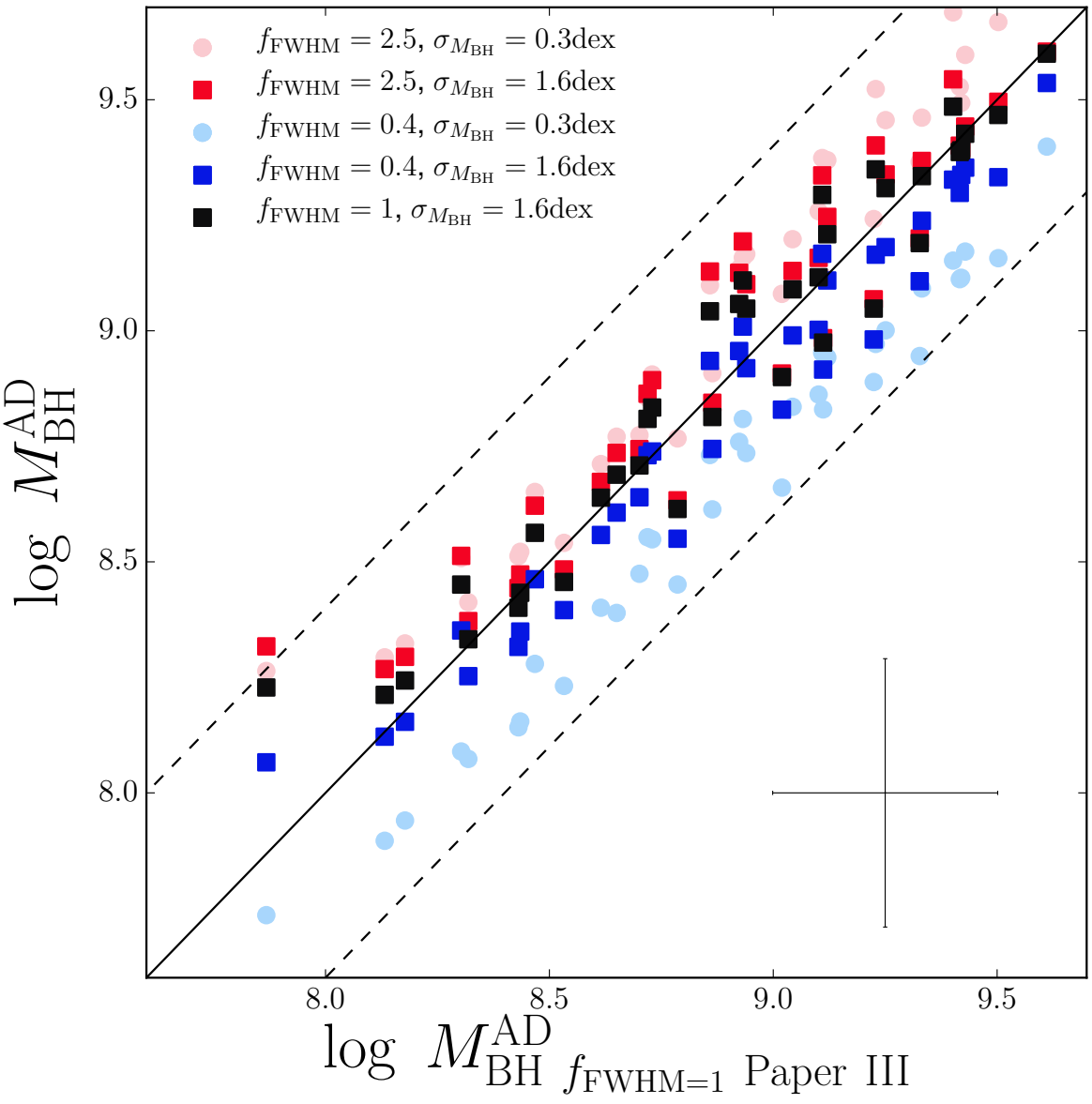

Figure 4.4.4: **Dependency of $M_{\rm BH}^{\rm AD}$ on the adopted values of f and $\sigma_{M_{\rm BH}}$.** Original $M_{\rm BH}^{\rm AD}$ values (from Paper III) vs Recalculated $M_{\rm BH}^{\rm AD}$ values obtained using different values for $f_{\rm FWHM}$ and the scatter in $M_{\rm BH}$ ($\sigma_{M_{\rm BH}}$, as shown in the legend). The solid line represents the 1:1 relation and the dashed lines represent $f = 0.4$ and $f = 2.5$. As $\sigma_{M_{\rm BH}}$ increases $M_{\rm BH}^{\rm AD}$ values get closer to the 1:1 relation (with just one exception at the lowest mass). This indicates that $f = 1$ is an appropriate initial choice. The cross symbol in the bottom right corner represents a typical error bars in our $M_{\rm BH}^{\rm AD}$ estimations.

4.3.3 f as a function of line width

In Table 4.1 we present the correlation coefficients of the $f_{\rm AD}$–FWHM$_{\rm obs}$ and $f_{\rm AD}$–$R_{\rm BLR}$FWHM$^2_{\rm obs}/G$ correlations for all the broad emission lines considered here. In all cases we find that the correlations associated with the FWHM$_{\rm obs}$ are stronger than those associated with $R_{\rm BLR}$FWHM$^2_{\rm obs}/G$. This suggests that the FWHM$_{\rm obs}$ correlations are not inherited from the definition of $f_{\rm AD}$. In order to prove this we conducted the Williams's Test (Dunn & Clark, 1969). Given a sample size, this test computes the statistical significance of the difference between the correlation coefficients of two correlations that have one variable in common. In this case the two dependent correlations are $f_{\rm AD}$–FWHM$_{\rm obs}$ and $f_{\rm AD}$–$R_{\rm BLR}$FWHM$^2_{\rm obs}/G$, while the common variable is $f_{\rm AD}$. Our results indicate very different correlation coefficients for the $f_{\rm AD}$–FWHM$_{\rm obs}$ and the $f_{\rm AD}$–$R_{\rm BLR}$FWHM$^2_{\rm obs}/G$ correlations (see Table 4.1), with a 5-σ significance for the Hα line, 4-σ significance for the Hβ and the Mg II λ2798 lines and a 3-σ significance for the C IV λ1549 line. This confirms that the correlations associated with the FWHM$_{\rm obs}$ of the broad emission lines are indeed much stronger than those that by definition are associated with $R_{\rm BLR}$FWHM$^2_{\rm obs}/G$.

Single epoch $M_{\rm BH}$ can also be estimated using $\sigma_{\rm obs}$ instead of FWHM$_{\rm obs}$. Obviously, in that case the virial factor has a different numerical value since FWHM can be significantly different from $\sigma_{\rm obs}$ (e.g., for a Gaussian line profile FWHM$_{\rm obs}$ = 2.35 $\sigma_{\rm obs}$). We tested whether the associated $f_{\rm AD}\left(\sigma_{\rm obs}\right) \equiv M^{\rm AD}_{\rm BH}\ /\left(G^{-1}R_{\rm BLR}\ \sigma^2_{\rm obs}\right)$ is also anti-correlated with $\sigma_{\rm obs}$ and confirmed statically significant anti-correlations using all four emission lines. However, in this case there is no statistical difference between the $f_{\rm AD}$–$\sigma_{\rm obs}$ and $f_{\rm AD}$–$R_{\rm BLR}\sigma^2_{\rm obs}/G$ correlations. This is most likely due to the larger uncertainties associated with the measurement of $\sigma_{\rm obs}$ in our sample (Mejía-Restrepo et al., 2016).

To determine how $M^{\rm AD}_{\rm BH}$ depends on the FWHM$_{\rm obs}$ of the lines and the associated L_λ used in single epoch mass determinations methods, we used the following expression:

$$\log M^{\rm AD}_{\rm BH}\left({\rm FWHM}, L_\lambda\right) \equiv \alpha_{\rm AD}\log\left(L_\lambda\right) + E\log{\rm FWHM\,(line)} + F \tag{4.4.5}$$

and implemented an ordinary bi-variate least square linear regression to determine the coefficients in the equation. We summarize the results in Table 4.2, where we also show $\alpha_{\rm line}$, which represents the slope of the power-law coefficient of L_λ in Equation 4.4.4. We also list the scatter between $M^{\rm AD}_{\rm BH}$ and $M^{\rm SE}_{\rm BH}\left({\rm FWHM}, L_\lambda\right)$ as well as the scatter between $M^{\rm AD}_{\rm BH}$ and the *corrected* $M^{\rm SE}_{\rm BH}\left({\rm FWHM}, L_\lambda\right)$ ($M^{\rm SE}_{\rm BH}({\rm corr}) \equiv {\rm M}^{\rm AD}_{\rm BH}\left({\rm FWHM}, {\rm L}_\lambda\right)$) after the dependency of $f_{\rm AD}$ on FWHM$_{\rm obs}$ is taken into account. In the case of the Balmer lines, the scatter is reduced by about a factor 2. Thus, correcting for the correlation between $\log f_{\rm AD}$ and the FWHM$_{\rm obs}$ of the Balmer lines provides an important improvement in our $M_{\rm BH}$ estimations.

The results of the linear regressions presented in Table 4.2 highlight two important findings. First, $\alpha_{\rm AD}$ and $\alpha_{\rm line}$ are basically indistinguishable from each other. This indicates that L_λ has almost no impact in the deviation of $M^{\rm SE}_{\rm BH}\left({\rm FWHM}, L_\lambda\right)$ from

Table 4.2: *Properties of different correlations found for the emission lines of interest. Column [1]: power-law coefficient from reverberation mapping experiments (see Equation 4.4.4). Columns [2]-[4]: best fit parameters for linear regressions of the expression* $\log M_{\rm BH}^{\rm AD}\,(FWHM, L_\lambda) = \alpha_{\rm AD}\log(L_\lambda) + E\log{\rm FWHM\,(line)} + F$*. Column [5]:* R^2 *values of the linear regressions. Columns [6] and [7]: scatter in the* $M_{\rm BH}^{\rm AD}$ *vs* $M_{\rm BH}^{\rm SE}\,(FWHM, L_\lambda)$ *and* $M_{\rm BH}^{\rm AD}$ *vs* $M_{\rm BH}^{\rm SE}$(corr) *correlations.*

	$\alpha_{\rm line}$	$\alpha_{\rm AD}$	E	F	R^2	$M_{\rm BH}^{\rm AD}$ vs $M_{\rm BH}^{\rm SE}$	$M_{\rm BH}^{\rm AD}$ vs $M_{\rm BH}^{\rm SE}$(corr)
	[1]	[2]	[3]	[4]	[5]	[6]	[7]
Hα	0.63	0.66±0.03	1.00±0.10	7.42±0.07	0.948	0.17	0.09
Hβ	0.65	0.69±0.04	0.82±0.11	7.43±0.09	0.943	0.24	0.12
MgII	0.61	0.68±0.05	0.78±0.24	7.40±0.15	0.850	0.22	0.16
CIV	0.60	0.61±0.06	0.69±0.36	7.29±0.27	0.770	0.24	0.20

$M_{\rm BH}^{\rm AD}$ and that $M_{\rm BH}^{\rm AD}$ preserves its dependency on $R_{\rm BLR}$. Second, the dependence of $M_{\rm BH}^{\rm AD}$ on the observed ${\rm FWHM_{obs}}$ of the Balmer lines is close to linear rather than quadratic, as expected from the virial relation.

4.3.4 Inclination as the source of the f–$\rm FWHM_{obs}$ correlation

In this section we present different tests that we carried out to determine whether inclination is driving the correlation between f and ${\rm FWHM_{obs}}$.

Hereafter when referring to $\log f_{\rm AD}$, $M_{\rm BH}^{\rm SE}\,({\rm FWHM}, L_\lambda)$ and ${\rm FWHM_{obs}}$ we mean $\log f_{\rm AD}\,({\rm H}\alpha)$, $M_{\rm BH}^{\rm SE}\,({\rm FWHM\,(H}\alpha))$ and the observed value of FWHM(Hα), unless otherwise specified. The reason to select the Hα line instead of the Hβ line for the following analysis is the better S/N and hence more accurate measurements of FWHM(Hα) in our sample. As shown in earlier works, ${\rm FWHM_{obs}}$ in both Balmer lines are the same within uncertainties (Greene & Ho, 2005; Mejía-Restrepo et al., 2016).

The anti-correlation between $\log f_{\rm AD}$ and ${\rm FWHM_{obs}}$ could be explained by the inclination of the axis of symmetry of a disc-like BLR with respect to the line-of-sight (LOS). If we consider the median LOS inclination, $i_{\rm median}$, at which Type-1 AGN are typically observed, we can also define a median virial factor $f_{\rm median}$ at which the SE $M_{\rm BH}$ calibration represents an accurate black hole mass for objects observed at $i_{\rm median}$. Objects with narrower than usual broad emission lines are more likely observed at $i < i_{\rm median}$ (face-on orientations) and objects with broader than usual emission are more likely observed at $i > i_{\rm median}$ (edge-on orientations). This will produce too large (too small) SE mass estimates for objects with very broad (very narrow) emission lines, and would translate into a virial factor that anti-correlates with the line FWHMs.

The inclination hypothesis is also consistent with recent work that found that $f_{\sigma^\star} \equiv M_{\rm BH}^{\sigma^\star}/(G^{-1}R_{\rm BLR}{\rm FWHM\,(H}\beta)^2)$ is anti-correlated with FWHM(Hβ)(Shen & Ho, 2014). Here, $M_{\rm BH}^{\sigma^\star}$ is the black hole mass obtained from the correlation between $M_{\rm BH}$ and the

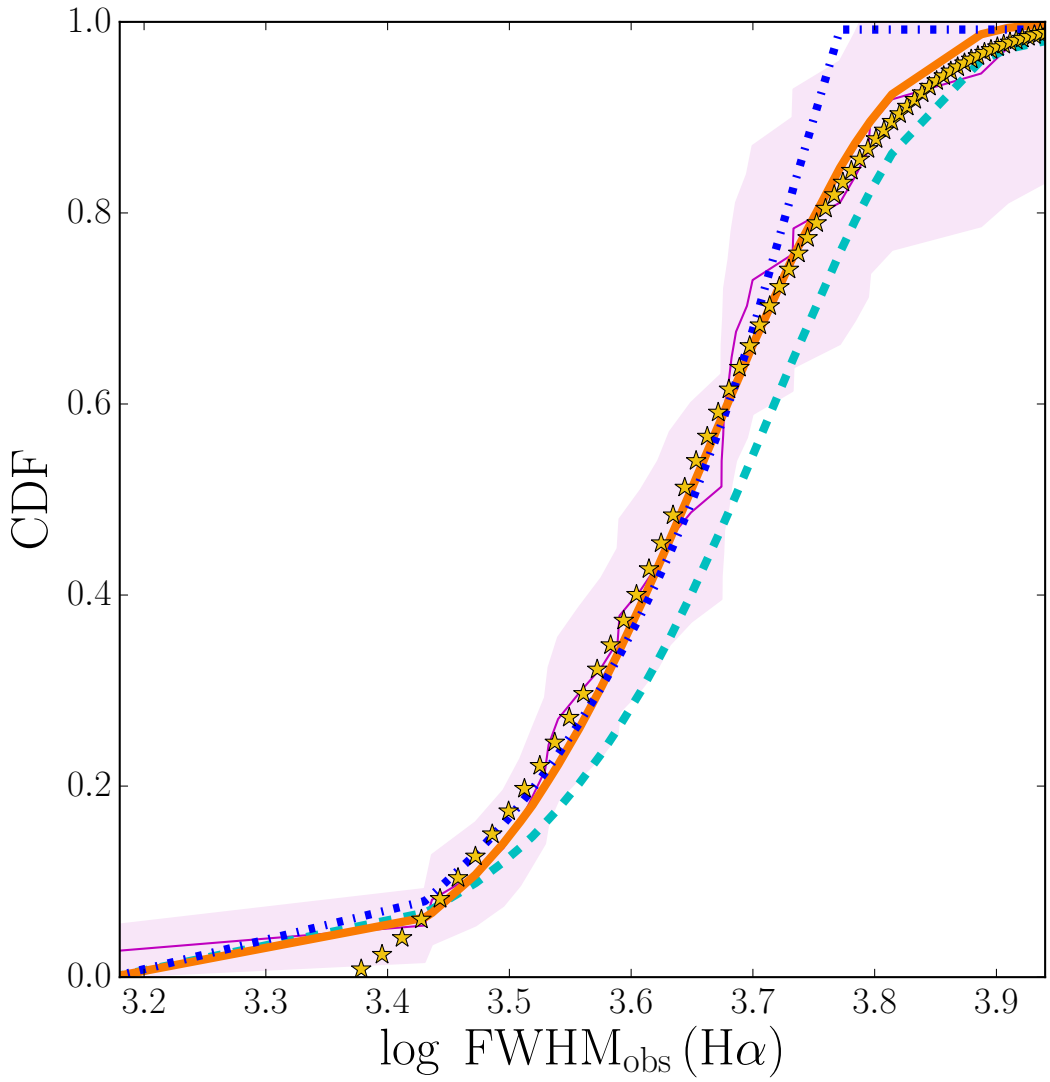

Figure 4.4.5: **Cumulative distribution functions for the observed and simulated FWHM$_{\rm obs}$ for Hα.** The cumulative distribution function (CDF) of FWHM(Hα) is the thin magenta line. The magenta shadowed region shows the Poissonian uncertainties. The thick orange line and yellow stars are the disc CDF for a thin ($H/R = 0$) and thick ($H/R = 0.5$) BLR, respectively. In both cases we assumed a truncated Gaussian distribution for the intrinsic FWHM(Hα) convolved with a $\sin i$ distribution. The cyan dashed line is a Gaussian distribution with no truncation. The dark blue dashed line is the CDF for FWHM$_{\rm int} = 8170 {\rm km\,s^{-1}}$ and FWHM$_{\rm std} = 0$, as modelled in other works (McLure & Dunlop, 2001; Decarli et al., 2008a). We observe that the modelled CDFs are generally in good agreement with the observed CDF for the thin and thick BLR models, but the thick BLR fails to reproduce the observed CDF at small FWHM(Hα) values.

stellar dispersion of the spheroidal component in galaxies. Analogously, an earlier work compared the virial black hole masses with black hole mass estimations obtained from

the relation between black hole mass and the luminosity of the host-galaxy spheroidal component (Decarli et al., 2008b). Their results also show a clear anti-correlation between f and the $\mathrm{FWHM_{obs}}$ of the broad emission lines that is interpreted by the authors as a BLR line-of-sight inclination bias.

There is further evidence that favors the hypothesis that LOS inclination is biasing SE M_{BH} estimations. As already pointed out, previous works found that the FWHM(Hβ) is significantly anti-correlated with radio core dominance in radio-loud quasars (Wills & Browne, 1986; Runnoe et al., 2014). This is consistent with Hβ emitting gas in a flattened configuration. In this scenario core-dominated objects (with their radio emission being Doppler-boosted along the LOS) correspond to face-on discs that typically show narrow Hβ profiles, while lobe-dominated objects (lacking Doppler-boosting) correspond to edge-on discs, that typically show broad Hβ profiles. In this scenario, the BLR is flat and the general plane of motion is similar to the plane of rotation of the central disc. In addition to this, there is accumulated evidence in the literature favouring a disc-like geometry for the BLR (McLure & Dunlop, 2001, 2002; Laor et al., 2006; Decarli et al., 2008a; Pancoast et al., 2014).

For a disc-like BLR with a thickness ratio H/R and inclination i with respect to the line-of-sight we will have $\mathrm{FWHM_{obs}} = \mathrm{FWHM_{int}} \times \sqrt{\sin^2(i) + (H/R)^2}$. Thus, for an ensemble of randomly orientated BLRs the final distribution of $\mathrm{FWHM_{obs}}$ will depend on (1) the intrinsic $\mathrm{FWHM_{int}}$ distribution and (2) the range of possible random orientations at which the BLR can be observed, both of which are, a priori, not known.

To check the inclination hypothesis we first need to determine the distribution of $\mathrm{FWHM_{int}}$ that is consistent with the probability density distribution (PDF) of the observed $\mathrm{FWHM_{obs}}$. We then need to test whether it is possible to recover the anti-correlation of f with $\mathrm{FWHM_{obs}}$ and the linear dependence of M_{BH} on $\mathrm{FWHM_{obs}}$, as derived in this letter. In other words, we need to test whether a population of randomly generated inclinations and $\mathrm{FWHM_{int}}$ that satisfy the PDF of $\mathrm{FWHM_{obs}}$, can also account for:

$$f \propto \mathrm{FWHM_{obs}^{-1}} \tag{4.4.6}$$

and at the same time:

$$\mathrm{FWHM_{int}} \propto \mathrm{FWHM_{obs}^{1/2}} \tag{4.4.7}$$

It is important to note that both predictions should be satisfied to guarantee inclination as the driving mechanism of the observed correlation between f and $\mathrm{FWHM_{obs}}$. The reason for this is that each of these expressions tests the dependency between $\mathrm{FWHM_{obs}}$ and the two independent distributions determined to reproduce $\mathrm{FWHM_{obs}}$: $\sin(i)$ and $\mathrm{FWHM_{int}}$. While Equation (5) tests the dependency between $\mathrm{FWHM_{obs}}$ and $\sin^{-2}(i)$ (which is proportional to f), Equation (6) tests the dependency between $\mathrm{FWHM_{obs}}$ and $\mathrm{FWHM_{int}}$.

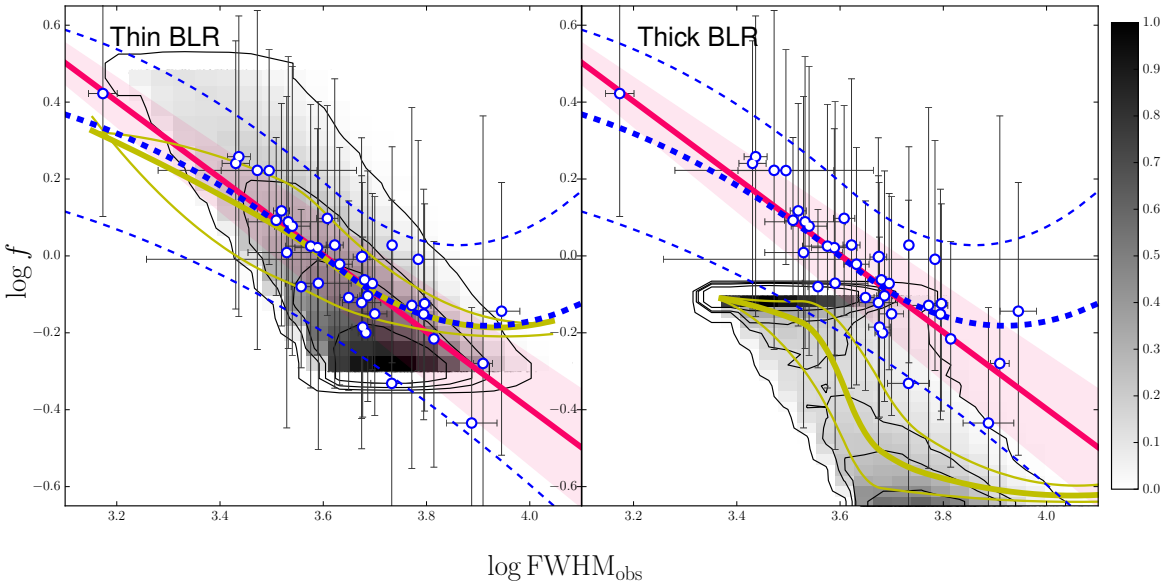

Figure 4.4.6: **Virial factor–$\mathrm{FWHM_{obs}}$ bi–dimensional distributions for a thin and thick BLR.** Predicted bi-dimensional probability distribution functions of the virial factor and $\mathrm{FWHM_{obs}}$ for a thin BLR (left) and a thick BLR (right), as predicted by the best-fit models shown in Figure 4.4.5 are shown in gray. The darkest regions represent the most probable combinations of these quantities as quantified in the colour-bar. The thin black lines are the 25%, 50% and 75% and 99% confidence limit contours centred around the maximum probability point. The thick yellow lines are the median of the f–$\mathrm{FWHM_{obs}}$ distributions derived from a quantile non-parametric spline regression. The open-blue circles are data from Figure4.4.2 for the Hα line. The magenta lines are the derived relation $f = \left(\mathrm{FWHM\,(H\alpha)}\,/4000\ \mathrm{km\,s^{-1}}\right)$ and the shadowed regions the associated uncertainties. The thin blue-dashed lines are the 25%, 50% and 75% quantiles of the observational distribution after accounting for the measurement errors in f_{AD} and FWHM(Hα). We see that for the thin BLR the 50%-quantile (median) of the theoretical and observational distributions are in very good agreement with each other. Additionally, the distribution of the data points shows good agreement with the predicted bi-dimensional distribution confidence limits. Explicitly, we find that 21% of the points fall inside the central 25% confidence level region, 51% fall inside the 50% confidence level region, 78% fall inside the 75% confidence level region, and 87% fall inside the 99% confidence region level. On the other hand, the thick BLR model cannot reproduce the bi-dimensional f–$\mathrm{FWHM_{obs}}$ distribution.

We first assumed a thin BLR by taking $H/R = 0$. We computed the PDF as the product of two independent random variables (Glen et al., 2004) and applied it to the special case where $\mathrm{FWHM_{obs}} = \mathrm{FWHM_{int}} \times \sin(i)$ (Lopez & Jenkins, 2012). For the $\mathrm{FWHM_{int}}$ distribution, we assumed an underlying truncated normal distribution with certain mean ($\mathrm{FWHM_{mean}}$) and dispersion ($\mathrm{FWHM_{std}}$). Our normal distribution was truncated to allow $\mathrm{FWHM_{int}}$ to vary between 1000 and 30000 $\mathrm{km\,s^{-1}}$. We also assumed that our sample is limited to objects with line-of-sight inclination angles between $i_{\mathrm{min}} =$

0° and $i_{\rm max} = 70^\circ$, with $i_{\rm max}$ determined by the torus opening angle. For an optimal exploration of the parameter space we ran a Monte Carlo Markov Chain simulation using the python code EMCEE (Foreman-Mackey et al., 2013). For the simulation we used 20 independent walkers and 5000 iterations that mapped a total of 10^5 models.

In the left panel of Figure 4.4.5 we compare the observed cumulative PDF ($\rm FWHM_{\it obs}$) and its uncertainty (magenta thin line and shadowed region, respectively) with the predicted cumulative PDF from the model with the highest posterior probability (black line). The parameters of this model are: $i_{\rm min} = 19^\circ$, $i_{\rm max} = 45^\circ$, $\rm FWHM_{mean} = 8500$, $\rm FWHM_{std} = 2150$, $\rm FWHM_{min} = 4200$ and $\rm FWHM_{max} = 30000$. Our model successfully reproduces the observed cumulative PDF. However, a simple normal distribution (red dashed line) is also consistent with the data and cannot be rejected. We also determined the best fit model for a distribution with $\rm FWHM_{std} = 0$, i.e., effectively a single velocity. This model (dashed blue-line) is able to reproduce the distribution at low values of $\rm FWHM_{obs}$, but it is unable to account for the distribution at large velocity widths.

First, we tested whether our thin BLR model is successful in reproducing the f–$\rm FWHM_{obs}$ distribution seen in the data (i.e., Equation 5). In the left panel of Figure 4.4.7 we show the predicted bi-dimensional probability density distribution of the virial factor and the observed FWHM(Hα) as predicted by the thin BLR model. The Figure includes contours showing 25%, 50%, 75% and 99% confidence limits contours (black-thin lines) centred around the maximum probability point. We also superposed the data from in Figure 4.4.2 (open-blue circles). The magenta line represents the derived relation $f = \left(\rm FWHM\,(H\alpha)\,/4000\ km\,s^{-1}\right)$. The thick yellow line is the median of the f–$\rm FWHM_{obs}$ distributions derived using a quantile non-parametric spline regression (Ng & Maechler, 2007). Analogously, the blue-dashed lines represent the 25%, 50% and 75% quantiles of the observational distribution. To obtained these quantiles, for each observed data we randomly generated 1000 points following the error distributions in $f_{\rm AD}$ and FWHM(Hα) and then applied the COBS method to characterize the resulting distribution. We can notice that the median (50%-quantile) of the theoretical and observational distributions are in very good agreement. The scattered open-blue circles also show excellent agreement with the the bi-dimensional probability density function from the best model. Explicitly, we find that from our 37 objects, 21% fall inside the central 25% confidence level region, 51% fall inside the 50% confidence level region, 74% fall inside the 75% confidence level region, and 85% fall inside the 99% confidence level region.

Next, we tested for the same thin BLR model whether it is possible to recover the predicted relation between $\rm FWHM_{obs}$ and $\rm FWHM_{int}$ (i.e., Equation 6). In the left panel of Figure 4.4.7 we show the predicted bi-dimensional probability distribution of $\rm FWHM_{int}$ versus $\rm FWHM_{obs}$ using the model with the highest posterior probability. The magenta solid line and magenta shadowed region represent the expected $\rm FWHM_{int} \propto FWHM_{obs}^{1/2}$ relation and 1-σ uncertainties, respectively. The solid-yellow line and yellow shadowed region represent the median $\rm FWHM_{int}$–$\rm FWHM_{obs}$ and errors from

the simulated bi-dimensional distribution. A good agreement is found between the simulations and the predicted relations. This implies that we are also able to recover the relation $\mathrm{FWHM_{int}} \propto \mathrm{FWHM_{obs}^{1/2}}$ for the thin BLR model.

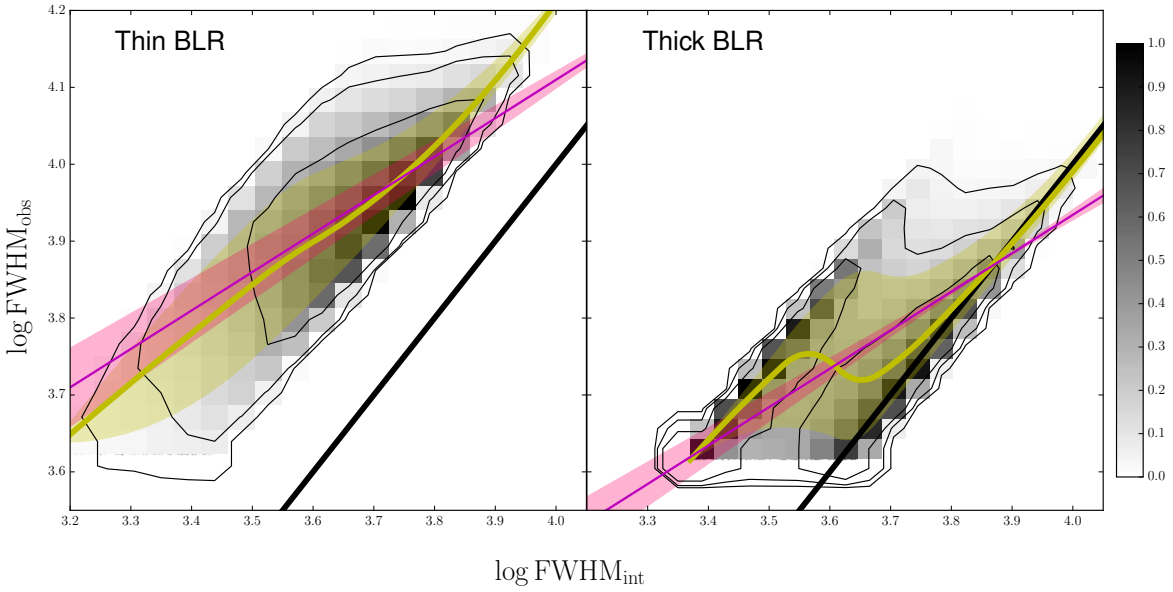

Figure 4.4.7: **$\mathrm{FWHM_{obs}$–$\mathrm{FWHM_{int}}$ bi–dimensional distributions for a thin and thick BLR.** Bi-dimensional probability distribution of the intrinsic and observed FWHM(Hα) for a thin BLR (left) and a thick BLRs (right) as predicted by the best-fit models shown in Figure 4.4.5. The darkest regions show the most probable combinations of $\mathrm{FWHM_{int}}$ and $\mathrm{FWHM_{obs}}$ values as quantified in the colour-bar. The thick black line is the 1:1 correlation. The thin black lines are the 68%, 95% and 99% confidence limit contours centred around the maximum of the probability distribution. The magenta line is the relation $\mathrm{FWHM_{int}} \propto \mathrm{FWHM_{obs}^{1/2}}$ and the width of the magenta shadowed region accounts for the uncertainties in that relation. The solid yellow line is the 50% regression quantile of $\mathrm{FWHM_{int}}$ as a function of $\mathrm{FWHM_{obs}}$ for the theoretical probability density distribution and the yellow shaded region covers the 25% to 75% percentiles. We can see that inclination closely reproduces the expected relation $\mathrm{FWHM_{int}} \propto \mathrm{FWHM_{obs}^{1/2}}$ for the thin BLR but fails to reproduce it for the thick BLR case.

In order to test the effects introduced by a thick BLR ($0 < H/R < 1$), we assumed a single H/R for all objects and followed the same steps outlined for the case of a thin BLR. We found that a wide range in BLR thickness ratios ($H/R < 0.5$) is able to reproduce the cumulative $\mathrm{FWHM_{obs}}$ PDF. However, objects with large thickness ratios clearly fail to reproduce the bi-dimensional distributions of f–$\mathrm{FWHM_{obs}}$ and $\mathrm{FWHM_{int}}$–$\mathrm{FWHM_{obs}}$, as can be seen in the right panels of Figures 4.4.6 and 4.4.7. We generally find that only relatively thin BLRs, i.e., those with $H/R < 0.1$, are able to reproduce both bi-dimensional distributions and the cumulative FWHM(Hα) PDF. In particular, for a BLR with $H/R \to 0$, we find that the derived f_{AD} values constrain the range of inclinations at which the BLR is observed in our sample to $15^\circ \lesssim i \lesssim 50^\circ$.

This upper limit is consistent with typical expectations of a central torus hiding the BLR. We also find that the median virial factor in our sample, $f = 0.95$, corresponds to a median orientation of $i_{\rm median} = 31^{\circ}$.

In summary, our results show that a population of randomly orientated, thin BLRs can successfully reproduce our observations. We can thus conclude that inclination is very likely the main reason for the observed f–FWHM$_{\rm obs}$ correlations.

4.3.5 Radiation pressure effects

We finally considered the possibility that non-virial BLR motions or winds induced by radiation pressure force might cause the observed $f_{\rm AD}$-FWHM$_{\rm obs}$ dependency. We first tested a simple model that assumes that the BLR is composed of homogeneous clouds that are optically thick to ionizing radiation but optically thin to electron scattering. The model predicts a dependency between the virial factor and the the normalized accretion rate, $\lambda_{\rm Edd}$, of the form: $f = f_1\,[1 + K\,\lambda_{\rm Edd}]$, where f_1 is the true virial factor and K depends on the fraction of ionizing radiation and the column density of the gas clouds that is assumed constant along the entire BLR (Marconi et al., 2008). From this expression we can see that $M_{\rm BH}^{\rm SE}$ underestimates the actual $M_{\rm BH}$ as $\lambda_{\rm Edd}$ increases. Equivalently, $f_{\rm AD}$ should increase as $\lambda_{\rm Edd}$ increases. However, we find no clear correlation between $\lambda_{\rm Edd}$ and $f_{\rm AD}$ in our data ($r_{\rm s} = 0.2$, $P = 0.23$), and therefore radiation pressure effects, as prescribed by this model, are not present in our objects. Note however that our sample is restricted to a relatively small range of $\lambda_{\rm Edd}$ (from $\lambda_{\rm Edd} = 0.01$ to $\lambda_{\rm Edd} = 0.3$, corresponding to a variation by a factor of 30).

A more recent model considers the effects of radiation pressure in a more realistic BLR composed of pressure confined clouds, hence allowing the gas density of individual clouds to decrease with distance to the central black hole (Netzer & Marziani, 2010). In this model the system is still bound by gravity and FWHM$_{\rm obs}$ becomes smaller with increasing $\lambda_{\rm Edd}$. The reason for this trend is that as $\lambda_{\rm Edd}$ increases, the clouds spend more time at large distances from the black hole, therefore increasing the median $R_{\rm BLR}$ and decreasing the median BLR Keplerian velocities. To account for this effect, the authors of this model proposed a modified expression for $R_{\rm BLR}$:

$$R_{\rm BLR} = R_{\rm BLR}^{0}\,[a_1 L_{\lambda}^{\alpha_{\rm line}} + a_2\,(L_{\lambda}/M_{\rm BH})] \tag{4.4.8}$$

where a_1 and a_2 are constants. The first term accounts for the observational relation described in Equation 4.4.4 and the second term represents a radiation pressure perturbation quantified by $L_{\lambda}/M_{\rm BH} \propto \lambda_{\rm Edd}$. When replaced into the virial mass equation (Equation 4.4.1) this relation leads to a simple quadratic equation on $M_{\rm BH}$ with solution:

$$M_{\rm BH}^{\rm rad} = \frac{a_{10}}{2} L^{\alpha_{\rm line}} {\rm FWHM_{obs}}^{2} \left[1 + \sqrt{1 + \frac{4\ a_{20} L_{\lambda}^{1-2\alpha_{\rm line}}}{a_{10}^{2}\ {\rm FWHM_{obs}^{2}}}}\right] \tag{4.4.9}$$

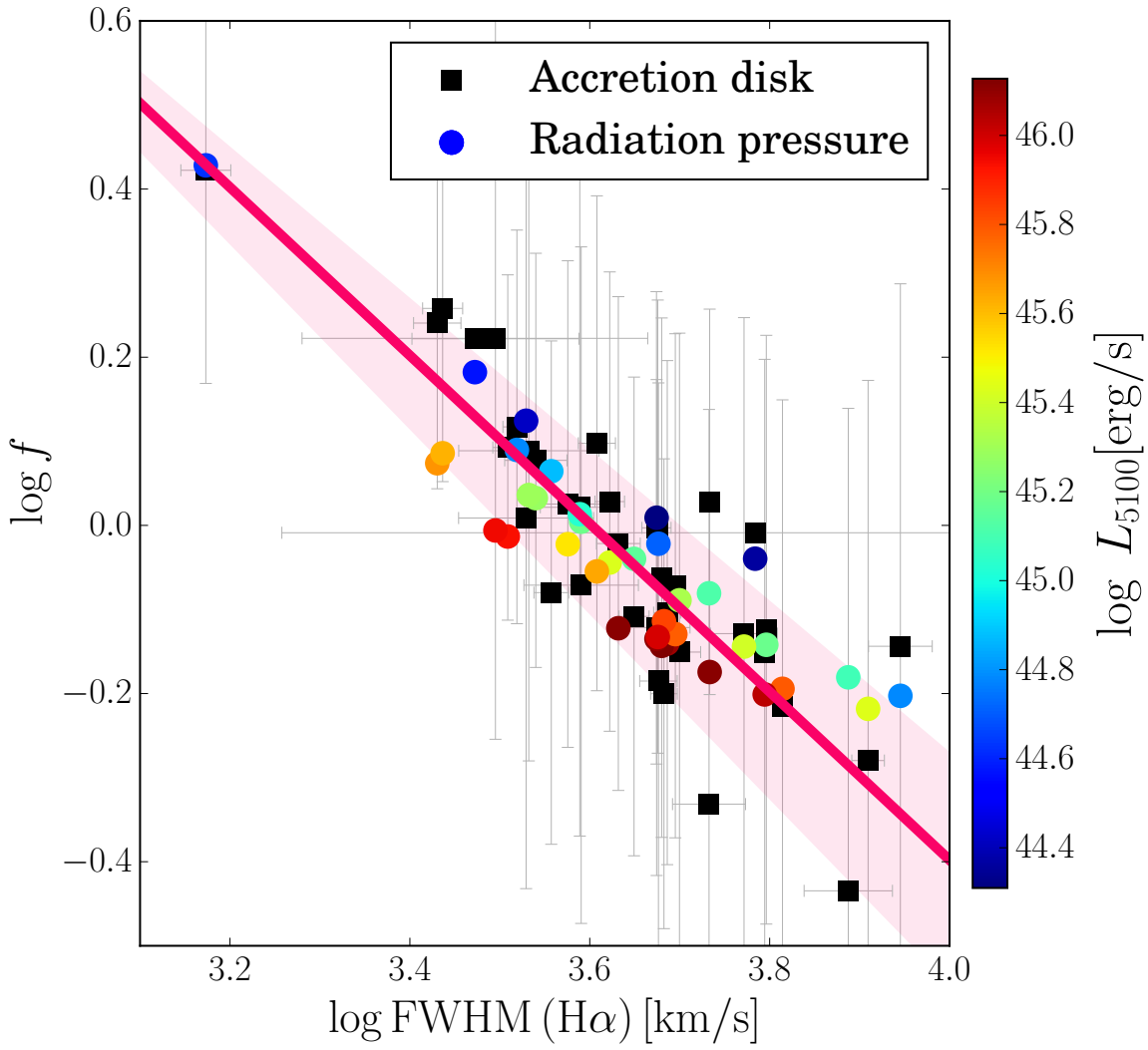

Figure 4.4.8: **Radiation pressure in a gravitationally bound BLR.** The observed virial factor vs $\mathrm{FWHM_{obs}}$ for the Hα line is shown (black squares). The magenta line is the derived relation $f = \left(\mathrm{FWHM\,(H\alpha)}\,/4000\ \mathrm{km\,s^{-1}}\right)$ and the width of the shadowed region accounts for the uncertainties in that relation. The filled points represent the modelled $f_{\rm rad}$ from the best fit model for radiation pressure in a gravitationally bound BLR. The colour of the points scales with the measured monochromatic luminosity at 5100Å (L_{5100}) for each object, as indicated by the colour bar. Redder (bluer) points correspond to larger (smaller) values of L_{5100}. As can be observed, the model predicts that the scatter in $f_{\rm rad}$ (coloured points) is driven by L_{5100} (see Equation 4.4.10). This dependence is not seen in our data (black squares) as shown in Figure 4.4.2. Nevertheless, the relatively large errors in $f_{\rm AD}$ and the weak dependence of $f_{\rm rad}$ in L_{5100} may probably hide the expected dependence from this radiation pressure model.

or equivalently:

$$f_{\rm rad} \propto \left[1 + \sqrt{1 + \frac{4\ a_{20} L_\lambda^{1-2\alpha_{\rm line}}}{a_{10}^2\ \mathrm{FWHM_{obs}^2}}}\right] \tag{4.4.10}$$

where $M_{\rm BH}{}^{\rm rad}$ and $f_{\rm rad}$ are the black hole mass and virial factor for a radiation pressure dominated BLR. $a_{10} = a_1 f_0\ R^0_{\rm BLR} G^{-1}$, $a_{20} = a_2 f_0\ R^0_{\rm BLR} G^{-1}$, and f_0 is a normalization constant. In the case when $4\ a_{20} L_\lambda^{1-2\alpha_{\rm line}} / a_{10}^2\ {\rm FWHM}^2_{\rm obs} \gg 1$ this would result in a close agreement with the inverse proportionality between $f_{\rm AD}$ and ${\rm FWHM}_{\rm obs}$ found in our data. Given that $\alpha_{\rm line}$ is found to be ~ 0.6 for all lines (Table 4.2), this would translate into an explicit dependency of f on L_λ. We would then expect that the scatter in the $f_{\rm AD}$–${\rm FWHM}_{\rm obs}$ relation should be driven by L_λ. In Figure 4.4.2 larger (smaller) values of L_{5100} are represented by redder (bluer) colours. We can see that there is no clear suggestion that the scatter in driven by L_{5100} in any of the lines. Note however that the relatively narrow range in L_{5100} covered by our sample (from $L_{5100} = 2.0 \times 10^{44}$ to $L_{5100} = 1.6 \times 10^{46}$ ergs/s, corresponding to a factor of 80), together with the uncertainties in our estimations of f, do not allow us to rule out this mechanism.

Testing this model further, we found the combination of parameters a_1, a_2 and f_0 that best reproduce our $M^{\rm AD}_{\rm BH}$ measurements and the observed relation between f and ${\rm FWHM}_{\rm obs}$ for the Hα line. To obtain dimensionless values for a_1 and a_2 we expressed $M_{\rm BH}$, L_λ and FWHM in units of $10^8 M_\odot$, $10^{44}{\rm erg\,s^{-1}}$ and 1000 ${\rm km\,s^{-1}}$, respectively. Taking $\alpha_{\rm line} = 0.63$, as suggested by the observations (see Table 4.2), we carried out a Monte-Carlo Markov Chain exploration of the parameter space of the model and found that $a_1 = 0.88$, $a_2 = 0.36$ and $f_o = 0.51$ are able to reproduce our $M^{\rm AD}_{\rm BH}$ measurements with a scatter of 0.12 dex, preserving the experimental dependence of $R_{\rm BLR}$ on L_λ as expressed in Equation 4.4.4 with a scatter of 0.05 dex. At the same time the results are able to reproduce the observed f–${\rm FWHM}_{\rm obs}$ relation with a scatter of 0.11 dex (see Figure 4.4.8, which presents our observations (black squares with error bars) together with the prescribed values for f as given by Equation 4.4.10 (colored circles without error bars)). However, we also found that the residuals between the predicted values and the best fit to the correlation are heavily correlated with L_{5100} ($r_s > 0.63$, $P_s < 2 \times 10^{-5}$), as can be seen by the color gradient of our simulated points in the direction perpendicular to the correlation best fit in Figure 4.4.8. This bias is introduced by the explicit dependence of $f_{\rm rad}$ on L_λ which is not observed in our sample, although notice that the error bars of our derived f values are of the order of, if not larger, than the expected dependence (see Figure 4.4.8). Finally, the dependency on L_{5100} vanishes when $\alpha_{\rm line} = 0.5$. For this case, however, we were unable to reproduce any the observables. Extending our sample towards lower luminosities should yield the final test to be able to confidently conclude whether this model can be the driving mechanism for the observed f–${\rm FWHM}_{\rm obs}$ correlation.

Chapter 5

Conclusions

Here I present the most relevant conclusions of this thesis which is oriented to improve current mass estimation methods of distant SMBHs and to infer the physical properties of the BLR.

In chapter 2 we used a unique sample of 39 type-I AGN observed by X-Shooter and uniformly covering the $M_{\rm BH} - L/L_{\rm Edd}$ plane at $z = 1.55$ down to $i_{\rm AB} \sim 21$ mag. Our sample allows for a comprehensive comparison between different luminosity probes and emission line measurements, for the prominent broad emission lines Hα, Hβ, Mg II and C IV, which are commonly used for virial SMBH mass estimates. Thanks to the broad spectral coverage, we were also able to test two approaches for continuum fitting and test for possible biases in $M_{\rm BH}$ determinations: a physically-motivated approach based on fitting an accretion disc model to each spectrum; and a more practical approach which treats the continuum around each prominent line as an independent power-law.

In summary, the main findings of this work are:

1. Comparing the two continuum fitting approaches, we find only small (although systemic) offsets in the derived line luminosities, local continua luminosities, and line FWHMs, and consequently in $M_{\rm BH}$ determinations (< 0.05 dex). This implies that a precise modeling of the continuum emission is *not* crucial for $M_{\rm BH}$ determinations.

2. Line dispersion measurements ($\sigma_{\rm line}$) are highly sensitive to continuum modelling, and cannot be safely used for $M_{\rm BH}$ determination, even for the well-studied Balmer lines and/or when high-quality spectra of broad UV lines are available.

3. We corroborate that both the Hα and Hβ lines show very similar FWHMs and can be consistently used for estimating $M_{\rm BH}$ based on the virial assumption.

4. The Mg II line width is found to follow that of Hβ, and, generally, can be safely used for $M_{\rm BH}$ estimations. Our new observations show that the MgII line is about

30±15% narrower than Hβ (in FWHM). We also found that about 10% of the objects show atypically *broad* Mg II lines, with FWHM (Mg II) $\gtrsim$ FWHM (Hα). These Mg II profiles are also systematically blue-shifted, probably due to non-virial dynamics, and further shown to be not suitable for reliable $M_{\rm BH}$ estimation (see §2.4.3.4). We note that broad-Mg II objects can only be identified using additional information from one of the Balmer lines, which would in turn eliminate the necessity to identify them. Without any additional information, such sources may be present in any sample of AGN.

5. We find that FWHM measurements for C IV in low-S/N spectra are systematically underestimated, for objects with partially resolved or unresolved C IV absorption features. We also find that the FWHMs of Mg II and the FWHMs of non-absorbed C IV profiles are consistent in low- and high-S/N data sets. On the other hand, the line dispersion measurements ($\sigma_{\rm line}$) for both C IV and Mg II profiles differ significantly (a scatter of ~ 0.2 dex).

6. $L/L_{\rm Edd}$ seems to affect the dynamics of the Mg II-emitting region, especially in objects with extreme accretion rates (as pointed out by Marziani et al. (2013a)).

7. We provide new single epoch calibrations for $M_{\rm BH}$, based on the FWHM of Hα, Hβ, Mg II and C IV.

8. The considerable uncertainties associated with C IV-based determination of $M_{\rm BH}$ are not solely due to insufficient spectral resolution and/or S/N. They are more likely related to the physics of the BLR. Our results are in agreement with some earlier findings about the systematic uncertainties associated to C IV. We found that the $L/L_{\rm Edd}$ is strongly correlated with FWHM (C IV) /FWHM (Hα) and with the velocity offset of the C IV line. We stress, however, that these correlations show large scatter and cannot practically assist in improving $M_{\rm BH}$ (C IV) estimates.

9. We confirm the result of Runnoe et al. (2013), finding a significant correlation between the Si IV+O IV]/C IV line peak ratio and FWHM(C IV)/FWHM(Hβ), which may in principle assist rehabilitating C IV-based $M_{\rm BH}$ determinations. Moreover, we find even stronger correlations associated with the C III]/C IV line peak ratio. In contrast to Runnoe et al. (2013), our results indicate that these empirical correlations do *not* significantly reduce the scatter in $M_{\rm BH}$ (C IV) estimates. These opposite results are probably a consequence of the limited number of objects (< 100 objects) in our sample as well as in the sample of Runnoe et al. (2013). To evaluate the robustness and usefulness of these methods, it is important to test these correlations on larger and more complete samples.

Motivated by the latter result, in chapter 3 we used the SDSS sample to test the validity of the practical alternatives to improve C IV-based $M_{\rm BH}$ estimations proposed

to date. Particularly, we tested the methods proposed by Runnoe et al. (2013), Mejía-Restrepo et al. (2016) and Coatman et al. (2017) which are all based on correlations between different observables associated to the C IV emission and the ratio of FWHM(C IV) and the FWHM of low-ionization lines (i.e. Hα, Hβ and Mg II). In spite of the good quality of the data used in these works, all these methods were derived on small samples that show limited coverage of the parameter space of the observables that are involved.

The usage of the SDSS DR7Q and the DR12Q quasar databases (which in spite of their data quality limitations are more representative of the quasar population) indicates that all these methods are of limited applicability to improve C IV-based $M_{\rm BH}$ estimations. In fact, we find that the aforementioned methods depend on correlations that are actually associated to the FWHM of the C IV profile itself and not to an interconnection between FWHM(C IV) and the FWHMs of the low ionization lines. Further support comes from the principal component analysis (PCA) described in the Appendix B.3. This analysis revealed that the first Eigenvector is mostly driven by the anti-correlation between FWHM(C IV) and the quantities used in Runnoe et al. (2013), Mejía-Restrepo et al. (2016) and Coatman et al. (2017) to improve C IV-bases mass estimations. Notably, the second Eigenvector is mostly driven by FWHM(Mg II) and shows no correlation with any C IV related quantity. This indicates that the formation of the Mg II and C IV profiles is independent from each other. In other words, there is no-possibility to relate the non-virialized C IV emission with the virialized Mg II emission.

Finally, in chapter 4, we evaluated the effects of the gas distribution on the determination of single epoch black hole masses. This study was possible thanks to the comparison of single epoch black hole mass estimations with those obtained from fitting standard disc models to the observed accretion disc SED. Our results show that the virial factor is inversely proportional to the observed width of the broad emission lines. We also find that line-of-sight inclination of gas in a planar distribution is the most probable cause for this effect. However, radiation pressure effects on the distribution of gas can also reproduce our findings. Regardless of the physical origin, our results provide an straightforward procedure to mitigate the uncertainties in single epoch black hole mass estimations associated to our ignorance of the actual virial factor in each source.

Appendix A

Complementary information to Chapter 2

A.1 Demonstrating the quality of X-Shooter spectra

Figure A.A.1 compares the newly obtained X-Shooter spectrum (UVB+VIS arms) to the publicly available SDSS spectrum, for J0143–0056 - the source shown in Figs. 2.2.3 and 2.2.4. This source has a $S/N \simeq 25$ at 2000Å which lies in the middle of the S/N range for the entire sample. Both spectra are presented *without* any binning or smoothing, including the residual sky and/or instrumental features. We note the significant improvements to S/N and spectral resolution, as evident from the minor absorption feature on the blue wing of the C III] λ1909 line. The broader spectral coverage allows for a much more robust determination of the continuum level next to the C IV and Mg II emission lines (i.e., L_{1450} and L_{3000}. Obviously, the NIR arm of X-Shooter includes the Hβ and Hα spectral regions (not shown here), which are unavailable in the SDSS data.

A.2 New UV iron emission template

In figure A.A.2 we compare our new UV iron template with the template of T06.We prefer the use of our new template motivated by the following three reasons:

- The T06 template severely underestimates the continuum emission around 2100Å.
- T06 modelled the BC continuum as a modified Black Body following (Grandi, 1982). This does not provide a good approximation to Balmer emission and we

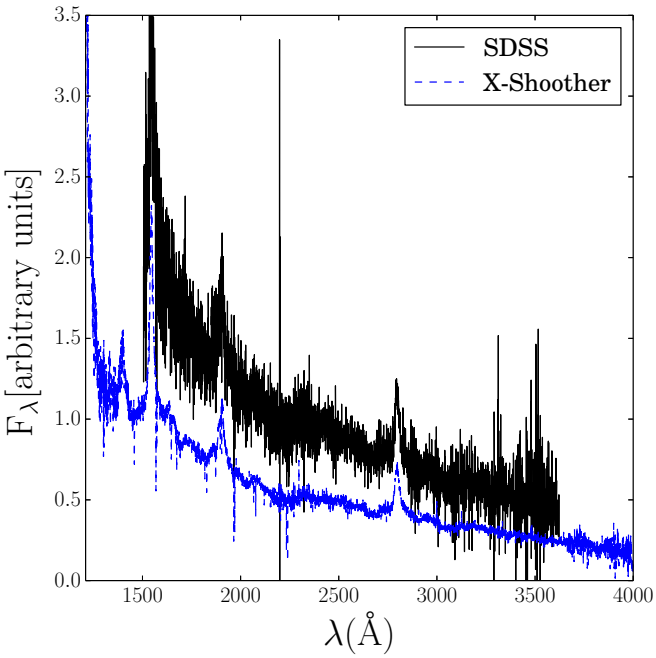

Figure A.A.1: SDSS and X-Shooter spectra of J0143-0056. Both spectra have been rescaled to avoid overlapping.

prefer templates based on photo-ionization calculations.

- The T06 template only extends between 2200Å and 3500Å. However, there is still a remaining weaker but still non-negligible contribution from iron emission up to the Balmer limit (3647Å). The correct estimation of iron emission in this regions (3500Å to 3647Å) is crucial for estimating the emission by iron lines and to prevent overestimation of the BC.

We constructed the template following T06 and VW01 procedures and using our own estimations of the accretion-disc emission and Balmer continua. We redefined the

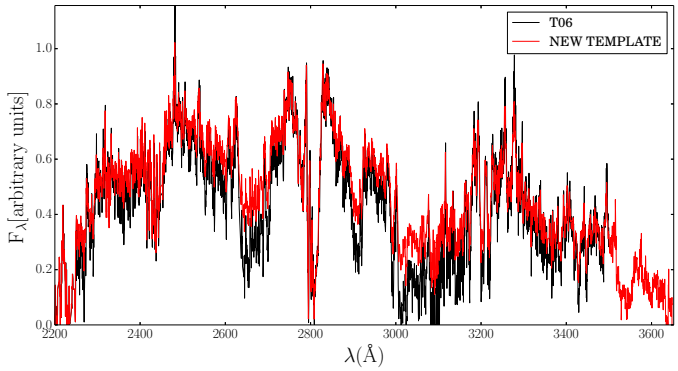

Figure A.A.2: Comparison of our new template (red) and Tsuzuki et al. (2006) template (black).

accretion-disc-continuum by manually selecting the continuum windows at ∼2100Å and ∼4200Å which account for the region where we require to obtain the new iron template (2100-3647Å) . The Balmer continuum model that we use is described in section 2.3.

Our template provides stronger iron emission, particularly in the range of 2620-3500 Å, which is crucial for Mg II measurements. This could be explained by our different Balmer continuum approach and disc continuum windows.

A.3 Emission line constraints

Table A.1 lists the constraints on the emission line modeling for each of the components in our fitting procedure following Shang et al. (2007) and Vanden Berk et al. (2004).

A.4 Comparison of Observed Emission Line Profiles

In Figures A.A.3 and A.A.4 we show the normalized profiles of the Hα, Hβ, Mg II and C IV emission lines, in velocity space. In most but not all sources, the C IV profiles (red) are broader and blue shifted with respect to the Hα and Hβ line profiles as discussed in §2.4.3. The low ionization lines, Hα, Hα and Mg II, show similar shape profiles. Hβ is generally slightly broader than Hα. Mg II is, on average, 30% narrower than Hβ. The five broad-Mg II objects (top-row) show Mg II that are broader than Hα and Hβ. These Mg II profiles are also slightly blue-shifted (about 300 km s^{-1}) relative to the Hβ line. The two BALQSOs are the last two objects of the bottom row on the second set.

Table A.1: *Line regions and adopted constraints. Under the global approach the C*IV *and C*III*] line regions are fitted simultaneously*

ID	LINE	λ	GAUSSIAN COMPONENT	Flux	Center	FWHM	FLUX RATIO
Si IV + O IV] Region							
1	Si IV	1396.75	Broad	Free	Free	Free	Free
2			Narrow	Free	1	Free	Free
3	O IV]	1402.34	Broad	Free	1	Free	Free
4			Narrow	Free	2	Free	Free
C IV Region							
1	N IV]	1486.5		Free	Free	Free	
2	C IV	1548.2	Narrow	Free	Free	Free	Free
3			Broad	Free	Free	Free	Free
4	C IV	1550.77	Narrow	Free	2	2	1
5			Broad	Free	3	3	1
6	He II	1640.72	Narrow	Free	Free	Free	
7			Broad	Free	6	Free	
8	O III]	1660.8		Free	1	Free	0.29
9		1666.14		8	8	8	0.71
10	N IV	1718.75		Free	Free	Free	Free
C III Region							
11	C III]	1908.73	Narrow	Free	Free	Free	
12			Broad	Free	13	Free	
13	Si III]	1892.03		Free	11	Free	
14	Al III	1854.72		Free	13	Free	1
15		1862.78		14	14	14	1
16	Si II	1818.17		Free	11	Free	
17	Fe II	1788.73		16	16	16	
18	N III]	1748.65		13	13	13	0.41
19		1752.16		18	18	18	0.14
20		1754.00		18	18	18	0.45
Mg II Region							
1	Mg II	2795.53	Narrow	Free	Free	Free	2
2			Broad	Free	1	Free	2
3	Mg II	2802.71	Narrow	1	1	1	1
4			Broad	2	2	2	1
5	Fe	Template		Free	Free	Free	
Hβ Region							
1	Hβ	4861.32	Narrow	Free	Free	Free	
2			Broad	Free	Free	Free	
3			NLR	Free	4	4	
4	[O III]	5006.84		Free	Free	Free	3
5		4958.91		4	4	4	1
6	He II	4685.65		Free	Free	Free	
7	Fe II	s		Free	...	Free	
Hα Region							
1	Hα	6562.8	Narrow	Free	Free	Free	
2			Broad	Free	Free	Free	
3			NLR	Free	Free	4	
4	[N II]	6548.06		Free	4	[O III] width	1
5		6583.39		4	4	4	3
6	[S II]	6716.47		Free	4	4	1
7		6730.85		6	6	6	1

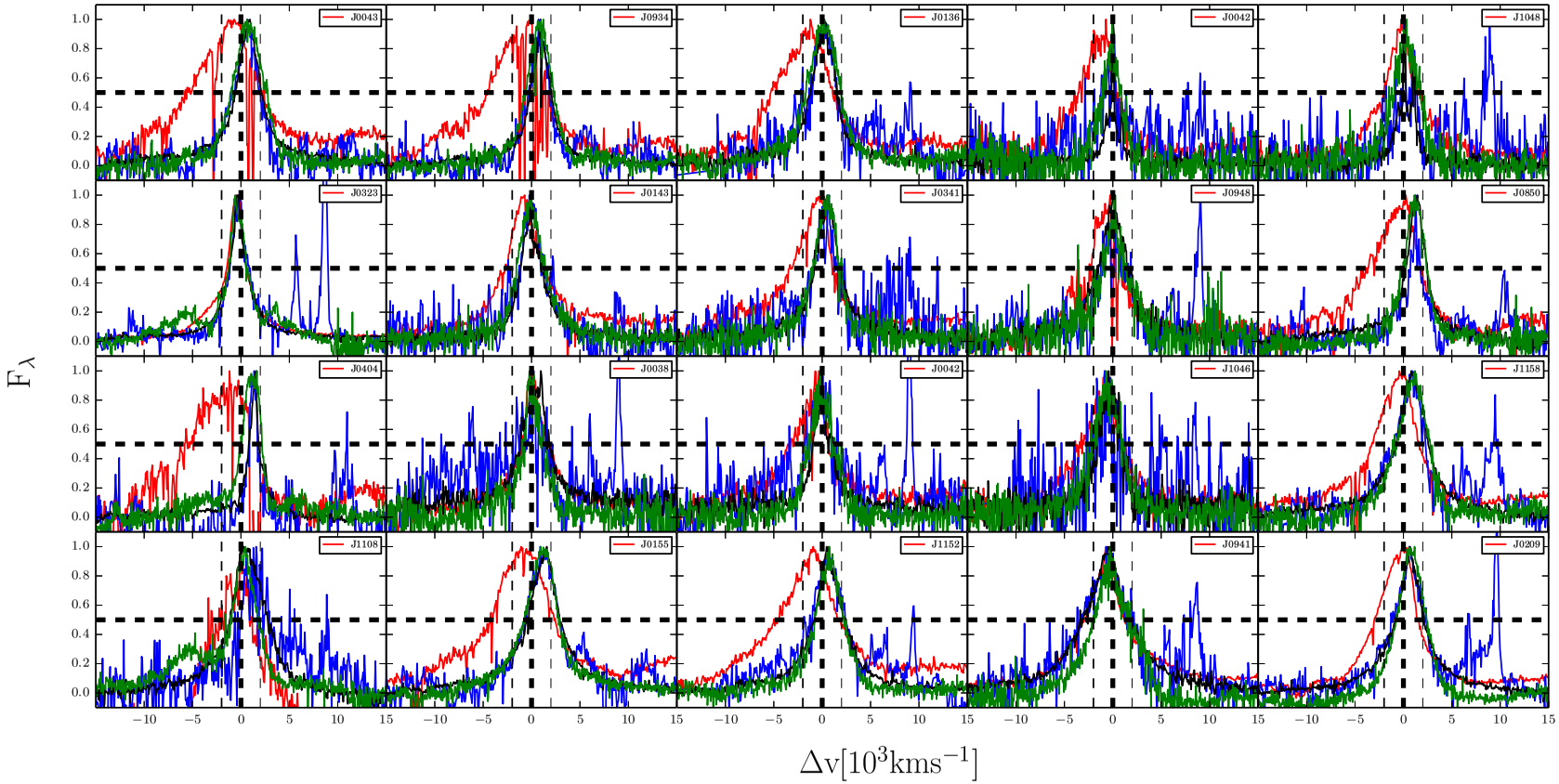

Figure A.A.3: Comparison of the observed Hα (black), Hβ (blue), Mg II (green) and C IV (red) line profiles in the velocity space for the objects in the sample with satisfactory Thin disc continuum fits. All profiles have been normalized relative to the peak flux density of the line. It is important to remark that both the Mg II and C IV profiles are doublets and their decomposed profiles are narrower than shown here. In the top row we show the five broad-Mg II objects.

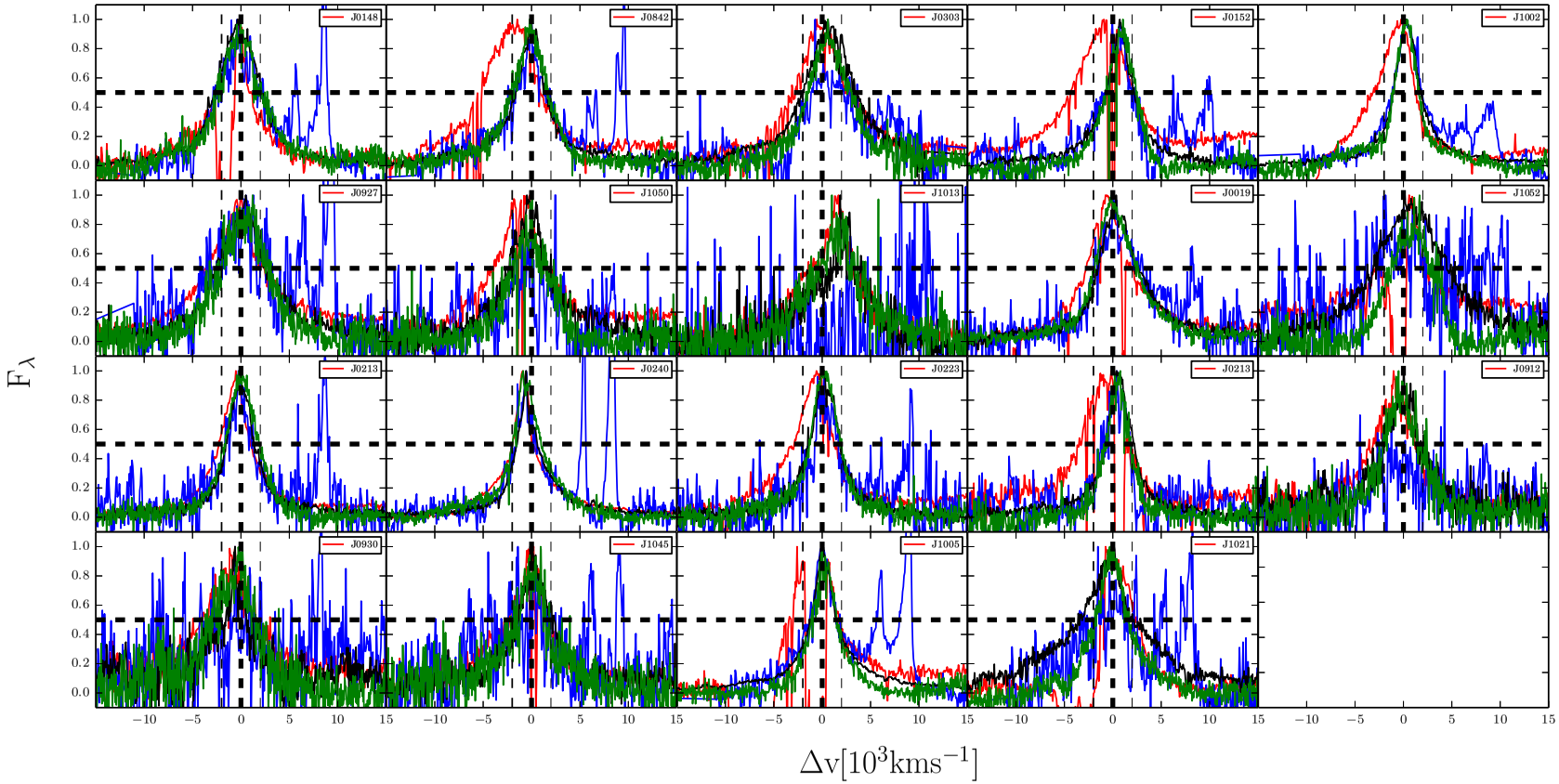

Figure A.A.4: - continued. Comparison of the observed Hα (black), Hβ (blue), Mg II (green) and C IV (red) line profiles in the velocity space for the objects in the sample with satisfactory Thin disc continuum fits. All profiles have been normalized relative to the peak flux density of the line. It is important to remark that both the Mg II and C IV profiles are doublets and their decomposed profiles are narrower than shown here. To the left of the bottom row we show the two BALQSO objects.

Appendix B

Complementary information to Chapter 3

B.1 Fitting Procedure, measurements and BALQSO exclusion

Our broad emission line modelling follows the procedure presented by Mejía-Restrepo et al. (2016) and Trakhtenbrot & Netzer (2012). Very briefly, the most prominent lines (Si IV+O IV], C IV, C III] and Mg II) are modelled using two Gaussian components while other weak emission lines are modelled with a single Gaussian (including He II1640, N IV1718, Si III]1892). The central wavelength of each Gaussian component is restricted to move within 1000 km s^{-1} around the laboratory central wavelength. The C IV and He II1640 are allowed to be blue shifted up to 5000 km s^{-1}.

We automatized the procedure by introducing some additional steps to the line and continuum fitting. We first proceed to fit and subtract the continuum emission within a pair of continuum windows around each line. These continuum windows are set at the wavelengths that we list in Table B.1. We subsequently fit the emission line following the "local" approach described in Mejía-Restrepo et al. (2016). After this we obtain the residuals of the fitting and remove the pixels with the 3% most negative fluxes

Table B.1: *Spectral pseudo-continuum windows used for our line fitting procedure under the local continuum approach.* [1]*For each object, we manually adjusted the continuum bands, using the listed wavelength ranges as a reference.*

Line Complex	Continuum windows[1]	
Si IV+O IV]	1340-1360Å	1420-1460Å
C IV	1430-1460Å	1680-1720Å
C III]	1680-1720Å	1960-2020Å
Mg II	2650-2670Å	3020-3040Å

Table B.2: *Pearson correlation coefficients between the listed quantities for the DR7Q and DR12Q samples.*

	DR7Q correlations												
Property	1	2	3	4	5	6	7	8	9	10	11	12	13
[1]FWHM(C IV)	1	0.17	0.71	0.34	-0.51	0.44	-0.63	-0.51	0.36	-0.11	-0.83	0.22	-0.19
[2]FWHM(Mg II)	0.17	1	-0.58	0.1	0.11	-0.19	-0.07	0.03	-0.09	0.07	-0.2	0.6	-0.1
[3]FWHM [C IV/Mg II]	0.71	-0.58	1	0.21	-0.5	0.5	-0.47	-0.45	0.36	-0.15	-0.55	-0.24	-0.09
[4]L_{1450}	0.34	0.1	0.21	1	-0.28	0.37	-0.36	-0.36	0.07	-0.09	-0.44	0.08	-0.16
[5]$\Delta V_{\rm peak}$ (C IV)	-0.51	0.11	-0.5	-0.28	1	-0.68	0.49	0.5	-0.39	0.25	0.45	-0.05	0.07
[6]$\Delta V_{\rm line}$ (C IV)	0.44	-0.19	0.5	0.37	-0.68	1	-0.51	-0.53	0.34	-0.25	-0.48	-0.03	-0.09
[7]$L_{\rm peak}$ [C IV/1450Å]	-0.63	-0.07	-0.47	-0.36	0.49	-0.51	1	0.65	-0.6	0.77	0.58	-0.2	0.07
[8]$L_{\rm peak}$ [C IV/SiOIV]	-0.51	0.03	-0.45	-0.36	0.5	-0.53	0.65	1	-0.47	0.45	0.43	-0.08	0.03
[9]$L_{\rm peak}$ [C IV/C III]]	0.36	-0.09	0.36	0.07	-0.39	0.34	-0.6	-0.47	1	-0.55	-0.23	0.03	0.15
[10]EW(C IV)	-0.11	0.07	-0.15	-0.09	0.25	-0.25	0.77	0.45	-0.55	1	-0.08	-0.06	-0.13
[11]$L_{\rm peak}$ (C IV) /L (C IV)	-0.83	-0.2	-0.55	-0.44	0.45	-0.48	0.58	0.43	-0.23	-0.08	1	-0.23	0.28
[12]FWHM (Mg II) /σ (Mg II)	0.22	0.6	-0.24	0.08	-0.05	-0.03	-0.2	-0.08	0.03	-0.06	-0.23	1	-0.19
[13]L_{3000}/L_{1450}	-0.19	-0.1	-0.09	-0.16	0.07	-0.09	0.07	0.03	0.15	-0.13	0.28	-0.19	1
	DR12Q correlations												
[1]FWHM(C IV)	1	0.14	0.71	0.39	-0.37	0.39	-0.53	-0.46	0.33	-0.01	-0.5	0.16	-0.01
[2]FWHM(Mg II)	0.14	1	-0.6	0.08	-0.01	-0.08	-0.01	0.07	-0.04	0.08	-0.11	0.58	0.02
[3]FWHM [C IV/Mg II]	0.71	-0.6	1	0.25	-0.29	0.37	-0.41	-0.42	0.29	-0.07	-0.32	-0.29	-0.03
[4]L_{1450}	0.39	0.08	0.25	1	-0.31	0.43	-0.37	-0.53	0.27	-0.06	-0.29	0.11	0.14
[5]$\Delta V_{\rm peak}$ (C IV)	-0.37	-0.01	-0.29	-0.31	1	-0.66	0.39	0.37	-0.29	0.13	0.22	-0.01	-0.08
[6]$\Delta V_{\rm line}$ (C IV)	0.39	-0.08	0.37	0.43	-0.66	1	-0.45	-0.46	0.29	-0.14	-0.27	-0.02	0.03
[7]$L_{\rm peak}$ [C IV/1450Å]	-0.53	-0.01	-0.41	-0.37	0.39	-0.45	1	0.59	-0.53	0.58	0.28	-0.11	-0.04
[8]$L_{\rm peak}$ [C IV/SiOIV]	-0.46	0.07	-0.42	-0.53	0.37	-0.46	0.59	1	-0.47	0.27	0.26	-0.08	-0.09
[9]$L_{\rm peak}$ [C IV/C III]]	0.33	-0.04	0.29	0.27	-0.29	0.29	-0.53	-0.47	1	-0.3	-0.16	0.07	0.28
[10]EW(C IV)	-0.01	0.08	-0.07	-0.06	0.13	-0.14	0.58	0.27	-0.3	1	-0.61	-0	-0.04
[11]$L_{\rm peak}$ (C IV) /L (C IV)	-0.5	-0.11	-0.32	-0.29	0.22	-0.27	0.28	0.26	-0.16	-0.61	1	-0.1	0.01
[12]FWHM (Mg II) /σ (Mg II)	0.16	0.58	-0.29	0.11	-0.01	-0.02	-0.11	-0.08	0.07	-0	-0.1	1	-0.07
[13]L_{3000}/L_{1450}	-0.01	0.02	-0.03	0.14	-0.08	0.03	-0.04	-0.09	0.28	-0.04	0.01	-0.07	1

within the continuum windows. The purpose of this step is to exclude from the fitting strong absorption features. We repeat the entire procedure three times to guarantee convergence. We also exclude from our sample objects with final reduced χ^2 larger than 3.

To avoid C IV BALQSOs we excluded from the sample objects with more than 7% of the pixels with negative C IV residuals. To test the performance of this automatic selection method we compare the objects that are flagged as BALQSOs using our method with the sample of 562 manually classified BALQSOs from the SDSS-DR2 quasar database that is described in Ganguly et al. (2007). With our criterion we flagged as BALQSO a total of 573/5088 objects from the SDSS-DR2 quasar catalogue at $1.7 < z < 2.0$. From these objects we found that 560/562 objects are also classified as BALQSO in the manually selected Ganguly et al. (2007) sample. These results translate into a successful identification rate of 99.6% and a false positive identification rate of 2.3%. After excluding the BALQSO candidates and objects with unreliable fits we end up with 3267 from the DR7Q catalogue (out of the originally selected 4817 objects) and with 35674 objects from the DR12Q catalogue (out of the originally selected 69092 objects).

B.2 Sample comparison

Here we describe in detail the parameter space of the most relevant physical quantities derived for the samples and summarize the most relevant issues associated to each of the of the small and large samples used in chapter 3.

B.2.1 Large sample remarks

- In both SDSS samples we can observed that FWHM(C IV) and L_{1450} correlate with each other ($r_{\rm p} \equiv r_{\rm Pearson} \sim 0.35$). This Indicates that, on average, more luminous quasars typically show broader C IV line profiles. However, the FWHM(Mg II) is completely independent of the quasar luminosity ($r_{\rm p} < 0.05$ in both SDSS samples).

- The DR12Q sample probes considerably fainter sources, compared with the DR7Q sample (by $\sim$ 0.5dex), and extends to $L_{1450} \gtrsim 10^{44.5}{\rm erg\,s^{-1}}$. This difference between both samples allows us to directly test the impact of luminosity limited samples as well as data quality in our analysis.

- In the case of $\log {\rm FWHM\,(C\,IV)}$ and $\log {\rm FWHM\,(Mg\,II)}$ both SDSS samples span similar ranges, from $\sim$3 to $\sim$4.2 in $\log {\rm FWHM\,(C\,IV)}$ and from $\sim$3 to $\sim$3.8 in $\log {\rm FWHM\,(Mg\,II)}$. However, the DR12Q sample has a larger fraction of object with low $\log {\rm FWHM\,(C\,IV)}$ and $\log {\rm FWHM\,(Mg\,II)}$. Explicitly, 5% (10%) of the objects in the DR12Q sample have ${\rm FWHM\,(C\,IV)} \lesssim 3.3$ (${\rm FWHM\,(Mg\,II)} \lesssim 3.3$) versus 2% (6%) in the DR7Q sample. Additionally, the DR12Q sample has a larger fraction of objects with $\log {\rm FWHM\,(Mg\,II)} > 3.8$. The sharp cut at $\log$ FWHM (C IV) = $\log$ FWHM (Mg II) = 3 is imposed by the fitting criterion.

- The $\log {\rm FWHM\,[C\,IV/Mg\,II]}$ distribution in both samples span over similar ranges, from $\sim$-0.6 to $\sim$0.8. However, the DR12Q sample shows a larger fraction (28%) of objects with $\log {\rm FWHM\,[C\,IV/Mg\,II]} < 0$ than the DR7Q sample (20%).

- We can observe that the DR12Q sample shows a larger fraction (roughly 10%) of objects with $\log$ $L_{\rm peak}\,[{\rm C\,IV/SiOIV}]$ and $\log$ $L_{\rm peak}\,[{\rm C\,IV/C\,III}] \gtrsim 1$ than the DR7Q sample (roughly $\sim$ 5%). We need however to be cautious about the reliability of such measurements because those objects show $L_{\rm peak}\,({\rm Si\,IV + O\,IV}]$) and $L_{\rm peak}\,({\rm C\,III}]$) weaker than one tenth of $L_{\rm peak}\,({\rm C\,IV})$. Thus, the signal to noise of the C III] and Si IV+O IV] line profiles is probably very low in many of those objects. We can also appreciate that the DR12Q and DR7Q samples show a similar distribution in $\log$ $L_{\rm peak}\left[{\rm C\,IV/1450\AA}\right]$.

- As we already explained, DR7Q blue-shift estimations are more accurate that in DR12Q. Additionally, we can observe in Fig. 3.3.4 that the $\Delta V_{\rm peak}\,({\rm C\,IV})$ and the $\Delta V_{\rm line}\,({\rm C\,IV})$ distributions show a larger fraction of objects with small blue-shifts in the DR12Q sample than in the DR7Q sample (6% in DR7Q vs 23%

DR12Q and 12% in DR7Q vs 28% in DR12Q for $\Delta V_{\rm peak}$ (C IV) and $\Delta V_{\rm line}$ (C IV) < 200 km s^{-1} respectively) . This behaviour is probably caused by objects in the DR12Q sample whose cosmological redshift has been estimated using the C IV profile. This effect artificially biases the C IV blue-shifts towards values close to 0. Because of these problems with the DR12Q redshift determinations we will mainly focus our blue-shift analysis on the DR7Q sample.

B.2.2 Small sample remarks

- The Runnoe+13 sample is mostly described by uniform distributions in L_{1450}, FWHM(C IV) and FWHM(Mg II) that are fairly similarly distributed around the SDSS data. However, RL AGN are mostly high luminosity objects. We can also observe that the Runnoe+13 FWHM [C IV/Mg II] distribution is clearly shifted towards larger values than the peak of the SDSS distributions. In terms of $\Delta V_{\rm peak}$ (C IV), the sample is shifted towards low values (75% with < 1000 km s^{-1}). Finally, in terms of the line peak ratios, $\log L_{\rm peak}$ (C IV) $/L_{\rm peak}$ (Si IV + O IV]) and $\log L_{\rm peak}$ (C IV) $/L_{\rm peak}$ (C III]), the sample is shifted towards large values (75% with $\gtrsim 0.5$).

- The X-Shooter sample also shows flat distributions in $\log L_{1450}$, $\log$ FWHM (C IV) and $\log$ FWHM (Mg II) that are also fairly spread around the SDSS data. Its $\log$ FWHM [C IV/Mg II] is clearly distributed towards values lower than the peak of the SDSS distribution. It can be observed that the line peak ratios ($\sim$75% with $\log L_{\rm peak}$ (C IV) $/L_{\rm peak}$ (Si IV + O IV]) $\lesssim 0.5$ and $\log L_{\rm peak}$ (C IV) $/L_{\rm peak}$ (C III]) $\lesssim 0.5$) and blue-shifts (75% with < 1000 km s^{-1}) are both distributed towards low values with respect to the SDSS distribution peaks.

- The Coatman+2017 sample is clearly dominated by objects with very large L_{1450} ($L_{1450} \gtrsim 10^{46}$erg s^{-1}) compared to the other samples. However, its FWHM(C IV) and $\Delta V_{\rm line}$ (C IV) distributions very closely follow the SDSS DR7Q distributions.

B.3 Principal Component analysis

In Table B.2 we show the correlation matrix associated to the most relevant C IV and Mg II measurements in both SDSS samples. We ran a Principal Component Analysis (PCA) on this correlation matrix to find different groups of interconnected variables and obtain the amount of variance driven by each group. In Table B.3 we show the correlation coefficients between the first three eigenvectors and the quantities that define them. We can observe that the first Eigenvector (EV1) is responsible for 38 and 32 percent of the variance in the DR7Q and DR12Q samples respectively. In both cases, FWHM(C IV) and $L_{\rm peak}$ [C IV/1450Å] show the strongest correlations with EV1 indicating that the FWHM(C IV)-$L_{\rm peak}$ [C IV/1450Å] anti-correlation drives EV1 and con-

Table B.3: *Pearson correlation coefficients between the listed quantities and the three first Eigenvectors (EV1, EV2 and EV3) obtained from principal component analysis for the DR7Q and DR12Q correlation matrices shown in Table B.2*

	DR7			DR12		
	EV1	EV2	EV3	EV1	EV2	EV3
Cumulative Variance	38%	54%	67%	32%	47%	61%
FWHM(C IV)	-0.81	0.27	-0.23	-0.75	0.21	0.25
FWHM(Mg II)	0.07	0.86	0.33	0.1	0.87	-0.3
FWHM [C IV/Mg II]	-0.72	-0.39	-0.43	-0.68	-0.45	0.41
L_{1450}	-0.48	0.25	-0.17	-0.62	0.22	-0.01
$\Delta V_{\rm peak}$ (C IV)	0.73	0.09	0.09	0.64	-0.04	0.01
$\Delta V_{\rm line}$ (C IV)	-0.74	-0.15	-0.15	-0.71	-0.01	0.04
$L_{\rm peak}$ [C IV/1450Å]	0.86	-0.04	-0.37	0.79	0.02	0.33
$L_{\rm peak}$ [C IV/SiOIV]	0.77	0.05	-0.18	0.77	0	0.13
$L_{\rm peak}$ [C IV/C III]]	-0.6	-0.25	0.45	-0.61	-0.04	-0.3
EW(C IV)	0.47	0.27	-0.74	0.27	0.38	0.84
$L_{\rm peak}$ (C IV) /L (C IV)	0.74	-0.4	0.37	0.45	-0.43	-0.66
^{12}FWHM (Mg II) /σ (Mg II)	-0.13	0.76	0.31	-0.05	0.76	-0.3
L_{3000}/L_{1450}	0.14	-0.41	0.4	-0.13	-0.03	-0.19

sequently a large percentage of the variance in the SDSS samples. FWHM [C IV/Mg II], L_{1450}, $L_{\rm peak}$ [C IV/SiOIV], $L_{\rm peak}$ [C IV/C III]], $\Delta V_{\rm peak}$ (C IV), $\Delta V_{\rm line}$ (C IV) and EW(C IV) and $L_{\rm peak}$ (C IV) /L (C IV) also show important correlations with EV1. However, these correlations are basically caused by the strong dependence of these quantities with FWHM(C IV) and $L_{\rm peak}$ [C IV/1450Å].

The second Eigenvector (EV2) is responsible for 16% and 15% of the variance in the DR7Q and DR12Q samples, respectively, and is strongly correlated with FWHM(Mg II) in both samples. It also shows a strong correlation with FWHM (Mg II) /σ (Mg II) and a strong anti-correlation with FWHM [C IV/Mg II], which is basically inherited from their correlations with FWHM(Mg II). Given that by definition EV2 is linearly independent of the other Eigenvectors, this result reveals that FWHM(Mg II) is basically independent of any C IV related quantity and may indicate that C IV and Mg II profiles show completely independent behaviours.

Finally, the third Eigenvector (EV3) drives 13% and 14% of the variance of the SDSS samples, respectively, and is strongly correlated with EW(C IV) as well as with $L_{\rm peak}$ (C IV) /L (C IV) which are both strongly correlated with each other because of their dependence on L (C IV). It also exhibits a correlation with FWHM [C IV/Mg II] which is not correlated with any of these quantities. Thus, EV3 does not provide a link between C IV and Mg II properties.

Appendix C

Accretion disc models

The material presented in this appendix is based on the work published in Capellupo et al. (2015) and Capellupo et al. (2016) which I coauthored.

C.1 Thin accretion disc model

In this work, we use the numerical code described in Slone & Netzer (2012) to calculate synthetic thin AD spectra. This code assumes the blackbody thin-disc model of Shakura & Sunyaev (1973) disc with major improvements in two areas: the inclusion of general relativity terms and the improvement of the radiative transfer in the disc atmosphere. In this case, $M_{\rm BH}$, $\dot{M}$, a_* and the viscosity parameter (α) determine the intrinsic SED of the accretion disc. Our calculations include Comptonization of the emitted radiation in the AD atmosphere (Hubeny et al., 2001; Davis & Laor, 2011) and, for BH spin values of $a_* \geq 0$, full general relativistic corrections. For retrograde discs with $a_* < 0$, the general relativistic effects are not included, which is a fair approximation because of the large size of the ISCO ($> 6r_g$, where r_g is the gravitational radius of the black hole). Throughout this work we assume $\alpha = 0.1$

C.2 Black hole mass and accretion rate determination

In our SED modelling the two input parameters are $M_{\rm BH}$ and $\dot{M}$. For each AGN in our sample, we calculate both M_{BH} and $\dot{M}$ directly from the observed spectrum.

For M_{BH}, we use the single epoch estimations from the Hα emission line using the new calibration derived in chapter 2. To measure $\dot{M}$, we follow several earlier works

based on the properties of thin ADs, e.g., Collin et al. (2002); Davis & Laor (2011). The SED of such systems, at long enough wavelengths, is given by a canonical power-law of the form $L_\nu \propto \nu^{1/3}$. Given a known $M_{\rm BH}$, the mass accretion rate can be directly determined by using the monochromatic luminosity in the region of the continuum showing such a power-law. The only additional unknown is the disc inclination to the line of sight. The expression we use here is taken from Netzer et al. (2014) and is given by:

$$4\pi D_L^2 F_\nu = f(\theta)[M_8 \dot{M}_\odot]^{2/3} \left[\frac{\lambda}{5100\ \text{Å}}\right]^{-1/3} \text{erg cm}^{-2}\,\text{s}^{-1}\,\text{Hz}^{-1}\ , \qquad \text{(C.C.1)}$$

where F_ν is the observed monochromatic flux, M_8 is the BH mass in units of $10^8\,M_\odot$, $\dot{M}_\odot$ the accretion rate in units of $M_\odot$/yr, and D_L the luminosity distance. The inclination dependent term, $f(\theta)$, gives the angular dependence of the emitted radiation. There are various possibilities for parametrizing this term (see Netzer et al., 2014). Here we express it as:

$$f(\theta) = \frac{f_0 F_\nu}{F_\nu(\text{face-on})} = f_0 \frac{\cos\theta(1 + b(\nu)\cos\theta)}{1 + b(\nu)}\ , \qquad \text{(C.C.2)}$$

where θ is the inclination to the line of sight and $b(\nu)$ is a limb darkening function which, in the present work, we assume to be frequency independent with $b(\nu) = 2$. For this case, $f_0 \simeq 1.2 \times 10^{30}$ erg/sec/Hz. This constant was obtained from realistic thin accretion models calculated by Slone and Netzer (2012), at a rest-frame wavelength of 5100 Å. Because of this, it is slightly different from other values quoted in the literature (e.g. Davis & Laor 2011, as corrected in Laor & Davis 2011).

Throughout this work, we use $\dot{m}$ to describe the normalized (or Eddington) mass accretion rate,

$$\dot{m} = \frac{\dot{M}}{\dot{M}_{Edd}}\,, \qquad \text{(C.C.3)}$$

where $\dot{M} = L_{\rm bol}/\eta c^2$ and $\dot{M}_{\rm Edd} = L_{\rm Edd}/\eta c^2$. We assume $L_{\rm Edd} = 1.5 \times 10^{46}\,M_8\,\text{erg}\,\text{s}^{-1}$, which applies to solar composition gas. Using this definition, $\dot{m}$=$L/L_{\rm Edd}$.

The above expressions can be re-arranged to estimate $\dot{M}$ by using the intrinsic λL_λ at a chosen wavelength. Longer wavelengths are likely to provide better estimates since the approximation is based on the $L_\nu \propto \nu^{1/3}$ part of the disc SED. For $M_{\rm BH} > 10^8 M_\odot$ and relatively small $\dot{M}$, this section of the SED corresponds to wavelengths longer than about 6000Å (e.g. figure 1 in Netzer et al., 2014). We choose the wavelength of λ =8600Å, which is well beyond 6000 Å, is located within the K-band of the observed SEDs, and is clear of emission lines.

A disadvantage associated with this choice is that towards longer wavelengths, the stellar light in the host galaxy starts to contribute significantly to the measured continuum. This effect is much more significant for fainter AGN than those studied here

Table C.1: *Parameter values for the grid of AD models.*

Parameter	Δ	Min-Max values
$\log M_{BH}$ $[M_\odot]$	0.075	7.40 : 10.25
$\log \dot{M}$ $[M_\odot/\mathrm{yr}]$	0.075	-1.50 : $+2.10$
a_*	0.1	-1.0 : $+0.998$
f_{sca}	0.067	1.000 : 0.330
A_V (mag)	0.05	0.00 : 0.50

(Stern & Laor, 2012). We determine which objects require a host galaxy subtraction based on the rest-wavelength equivalent width (EW) of the Hα emission line. The EW of the Balmer lines is not affected by the Baldwin effect, and the Hα line intensity is a reliable bolometric luminosity indicator (Stern & Laor, 2012). We first look at the EW distribution of the brightest 28 AGN in the sample, whose luminosity at 5100Å is high enough that host contamination is small enough to safely be neglected (Shen et al., 2011). We then compare the EW distribution for the 11 faintest AGN in the sample to the distribution for the brighter AGN, and we find most of the faint AGN have EW smaller than the median EW of the brighter AGN (i.e. EW $<$ 400Å). This clustering of AGN at low EW, as compared to the distribution of EW for the brighter sample, indicates there is host galaxy contamination to the continuum luminosity in this wavelength region for these few objects.

In order to subtract the host galaxy for these few faint objects, we use a Bruzual & Charlot (2003) model of an old stellar population, with an age of 11 Gyr and solar metallicity. Such stellar population models have been used in many earlier works to correct for host galaxy contamination (e.g. Bongiorno et al., 2014; Banerji et al., 2015). We scale the stellar population model based on the ratio between the observed Hα EW and the median of the EW distribution (400Å). Younger stellar populations have a larger contribution in the UV, but using a stellar population with an age of 900 Myr, instead of the 11 Gyr model, changes the luminosity by less than 5% at 3000 Å in the corrected AGN spectrum. Therefore, the choice of stellar population model does not have a large effect on the UV spectrum of our AGN. We now use these corrected spectra for measuring $\dot{M}$ and for the remainder of the analysis presented in this thesis.

C.3 Bayesian SED-Fitting Procedure

We generate a grid of thin AD models using the Slone & Netzer (2012) code, and we use a Bayesian method to fit the models to the observed spectra. Our grid consist of 441,440 models for evenly spaced values of M_{BH}, $\dot{M}$, a_* and the scaling factor ($f_{\mathrm{sca}} = \cos\theta(1 + 2\cos\theta)/3$) as described in Table C.1. To account for the possible host-galaxy intrinsic reddening we include A_V as a parameter in the Bayesian analysis. We adopt a range in A_V from 0. to 0.50 mag, in intervals of 0.05. To deredden the X-shooter spectra we adopt a simple power-law curve, where $A(\lambda) = A_V\,(\lambda/\lambda_V)^{-1}$ mag.

.

In our Bayesian approach, we determine the posterior probability for each of the 441,440 models for each value of A_V for each source. This probability is the product of the likelihood, $\mathcal{L}(m)$, and priors on $M_{\rm BH}$ and $\dot{M}$. We have no prior knowledge on a_*, cos θ[1], or the amount of intrinsic reddening. The likelihood is based on the standard χ^2 statistic, measured using up to seven line-free continuum windows, centred at 1353, 1464, 2200, 4205, 5100, 6205, and 8600 Å. The widths of these bands range from 10 to 50 Å. For five objects at the upper end of the narrow redshift range of our sample, the bands centred on 4205 and 5100 Å fall within regions of strong atmospheric absorption and are thus unusable. When calculating the χ^2, we combine the standard error from Poisson noise and an assumed 5 per cent error on the flux calibration.

We use Gaussian priors on the observed values (M_{BH}^{obs}, $\dot{M}^{obs}$) and with standard deviations (σ_M, $\sigma_{\dot{M}}$) given by their uncertainties. We adopt 0.3 and 0.2 dex for σ_M and $\sigma_{\dot{M}}$, respectively. The resulting posterior probability is given by:

$$\begin{aligned}\text{posterior} \propto \exp(-\chi^2/2) \times \exp(-(M_{BH}^{obs} - M_{BH}^{mod})^2/2\sigma_M^2) \\ \times \exp(-(\dot{M}^{obs} \times \frac{M_{BH}^{obs}}{M_{BH}^{mod}} - \dot{M}^{mod})^2/2\sigma_{\dot{M}}^2).\end{aligned}$$

The Bayesian procedure ranks the 441,440 models based on the posterior probability for each one. We consider an AGN to have a satisfactory thin AD fit when the model with the highest probability has a reduced χ^2 statistic less than 3.

[1]We only consider cos $\theta > 0.5$, appropriate for type-I AGN.

Bibliography

Abazajian, K. N., et al. 2009, ApJS, 182, 543

Antonucci, R. 1993, ARA&A, 31, 473

Antonucci, R. R. J., & Miller, J. S. 1985, ApJ, 297, 621

Arav, N., Borguet, B., Chamberlain, C., Edmonds, D., & Danforth, C. 2013, MNRAS, 436, 3286

Banerji, M., et al. 2015, MNRAS, 454, 419

Baron, D., Stern, J., Poznanski, D., & Netzer, H. 2016, ArXiv e-prints

Baskin, A., & Laor, A. 2004, MNRAS, 350, L31

—. 2005, MNRAS, 356, 1029

Batiste, M., Bentz, M. C., Raimundo, S. I., Vestergaard, M., & Onken, C. A. 2017, ApJ, 838, L10

Bentz, M. C., & Katz, S. 2015, PASP, 127, 67

Bentz, M. C., Peterson, B. M., Netzer, H., Pogge, R. W., & Vestergaard, M. 2009, ApJ, 697, 160

Bentz, M. C., et al. 2013, ApJ, 767, 149

Bongiorno, A., et al. 2014, MNRAS, 443, 2077

Borguet, B. C. J., Arav, N., Edmonds, D., Chamberlain, C., & Benn, C. 2013, ApJ, 762, 49

Boroson, T. A., & Green, R. F. 1992, ApJS, 80, 109

Brotherton, M. S., Runnoe, J. C., Shang, Z., & DiPompeo, M. A. 2015a, ArXiv e-prints

Brotherton, M. S., Singh, V., & Runnoe, J. 2015b, MNRAS, 454, 3864

Bruzual, G., & Charlot, S. 2003, MNRAS, 344, 1000

Capellupo, D. M., Netzer, H., Lira, P., Trakhtenbrot, B., & Mejía-Restrepo, J. 2015, MNRAS, 446, 3427

—. 2016, MNRAS, 460, 212

Coatman, L., Hewett, P. C., Banerji, M., & Richards, G. T. 2016, MNRAS, 461, 647

Coatman, L., Hewett, P. C., Banerji, M., Richards, G. T., Hennawi, J. F., & Prochaska, J. X. 2017, MNRAS, 465, 2120

Collin, S., Boisson, C., Mouchet, M., Dumont, A.-M., Coupé, S., Porquet, D., & Rokaki, E. 2002, A&A, 388, 771

Collin, S., Kawaguchi, T., Peterson, B. M., & Vestergaard, M. 2006, A&A, 456, 75

Corbin, M. R. 1990, ApJ, 357, 346

Corbin, M. R., & Boroson, T. A. 1996, ApJS, 107, 69

Croom, S. M., Smith, R. J., Boyle, B. J., Shanks, T., Miller, L., Outram, P. J., & Loaring, N. S. 2004, MNRAS, 349, 1397

Czerny, B., Du, P., Wang, J.-M., & Karas, V. 2016, ApJ, 832, 15

Davis, S. W., & Laor, A. 2011, ApJ, 728, 98

De Rosa, G., et al. 2014, ApJ, 790, 145

Decarli, R., Dotti, M., Fontana, M., & Haardt, F. 2008a, MNRAS, 386, L15

Decarli, R., Labita, M., Treves, A., & Falomo, R. 2008b, MNRAS, 387, 1237

Del Moro, A., et al. 2016, MNRAS, 456, 2105

Denney, K. D. 2012, ApJ, 759, 44

Denney, K. D., Peterson, B. M., Dietrich, M., Vestergaard, M., & Bentz, M. C. 2009a, ApJ, 692, 246

Denney, K. D., Pogge, R. W., Assef, R. J., Kochanek, C. S., Peterson, B. M., & Vestergaard, M. 2013, ApJ, 775, 60

Denney, K. D., et al. 2009b, ApJ, 704, L80

—. 2010, ApJ, 721, 715

Done, C., & Krolik, J. H. 1996, ApJ, 463, 144

Du, P., et al. 2015, ApJ, 806, 22

Dunn, O. J., & Clark, V. 1969, Journal of the American Statistical Association, 64, 366

Ferrarese, L., & Merritt, D. 2000, ApJ, 539, L9

Fine, S., Croom, S. M., Bland-Hawthorn, J., Pimbblet, K. A., Ross, N. P., Schneider, D. P., & Shanks, T. 2010, MNRAS, 409, 591

Fine, S., et al. 2006, MNRAS, 373, 613

—. 2008, MNRAS, 390, 1413

Foreman-Mackey, D., Hogg, D. W., Lang, D., & Goodman, J. 2013, PASP, 125, 306

Ganguly, R., Brotherton, M. S., Cales, S., Scoggins, B., Shang, Z., & Vestergaard, M. 2007, ApJ, 665, 990

Gaskell, C. M. 1982, ApJ, 263, 79

—. 2009, New Astronomy Review, 53, 140

Gaskell, C. M., & Goosmann, R. W. 2013, ApJ, 769, 30

Ge, X., Bian, W.-H., Jiang, X.-L., Liu, W.-S., & Wang, X.-F. 2016, MNRAS, 462, 966

Ginsburg, A., & Mirocha, J. 2011, PySpecKit: Python Spectroscopic Toolkit, Astrophysics Source Code Library

Glen, A. G., Leemis, L. M., & Drew, J. H. 2004, Computational Statistics & Data Analysis, 44, 451

Goosmann, R. W., & Gaskell, C. M. 2007, A&A, 465, 129

Graham, A. W. 2015, ArXiv e-prints

Graham, A. W., Onken, C. A., Athanassoula, E., & Combes, F. 2011, MNRAS, 412, 2211

Grandi, S. A. 1982, ApJ, 255, 25

Greene, J. E., & Ho, L. C. 2005, ApJ, 630, 122

Gültekin, K., et al. 2009, ApJ, 698, 198

Häring, N., & Rix, H.-W. 2004, ApJ, 604, L89

Hewett, P. C., & Wild, V. 2010, MNRAS, 405, 2302

Ho, L. C., Goldoni, P., Dong, X.-B., Greene, J. E., & Ponti, G. 2012, ApJ, 754, 11

Hubeny, I., Blaes, O., Krolik, J. H., & Agol, E. 2001, ApJ, 559, 680

Kallman, T. R., & Krolik, J. H. 1986, ApJ, 308, 805

Kaspi, S., Brandt, W. N., Maoz, D., Netzer, H., Schneider, D. P., & Shemmer, O. 2007, ApJ, 659, 997

Kaspi, S., Maoz, D., Netzer, H., Peterson, B. M., Vestergaard, M., & Jannuzi, B. T. 2005, ApJ, 629, 61

Kaspi, S., Smith, P. S., Netzer, H., Maoz, D., Jannuzi, B. T., & Giveon, U. 2000, ApJ, 533, 631

Khachikian, E. Y., & Weedman, D. W. 1974, ApJ, 192, 581

Kollatschny, W., & Zetzl, M. 2011, Nature, 470, 366

—. 2013, A&A, 558, A26

Kormendy, J., & Ho, L. C. 2013, ARA&A, 51, 511

Labita, M., Decarli, R., Treves, A., & Falomo, R. 2009, MNRAS, 399, 2099

Laor, A., Barth, A. J., Ho, L. C., & Filippenko, A. V. 2006, ApJ, 636, 83

Laor, A., & Davis, S. W. 2011, MNRAS, 417, 681

Laor, A., Jannuzi, B. T., Green, R. F., & Boroson, T. A. 1997, ApJ, 489, 656

Lopez, S., & Jenkins, J. S. 2012, ApJ, 756, 177

Marconi, A., Axon, D. J., Maiolino, R., Nagao, T., Pastorini, G., Pietrini, P., Robinson, A., & Torricelli, G. 2008, ApJ, 678, 693

Marziani, P., Dultzin-Hacyan, D., & Sulentic, J. W. 2006, Accretion onto Supermassive Black Holes in Quasars: Learning from Optical/UV Observations (Nova Science Publishers), 123

Marziani, P., Sulentic, J. W., Plauchu-Frayn, I., & del Olmo, A. 2013a, A&A, 555, A89

—. 2013b, ApJ, 764, 150

McConnell, N. J., & Ma, C.-P. 2013, ApJ, 764, 184

McLure, R. J., & Dunlop, J. S. 2001, MNRAS, 327, 199

—. 2002, MNRAS, 331, 795

—. 2004, MNRAS, 352, 1390

McLure, R. J., & Jarvis, M. J. 2002, MNRAS, 337, 109

Mejía-Restrepo, J. E., Trakhtenbrot, B., Lira, P., Netzer, H., & Capellupo, D. M. 2016, MNRAS, 460, 187

Mortlock, D. J., et al. 2011, Nature, 474, 616

Müller, A., & Wold, M. 2006, A&A, 457, 485

Netzer, H. 1977, MNRAS, 181, 89P

—. 2006, ApJ, 652, L117

Netzer, H., Lira, P., Trakhtenbrot, B., Shemmer, O., & Cury, I. 2007, ApJ, 671, 1256

Netzer, H., & Marziani, P. 2010, ApJ, 724, 318

Netzer, H., Mor, R., Trakhtenbrot, B., Shemmer, O., & Lira, P. 2014, ApJ, 791, 34

Netzer, H., & Trakhtenbrot, B. 2014, MNRAS, 438, 672

Ng, P., & Maechler, M. 2007, Statistical Modelling, 7, 315

Onken, C. A., Ferrarese, L., Merritt, D., Peterson, B. M., Pogge, R. W., Vestergaard, M., & Wandel, A. 2004, ApJ, 615, 645

Onken, C. A., & Peterson, B. M. 2002, ApJ, 572, 746

Pancoast, A., Brewer, B. J., Treu, T., Park, D., Barth, A. J., Bentz, M. C., & Woo, J.-H. 2014, MNRAS, 445, 3073

Pâris, I., et al. 2012, A&A, 548, A66

—. 2016, ArXiv e-prints

Park, D., Woo, J.-H., Denney, K. D., & Shin, J. 2013, ApJ, 770, 87

Park, D., et al. 2012, ApJ, 747, 30

Peterson, B. M., & Wandel, A. 1999, ApJ, 521, L95

—. 2000, ApJ, 540, L13

Peterson, B. M., et al. 2004, ApJ, 613, 682

Popovic, L. C., Vince, I., Atanackovic-Vukmanovic, O., & Kubicela, A. 1995, A&A, 293, 309

Rafiee, A., & Hall, P. B. 2011, ApJS, 194, 42

Ricci, C., et al. 2017, MNRAS, 468, 1273

Richards, G. T., Vanden Berk, D. E., Reichard, T. A., Hall, P. B., Schneider, D. P., SubbaRao, M., Thakar, A. R., & York, D. G. 2002, AJ, 124, 1

Richards, G. T., et al. 2011, AJ, 141, 167

Runnoe, J. C., Brotherton, M. S., DiPompeo, M. A., & Shang, Z. 2014, MNRAS, 438, 3263

Runnoe, J. C., Brotherton, M. S., Shang, Z., & DiPompeo, M. A. 2013, MNRAS, 434, 848

Satyapal, S., Ellison, S. L., McAlpine, W., Hickox, R. C., Patton, D. R., & Mendel, J. T. 2014, MNRAS, 441, 1297

Schneider, D. P., et al. 2010, AJ, 139, 2360

Sergeev, S. G., Pronik, V. I., Sergeeva, E. A., & Malkov, Y. F. 1999, ApJS, 121, 159

Shakura, N. I., & Sunyaev, R. A. 1973, A&A, 24, 337

Shang, Z., Wills, B. J., Wills, D., & Brotherton, M. S. 2007, AJ, 134, 294

Shen, Y. 2013, Bulletin of the Astronomical Society of India, 41, 61

Shen, Y., Greene, J. E., Strauss, M. A., Richards, G. T., & Schneider, D. P. 2008, ApJ, 680, 169

Shen, Y., & Ho, L. C. 2014, Nature, 513, 210

Shen, Y., & Liu, X. 2012, ApJ, 753, 125

Shen, Y., et al. 2011, ApJS, 194, 45

Slone, O., & Netzer, H. 2012, MNRAS, 426, 656

Stalevski, M., Ricci, C., Ueda, Y., Lira, P., Fritz, J., & Baes, M. 2016, MNRAS, 458, 2288

Stern, J., & Laor, A. 2012, MNRAS, 423, 600

Sulentic, J. W., Bachev, R., Marziani, P., Negrete, C. A., & Dultzin, D. 2007, ApJ, 666, 757

Sulentic, J. W., Marziani, P., Zamanov, R., Bachev, R., Calvani, M., & Dultzin-Hacyan, D. 2002, ApJ, 566, L71

Tilton, E. M., & Shull, J. M. 2013, ApJ, 774, 67

Trakhtenbrot, B., & Netzer, H. 2012, MNRAS, 427, 3081

Trakhtenbrot, B., Netzer, H., Lira, P., & Shemmer, O. 2011, ApJ, 730, 7

Tremaine, S., Shen, Y., Liu, X., & Loeb, A. 2014, ApJ, 794, 49

Tsuzuki, Y., Kawara, K., Yoshii, Y., Oyabu, S., Tanabé, T., & Matsuoka, Y. 2006, ApJ, 650, 57

Ulrich, M.-H., & Horne, K. 1996, MNRAS, 283, 748

Urry, C. M., & Padovani, P. 1995, PASP, 107, 803

Vanden Berk, D. E., et al. 2004, ApJ, 601, 692

Vestergaard, M. 2002, ApJ, 571, 733

Vestergaard, M., & Osmer, P. S. 2009, ApJ, 699, 800

Vestergaard, M., & Peterson, B. M. 2006, ApJ, 641, 689

Wall, J. V., Jackson, C. A., Shaver, P. A., Hook, I. M., & Kellermann, K. I. 2005, A&A, 434, 133

Wang, J.-G., et al. 2009, ApJ, 707, 1334

Wills, B. J., & Browne, I. W. A. 1986, ApJ, 302, 56

Wills, B. J., Netzer, H., Brotherton, M. S., Han, M., Wills, D., Baldwin, J. A., Ferland, G. J., & Browne, I. W. A. 1993, ApJ, 410, 534

Woo, J.-H., Yoon, Y., Park, S., Park, D., & Kim, S. C. 2015, ApJ, 801, 38

Woo, J.-H., et al. 2010, ApJ, 716, 269

Wu, X.-B., et al. 2015, Nature, 518, 512

Xiao, T., Barth, A. J., Greene, J. E., Ho, L. C., Bentz, M. C., Ludwig, R. R., & Jiang, Y. 2011, ApJ, 739, 28

York, D. G., et al. 2000, AJ, 120, 1579

Zheng, W., & Sulentic, J. W. 1990, ApJ, 350, 512

Zuo, W., Wu, X.-B., Fan, X., Green, R., Wang, R., & Bian, F. 2015, ApJ, 802, 140